PHYSIK-DEPARTMENT

Self-consistent Projection Operator Theory

Dissertation

von

Peter Degenfeld-Schonburg

TECHNISCHE UNIVERSITÄT
MÜNCHEN

TECHNISCHE UNIVERSITÄT MÜNCHEN

Physik Department

Arbeitsgruppe „Quantum Optics and Quantum Dynamics“,
Lehrstuhl T34, Prof. Dr. Michael J. Hartmann

Self-consistent Projection Operator Theory

Peter Degenfeld-Schonburg

Vollständiger Abdruck der von der Fakultät für Physik der Technischen Universität München zur Erlangung des akademischen Grades eines

Doktors der Naturwissenschaften (Dr. rer. nat.)

genehmigten Dissertation.

Vorsitzender:	Prof. Dr. Rudolf Gross
Prüfer der Dissertation:	1. Prof. Dr. Michael J. Hartmann
	2. Prof. Dr. Michael Knap
	3. Prof. Dr. Michael Fleischhauer (schriftliche Beurteilung)

Die Dissertation wurde am 08.06.2016 bei der Technischen Universität München eingereicht und durch die Fakultät für Physik am 25.10.2016 angenommen.

Abstract

In this thesis we develop the self-consistent projection operator theory which provides a highly efficient and accurate approach to the calculation of local properties of a quantum few- or many-body system by defining a time dependent projection operator. This projector, which is coined self-**c**onsistent **Mo**ri **p**rojector (c-MoP), allows for a derivation of an integro-differential equation that generalizes the Nakajima-Zwanzig equation and exactly describes the dynamics of reduced density matrices of all subsystems of a large quantum system. The c-MoP theory generalizes the concepts of open systems theory to settings where a dynamically evolving environment has to be taken into account and provides a systematic extension of mean-field approaches. We illustrate the power of our theory for a broad range of applications by testing its performance for the determination of stationary states and transient time evolutions, both, for the models of nonlinear quantum optics and driven-dissipative many body lattice systems.

In the case of one dimensional spin lattices c-MoP is very efficient and its accuracy for local observables compares with t-DMRG methods, yet, offering a formalism which is directly applicable to any lattice dimension. For the degenerate optical parametric oscillator, c-MoP gives quasi exact solutions for the reduced quantum states of the nonlinearly coupled bosonic modes even at the critical point of the dissipative phase transition. We further develop a Gaussian approach consistent with our theory, which yields sensibly better results than any previously developed Gaussian methods and even reaches accuracies comparable to diagrammatic Keldysh approaches. Finally, we exploit the c-MoP theory to enable the investigation of the optomechanical interaction between a mechanical mode and a light field of purely quantum nature in the degenerate optomechanical parametric oscillator setup. Our work, thus, illustrates the potential of c-MoP theory for the analysis of hybrid dissipative quantum systems in the vicinity of critical points.

Within the framework of this thesis, the following articles were published in refereed journals, listed in chronological order:

- P. Degenfeld-Schonburg, E. del Valle, and M. J. Hartmann, *Signatures of single-site addressability in resonance fluorescence spectra*, Phys. Rev. A **85**, 013842 (2012)
- P. Degenfeld-Schonburg and M. J. Hartmann, *Self-consistent projection operator theory for quantum many-body systems*, Phys. Rev. B **89**, 245108 (2014).
- S. Okubo, M. Eto, P. Degenfeld-Schonburg, and M. J. Hartmann *Study of coupled QED-cavities using the self-consistent Mori projector method*, Journal of Physics, Conf. Ser. **568**, 012014 (2014).
- P. Degenfeld-Schonburg, C. Navarrete-Benlloch and M. J. Hartmann, *Self-consistent projection operator theory in nonlinear quantum optical systems: A case study on degenerate optical parametric oscillators*, Phys. Rev. A **91**, 053850 (2015).
- P. Degenfeld-Schonburg, M. Abdi, M. J. Hartmann, and C. Navarrete-Benlloch, *Degenerate optomechanical parametric oscillators: cooling in the vicinity of a critical point*, Phys. Rev. A **93**, 023819 (2016).
- S. Pina-Otey, F. Jiménez, P. Degenfeld-Schonburg, and C. Navarrete-Benlloch, *Classical and quantum linearized descriptions of degenerate optomechanical parametric oscillators*, Phys. Rev. A **93**, 033835 (2016).
- M. Abdi, P. Degenfeld-Schonburg, M. Sameti, C. Navarrete-Benlloch and M. J. Hartmann, *Dissipative optomechanical preparation of macroscopic quantum superposition states*, Phys. Rev. Lett. **116**, 233604 (2016).

Contents

Introduction

Since the beginning of the 20th century researchers have faced tremendous challenges with physical systems that inevitably need to be described by the laws of quantum mechanics. The axiomatic Schrödinger equation, constituting the analog of Newtons 2nd law for classical systems, defies an analytic solution in almost all cases of interest. Already for one-particle problems only a few exact analytic solutions are known, with the hydrogen atom and the quantum harmonic oscillator as the most prominent examples [1]. Even more demanding seems the handling of quantum mechanical models in which more than one particle needs to be accounted for. Clearly, finding the solution to Schrödinger's equation paves the way to the understanding of the physics represented by the models. The search for methods which at least approximately solve the many-body quantum problem thus places a cornerstone in a diversity of research fields including statistical mechanics [2, 3], open systems theory [4, 5], quantum optics [6, 7] and condensed matter theory [8, 9].

In all of these fields it is possible to encounter different categories of approaches to the complex quantum problem. In one category we find sophisticated analytical methods that lead to exact solutions for models exhibiting certain features such as symmetries, low spatial dimensions, or arbitrarily large time-scale separation. To name just a few there are spin chain models solved by the Bethe Ansatz [10], P-function methods [11, 12] for nonlinear quantum optical systems or the solution of Weisskopf and Wigner [13] for a certain version of the Spin-Boson problem [14]. These exactly solvable examples contribute a significant but still small subpart of quantum models.

The technological developments in the area of computer and numerical sciences over the last few decades enabled a second category, that is the exploitation of powerful numerical techniques in order to solve complex problems. For systems obeying the laws of classical physics nowadays computers and commercial software enable the efficient simulation of large-scale systems which is relevant for science and also for industrial applications [15]. In the case of quantum mechanics, however, the complexity of the system does not scale linearly, as in the classical case, but rather exponentially with the number of constituents. This scaling behavior is a fundamental consequence of the mathematical structure of quantum mechanics [1] and can not be overcome. Thus, numerical methods indeed enlarge the set of solvable quantum mechanical models [16] but they are still restricted to rather small system sizes or need to invoke approximations. The general quantum many-body problem still remains as one of the great challenges of modern physics.

Finally, in the third category we find a large diversity of effective or rather approximative theories. The main goal of these theories is to introduce reasonably accurate descriptions of the physical model under study which obey effective equations of motion that can be solved much more efficiently than the full quantum mechanical model. One particularly important idea is to introduce descriptions which do not explore the entire Hilbert space but only account for a subpart of the full quantum system. A prominent representative of this strategy in the context of condensed matter theory are mean-field approaches [17] as they only predict local properties of the many-body system [18]. In the same spirit semi-classical treatments often used in quantum optics [19, 20] solely explore the subclass of states which are described by gaussian quantum fluctuations centered around the classical coherent state.

In systems where the dynamical degrees of freedom evolve on different time scales, approximate but yet highly accurate descriptions of reduced complexity may be found. The concept of time-scale separation forms the underlying assumption of adiabatic elimination methods or more generally open systems theories [4, 5]. The "slow" and the "fast" subparts of the whole system are split into "system" and "environment", respectively. The former contains the information of interest about the quantum state while the information of the latter can be disregarded leading to an equation of reduced complexity for the system variables only. This exact equation for the reduced quantum state of the system is known as the Nakajima-Zwanzig equation [4] and it can be formally deduced from the Schrödinger or rather Liouville-von Neumann equation by exploiting the Mori projection operator technique [21].

For many microscopic models within the validity of the so called Born-Markov approximation, which is indeed a direct consequence of time-scale separation between the system and its environment, the Nakajima-Zwanzig equation reduces to the widely celebrated Lindblad master equation [22, 23]. The Lindblad terms of a master equation describe fundamental physical effects such as decoherence and dissipation due to the "openness" of the system. Consequently, the theory of open systems has found its applications in almost all fields of science with the field of quantum optics being a paradigmatic example. Moreover, the idea of introducing dissipation to the traditional closed system examples of condensed matter theory is currently receiving enormous interest in the search for strongly correlated steady states and non-equilibrium analogs of quantum phase transitions [24–26].

The Born-Markov approximation usually goes hand in hand with the underlying time-scale separation assumption of open systems theory with the latter putting bounds to its applicability. Therefore, a large body of works have also been devoted to the treatment of open systems beyond the Markovian limit [27]. While in numerical works on this topic the separation into system and environment is abandoned and instead the full problem is solved by a very careful selection of the relevant states [28], in the framework of projection operator techniques time-convolutionless [4] and correlated projection operator methods [29] were invented.

The question of how to introduce back-action effects of the system onto the environment into a projection operator formalism, enabling the treatment of scenarios where there is no clear distinction between fast and slow degrees of freedom, remained unresolved until today.

The purpose of this thesis is to introduce the self-consistent Mori projection operator theory (c-MoP) and prove its applicability to the general quantum many-body problem including also the (few-)body scenarios encountered for example in quantum optics.

Conceptually, we introduce a novel approach to the calculation of local properties of a quantum many-body system by defining a time dependent projection operator that may be viewed as a generalization of the Mori projector [21]. Based on this projector, which we coin self-consistent Mori projector, we are able to derive an integro-differential equation that generalizes the Nakajima-Zwanzig equation [3, 4] and exactly describes the dynamics of the reduced density matrix of each of the subsystems of the full many-body setup. By taking dynamical back-action between the degrees of freedom into account, our method does not rely on a pronounced time-scale separation between the subparts thus reaching beyond the applicability of standard open systems theory.

In this thesis we apply the c-MoP theory to a diversity of models including open and closed spin lattices in one and two dimensions and nonlinear quantum optical systems such as the degenerate opto(-mechanical) parametric oscillator and the nonequilibrium Dicke model. The physics of the driven and dissipative phase transitions in all the scenarios investigated here are very accurately described by the c-MoP theory even at the critical points. Throughout the applications we test the accuracy of c-MoP by comparing it to (quasi) exact results, if these are available, and also to other approximative methods such as linearized descriptions, mean-field theory or the Keldysh formalism within the self-consistent Hartree-Fock approximation. In the considered cases we find c-MoP to outperform all of these approximative methods and for 1D spin lattices to compare with the performance of t-DMRG calculations for local observables. In fact, for unitary evolution in the closed system version of the XX spin chain we show that c-MoP even reaches larger time ranges as t-DMRG. Moreover, we highlight how different choices for the self-consistent Mori projector can lead to significantly different efficiencies and accuracies, with the former being strongly dependent on the ability to resolve nonlinear and non-Markovian c-MoP equations for which we provide different possible approaches to solve them.

We also study two direct applications of the c-MoP theory. First, we investigate the quantum to classical transition, which is a nonequilibrium mean-field phase transition of first order, in the locally driven and dissipative Heisenberg XX spin model. By exploiting c-MoP, however, we find a strong signature for the absence of the phase transition both in one and two dimensions even in the thermodynamic limit of infinite lattice sites. Second, we use c-MoP to introduce a theoretical approach that is capable of describing the below threshold regime of the degenerate optomechanical parametric oscillators, even at the critical point itself. We find that the down-converted field can induce significant mechanical cooling and identify the process responsible of this as a ”cooling by heating” mechanism. Moreover, we show that, contrary to naive expectations and semi-classical predictions, cooling is not optimal at the critical point, where the photon number is largest.

The thesis is organized in two Parts. Part I includes Chapter 1 and Chapter 2. In the former we introduce the mathematical foundations, general concepts and ideas of the c-MoP theory while in the latter we show the applicability of c-MoP to quantum many-body lattice problems. Part II contains Chapter 3, Chapter 4 and Chapter 5 where we apply the c-MoP theory to the degenerate optical paramteric oscillator, the degenerate optomechanical parametric oscillator, and the nonequilibrium Dicke model, respectively. In all the chapters we use the c-MoP approach in one variety or another, and yet, the physical context or rather physical models differ a lot throughout all the chapters. Therefore, we provide a more specific introduction for each chapter complementing the general introduction presented here. Moreover, we provide a summary of Part I and a summary of Part II. Finally, we conclude the thesis with an extensive discussion and outlook on future application and optimization of the c-MoP theory.

Part I

The self-consistent projection operator theory and its application to quantum many-body physics

Chapter 1

The self-consistent Mori projector and the c-MoP equations

1.1 Introduction

In this section we will introduce the concept of the self-consistent projection operator theory in its most general form. The time-dependent projection operator takes the central role in the theory and its action on the full state of the quantum model at hand will map out the part of the full quantum state which will be of interest. For this part, we will be able to derive an effective equation of motion which can be viewed as a generalization of the Nakajima-Zwanzig equation [3]. In the same spirit, one can view the time-dependent projection operator as a generalization of the Mori projector [21]. During the course of this chapter we will understand the thoughts behind the nomenclature for the self-consistent Mori projector theory, or in short **c-MoP** theory, and deepen our understanding about the motivation for such an approach by comparing it to its time-independent counterpart, namely open system theory [4], as well as to meanfield theory [17].

The starting point for all applications of this thesis is the physical model under consideration. In every situation the state of the entire quantum system $R(t)$ at every instant of time t is modeled by the Liouville-von Neumann equation of motion

$$\dot{R}(t) = \mathcal{L}R(t), \tag{1.1}$$

where the dot denotes a time derivative. The dynamical evolution of the quantum state shall be generated by the superoperator $\mathcal{L}$. In the case of closed quantum systems the Liouvillian can be directly associated with its corresponding Hamiltonian H and Eq. (1.1) reduces to the Schrödinger equation with $\mathcal{L}R(t) = -i[H, R(t)]$ ($\hbar = 1$ throughout the thesis). However, we will consider Liouvillians $\mathcal{L}$ which may feature non-unitary terms of Lindblad type [22]. We refer to $\mathcal{L}$ as the (full) Liouvillian. In many cases the complexity of the Liouvillian renders an exact solution of Eq. (1.1) impossible. Therefore, it is highly desirable to develop approaches which under certain approximations allow for an effective description of the full Liouville von-Neumann equation. It is precisely such an approach that we will provide in this work. The general concept and the main tools of the theory are introduced in this chapter.

Even though it is desirable to obtain a solution for the entire quantum state $R(t)$, the information contained in the full state is more than enough to understand the desired physical aspects. In fact, in many cases a reduced information of a subpart of the entire system completely suffices. A paradigmatic example is given by the physical situation in which one or an ensemble of atoms couples to the quantized electro-magnetic field [6, 7, 30, 31]. Here, the evolution of the reduced state of the atoms is of interest rather than the evolution of the full set of modes describing the entire mode ensemble of the electro-magnetic field.

Generally, the reduced information of a subpart, let us denote it by n_0, is contained in its reduced density matrix $\rho_{n_0}(t)$. The exact reduced state can be obtained by tracing out all degrees of freedom which do not belong to the subpart n_0 of the full quantum state, thus $\rho_{n_0}(t) = \mathrm{Tr}_{\not{n}_0}\{R(t)\}$, where $\mathrm{Tr}_{\not{n}_0}$ denotes the trace over all parts but the subpart n_0. For any system observable $A_{n_0} \otimes \mathbb{1}_{\not{n}_0}$ it entirely suffices to know the reduced density matrix since

$$\mathrm{Tr}\{A_{n_0} \otimes \mathbb{1}_{\not{n}_0} R(t)\} = \mathrm{Tr}_{n_0}\{A_{n_0} \mathrm{Tr}_{\not{n}_0} R(t)\} = \mathrm{Tr}_{n_0}\{A_{n_0} \rho_{n_0}(t)\}. \tag{1.2}$$

In the light of this insight, the next question naturally arising is whether one can find an effective equation of motion for the evolution of the reduced state. For its usability such an equation should be ”more practical” than the full Liouville von-Neumann equation in the sense that it should provide efficiently solvable equations which will still lead to accurate descriptions of the underlying physical model.

Aiming for this goal, we will exploit the idea of projection operator techniques [4, 5] in order to develop the self-consistent projection operator theory. Our theory is shown to generalize standard projection operator theories or rather open quantum systems theory by taking dynamical back-action between the subparts of the full setup into account and thus not requiring any time-scale separation. In the next section, we highlight the innovations of our work by comparing the major differences of our theory to standard projection operator approaches.

The remainder of Chapter 1 is organized as follows. In Sec. 1.2 we highlight the main innovations of our theory by comparing it to standard open systems theory. The self-consistent Mori projector is introduced in Sec. 1.3. Based on it we derive the generalized Nakajima-Zwanzig equations or the exact c-MoP equations in Sec. 1.4 and use it as the starting point for the Born approximation introduced in Sec. 1.5. We further discuss on the relation of c-MoP to mean-field theories in Sec. 1.5.1, discuss properties of the c-MoP theory such as positivity and nonlinearity in Sec. 1.5.2, introduce the form of the c-MoP equation for unitary interaction Liouvillians in Sec. 1.5.3 which constitutes the main equation of this thesis, and highlight the scaling behavior of our theory in Sec. 1.5.4.

1.2 Generalization of standard open quantum system theory

In the course of this section we employ the notation commonly at use in the context of open quantum systems [4]. In the general scenario of an open quantum system, the full quantum setup described by the state $R(t)$ can be separated into two parts. We refer to the part of interest as the "system" and to the remainder as the "environment". Accordingly, we restate the Liouville von-Neumann equation such that

$$\dot{R}(t) = \mathcal{L}R(t) = (\mathcal{L}_S + \mathcal{L}_E + \mathcal{L}_I)\; R(t), \tag{1.3}$$

with the superoperators $\mathcal{L}_S$ ($\mathcal{L}_E$) describing the free evolution of the system (environment) and $\mathcal{L}_I$ accounting for any system-environment interaction. We are only interested in the reduced information set of the system observables. Thus, we are aiming to derive an effective equation of motion for the reduced state $\rho_S(t)$ which can be obtained by tracing out all environmental degrees of freedom from the full quantum state, i.e. $\rho_S(t) = \mathrm{Tr}_E R(t)$.

For this purpose it proves useful to utilize the idea of projection operator techniques [4, 5] in which the operation of tracing over environmental degrees of freedom can be regarded as a formal projection $R(t) \to PR(t)$. The Mori projector [21] is defined by $P = \rho_E \otimes \mathrm{Tr}_E$ where ρ_E is an arbitrary reference state or rather density matrix with trace one. Usually, see for example Sec. 4.3 within this work, the physically most meaningful reference state is the state which is stationary with respect to its interaction-free generator, i.e.

$$\mathcal{L}_E\, \rho_E = 0\,, \tag{1.4}$$

and additionally coincides with the initial state, that is $\rho_E = \mathrm{Tr}_S R(t_0)$. The Mori projector maps on the relevant part of the density matrix $R(t)$ in the sense that $PR(t) = \rho_E \otimes \rho_S(t) = R_{\mathrm{rel}}(t)$ gives the complete information required to reconstruct the reduced state $\rho_S(t)$. By introducing the complementary operator $Q = \mathbb{1} - P$ one can derive a (formally) exact equation of motion for the relevant part of the density matrix $R_{\mathrm{rel}}(t)$. By tracing over the environment one obtains an exact equation of motion for $\rho_S(t)$ given by

$$\dot{\rho}_S(t) = \mathcal{L}_S \rho_S(t) + \mathrm{Tr}_E \mathcal{L}_I PR(t) + \int_0^t d\tau\, \mathrm{Tr}_E \left\{ \mathcal{L}_I\, e^{(\mathcal{L}_E + \mathcal{L}_S + Q\mathcal{L}_I)\tau} Q \mathcal{L}_I PR(t-\tau) \right\}, \tag{1.5}$$

where we have neglected any initial system-environment correlations. Equation (1.5) is known as the Nakajima-Zwanzig equation (NZE) [3, 4].

We emphasize, the NZE is an exact equation for all choices of environmental reference states ρ_E fulfilling the initial condition $\rho_E = \mathrm{Tr}_S R(t_0)$. However, the NZE is not solvable in its full generality. Due to the interaction Liouvillian entering the exponential $e^{(\mathcal{L}_E+\mathcal{L}_S+Q\mathcal{L}_I)\tau}$ in the integral kernel of the NZE, the complexity of the NZE is comparable to the complexity of the full Liouville von-Neumann equation (1.3) which posseses the formal solution $R(t) = e^{\mathcal{L}t}R(0)$. Therefore, one needs to rely on an expansion in powers of $\mathcal{L}_I$ which can be directly performed on the level of the NZE but not on the level of the full Liouville von-Neumann equation. Within the Born approximation (BA) one expands the NZE up to second order in the interaction by simply dropping the interaction from the exponential in the integral kernel, i.e.

$$e^{(\mathcal{L}_E+\mathcal{L}_S+Q\mathcal{L}_I)\tau} \xrightarrow{\text{BA}} e^{(\mathcal{L}_E+\mathcal{L}_S)\tau}.$$

Whereas the NZE is exact for all choices of ρ_E with $\rho_E = \mathrm{Tr}_S R(t_0)$, the result of the NZE in born approximation (NZE2) strongly depends on the choice of the environmental reference state. In fact, for choices of ρ_E fulfilling Eq. (1.4) the validity or rather accuracy of the BA relies on a time-scale separation where the environmental dynamics must be much faster than the dynamics of the system. In particular, the time-scale separation is present if the time-scale on which the environmental modes react to any perturbation induced by the system is much slower than the relaxation time of the environment with respect to its unperturbed dynamics governed by $\mathcal{L}_E$.

Let us denote the relaxation rate on which the environment relaxes to its stationary state after a perturbation emerging from $\mathcal{L}_I$ by $\gamma_E > 0$. In the framework of the standard projection operator theory it is not clear how to accurately define a rate of perturbation. Therefore, we need to make use of a heuristic argument and simply introduce a rate of perturbation $\alpha > 0$ by redefining $\mathcal{L}_I = \alpha\tilde{\mathcal{L}}_I$. Based on these definitions we expect time-scale separation to be present and consequently the BA to be accurate if $\alpha \ll \gamma_E$.

Moreover, the time-scale separation allows for the applicability of the Markov approximation (MA) [4, 5], see Sec. 4.3 for a more detailed explanation. Hence, the applicability of both the BA and the MA rely on the condition $\alpha \ll \gamma_E$ as the relaxation rate of the environment leads to a decay of the memory kernel $\mathrm{Tr}_E\left\{\mathcal{L}_I\, e^{(\mathcal{L}_E+\mathcal{L}_S+Q\mathcal{L}_I)\tau}Q\mathcal{L}_I PR(t-\tau)\right\}$ on a time-scale of γ_E^{-1} and further allows to choose ρ_E according to the relation in Eq. (1.4).

In the light of these insights, one can interpret α as an expansion parameter. The NZE2 equation is expected to be accurate if time-scale separation is present which requires the parameter α to be "small" in the sense we have just understood above. Therefore, the standard projection operator approach can be interpreted as a "perturbative" approach in the same sense and the NZE2 is applicable in cases where the system-environment interaction is small with respect to the dynamics of the environment.

The self-consistent projection operator theory, in strong contrast, takes the back-action from the system onto the environment into account. Thus, it generalizes standard projection operator theories to physical scenarios without any time-scale separation. The rate α does not necessarily need to be small with respect to the local time scale γ_E (in fact in some cases it can be arbitrarily large, see Sec. 2.2.1) as exemplified in depth throughout all application of this thesis. As a consequence of adapting to the dynamical evolution of the environment, the self-consistent projection operator theory is applicable to a much larger class of physical scenarios than standard Nakajima-Zwanzig approaches. We now anticipate some results derived in detail in the following sections in order to underline the above statements on the basis of very general arguments.

The first major step of our theory is given by the introduction of the self-consistent Mori projector $P_t^S = \rho_E(t)\otimes\mathrm{Tr}_E$ which generalizes time-independent Mori projectors to a time-dependent projector. The time dependence is defined self-consistently with the full quantum state via $\rho_E(t) = \mathrm{Tr}_S R(t)$. The next major step is reached by deriving a generalized version of the NZE for the reduced state of the system given by

$$\dot{\rho}_S(t) = \mathcal{L}_S\rho_S(t) + \mathrm{Tr}_E\mathcal{L}_I P_t^S R(t) + \int_0^t d\tau\,\mathrm{Tr}_E\left\{\mathcal{L}_I\,\mathcal{D}(t,\tau)\mathcal{C}_{t-\tau}\mathcal{L}_I P_{t-\tau}^S R(t-\tau)\right\}. \tag{1.6}$$

Here, we have neglected any initial correlations, introduced the dynamical map $\mathcal{D}(t,\tau) = \hat{T}e^{\int_{t-\tau}^{t}(\mathcal{L}_E+\mathcal{L}_S+\mathcal{C}_{t'}\mathcal{L}_I)dt'}$ with the time-ordering operator $\hat{T}$ [23], see also Sec. 1.4, and defined the projector $\mathcal{C}_t = \mathbb{1} - \rho_E(t)\otimes\mathrm{Tr}_E - \rho_S(t)\otimes\mathrm{Tr}_S$ which projects onto the time-evolving system-environment correlations. We note, the action of the generalized Mori projector on the full quantum state gives $P_t^S R(t) = \rho_E(t)\otimes\rho_S(t)$.

By comparing Eqs. (1.5) and (1.6) we find the two counterparts $Q \leftrightarrow \mathcal{C}_t$ and most importantly $\rho_E \leftrightarrow \rho_E(t)$. Due to the time-dependence of the environmental state, Eq.(1.6) is not closed yet. Therefore, we additionaly introduce the Mori projector $P_t^E = \rho_S(t)\otimes\mathrm{Tr}_S$ which naturally appears in the definition of $\mathcal{C}_t$ as a direct consequence of the time-dependence in $\rho_E(t)$, see Sec. 1.4 for a detailed explanation. And finally, we derive a generalized version of the NZE for the reduced state of the environment given by

$$\dot{\rho}_E(t) = \mathcal{L}_E\rho_E(t) + \mathrm{Tr}_S\mathcal{L}_I P_t^E R(t) + \int_0^t d\tau\,\mathrm{Tr}_S\left\{\mathcal{L}_I\,\mathcal{D}(t,\tau)\mathcal{C}_{t-\tau}\mathcal{L}_I P_{t-\tau}^E R(t-\tau)\right\}, \tag{1.7}$$

where we have again neglected any initial system-environment correlations. Equations (1.6) and (1.7) form a closed set of coupled equations for the reduced states $\rho_S(t)$ and $\rho_E(t)$ and we refer to them as the generalized Nakajima-Zwanzig equations (gNZEs).

Just like the NZE we find the gNZEs to be formally exact for the reduced quantum states. However, they are not solvable in their full generality. Thus, we apply again the Born approximation which resides in the replacement $\mathcal{D}(t,\tau) \xrightarrow{\mathrm{BA}} e^{(\mathcal{L}_E+\mathcal{L}_S)\tau}$ within the integral kernels of the gNZEs. Hence, we have truncated the Dyson series, see Sec. 1.4, up to second order in the interaction $\mathcal{L}_I$. We refer to the resulting equations as the self-consistent Mori projector (c-MoP) equations.

In strong contrast to the BA on the level of the standard NZE, the c-MoP equations account for the back-action onto the environment by the last two terms on the right-hand side of Eq. (1.7). As a consequence the c-MoP equations do not require the smallness of the perturbation rate α with respect to the relaxation time γ_E of the environment.

1.3 The self-consistent Mori projector

We now turn to the presentation of a detailed derivation of the self-consistent Mori projector and the resulting effective equations of motion. In contrast to Sec. (1.2), we consider the general scenario of a physical setup described by Eq. (1.1) with an N-partite structure. The N parties could e.g. represent the different modes in a multi-mode setup, see Chapters 3 and 4, or a single lattice site (or clusters of lattice sites) in a lattice problem, see Chapter 2. Let us label the subsystems by using the index n with $n \in \{1, 2, ..., N\}$ and with reduced density matrices $\rho_n(t)$. Next, we shall pick one subsystem, say the subsystem with $n = n_0$, and aim for the derivation of an exact equation describing the time evolution of its reduced state $\rho_{n_0}(t)$.

For this purpose we will exploit the idea of projection operator techniques [4, 5] and introduce a projector P, similar to the Mori projector [21], which projects the full density matrix onto a relevant fraction $R_{\mathrm{rel}}(t) = PR(t)$ with $P(\cdot) = \rho_{\not n_0} \otimes \mathrm{Tr}_{\not n_0}(\cdot)$. The term "relevant" indicates that $R_{\mathrm{rel}}(t) = P_t R(t)$ contains all information needed to determine the exact expectation value of any operator A_{n_0} acting solely on the subpart n_0, i.e. $\langle A_{n_0}\rangle(t) = Tr\{A_{n_0} P_t R(t)\}$. Here, $\rho_{\not n_0}$ is a density matrix acting on the Hilbert space $\mathcal{H}_{\not n_0}$ of the remaining $N-1$ parties. However, $\rho_{\not n_0}$ is just a reference state and within the formal projection operator approach it is not unique. As a consequence, every result of the theory will indeed depend on the choice of the reference state as explained in Sec. (1.2).

The innovative step of our theory is to consider a time-dependent case for the density matrix $\rho_{\not n_0}(t)$ and therefore a time dependent projector. We define the self-consistent Mori projection operator [32] for an N-partite system by

$$P_t^{n_0}(\cdot) = \rho_{\not n_0}(t) \otimes \mathrm{Tr}_{\not n_0}(\cdot), \tag{1.8}$$

where the density matrix $\rho_{\not n_0}(t)$ is given by a factorized state of the reduced density matrices of all $N-1$ remaining constituents, i.e.

$$\rho_{\not n_0}(t) = \rho_1(t) \otimes \rho_2(t) \otimes ... \otimes \rho_{n_0-1}(t) \otimes \rho_{n_0+1}(t) \otimes ... \otimes \rho_N(t) = \bigotimes_{n \neq n_0} \rho_n(t)\,, \tag{1.9}$$

with the self-consistency condition for every reduced density matrix

$$\rho_n(t) = \mathrm{Tr}_{\not n} R(t). \tag{1.10}$$

Overall the action of the self-consistent Mori projector defined in Eq. (1.8) on the full quantum state results in a factorized state $\bigotimes_{n=1}^{N} \rho_n(t) = P_t^{n_0} R(t)$.

Most importantly, the time-dependence is introduced consistently with the time evolution of the full quantum state as we choose $\rho_n(t) = \mathrm{Tr}_{\not n}\{R(t)\}$. To emphasize the importance of the self-consistency condition we speak of a self-consistent Mori projector approach (**c-MoP**) as both the reduced density matrix of the subsystem of interest $\rho_{n_0}(t)$ and the state of the remainder $\rho_{\not n_0}(t)$ are determined consistently with the dynamics given by the full quantum state $R(t)$. To account for the partition of the whole system into N parts we have written the matrix $\rho_{\not n_0}(t)$ into a factorized form of reduced density matrices. Such an additional factorization into local density matrices is necessary, as otherwise, we will be confronted with an effective problem of $N-1$ parties for the treatment of $\rho_{\not n_0}(t)$. Especially for the application of our theory to quantum many-body problems, see Chapter 2, any other choice for $\rho_{\not n_0}(t)$ would lead to equations of motion where local quantities depend on non-local ones and thus not lead to the same reduction of the complexity of the description as $P_t^{n_0}$.

The time-dependence of the projector is in strong contrast to standard projection operator techniques where time-independent states are chosen as explained in Sec. (1.2). However, our theory also employs the complement of $P_t^{n_0}$ which projects out the irrelevant part of the density matrix $R_{irr}(t) = Q_t^{n_0} R(t)$ and is given by

$$Q_t^{n_0}(\cdot) = \left(\mathbb{1} - P_t^{n_0}\right)(\cdot), \tag{1.11}$$

where $\mathbb{1}$ is the identity mapping. We find the complementarity of the two subspaces $R_{rel}(t)$ and $R_{irr}(t)$ indicated by the characteristic features of projection operators

$$\begin{aligned} P_t^{n_0} Q_t^{n_0} &= Q_t^{n_0} P_t^{n_0} = 0 && (1.12)\\ P_t^{n_0} + Q_t^{n_0} &= \mathbb{1} && (1.13)\\ (P_t^{n_0})^2 &= P_t^{n_0} && (1.14)\\ (Q_t^{n_0})^2 &= Q_t^{n_0}. && (1.15) \end{aligned}$$

1.4 Exact equations of motion for reduced density matrices

To derive an exact equation of motion for the reduced state of the subsystem n_0, we first derive a set of equations for the two complements $P_t^{n_0} R(t)$ and $Q_t^{n_0} R(t)$ of the full density matrix $R(t)$. Then we state a formal solution for the irrelevant part and finally deduce a closed equation for the relevant part.

We start by rewriting Eq. (1.1) into

$$\dot{R}(t) = \mathcal{L}R(t) = \left(\underbrace{\mathcal{L}_{n_0} + \sum_{\substack{n=1 \\ n \neq n_0}}^{N} \mathcal{L}_n}_{=\mathcal{L}_0} + \underbrace{\sum_{n=1}^{Z} \mathcal{L}_{<n_0,n>} + \mathcal{L}_{I\not{n}_0}}_{=\mathcal{L}_I} \right) R(t)\,. \tag{1.16}$$

The superoperator $\mathcal{L}_{n_0}$ only acts on the subsystem of interest, while $\mathcal{L}_n$ describes the local dynamics of the n-th constituent or rather subpart. We group the local evolution operators into $\mathcal{L}_0$. The interaction between the subparts grouped into $\mathcal{L}_I$, is described by two fractions where $\sum_{n=1}^{Z} \mathcal{L}_{<n_0,n>}$ denotes the pairwise interaction of the subsystem n_0 with $Z \leq N-1$ different subsystems n, and $\mathcal{L}_{I\not{n}_0}$ accounts for any interaction between subsystems excluding the subsystem n_0. We allow for each of the Liouvillians to feature unitary or non-unitary terms with the restriction that all superoperators shall be the generators of completely positive, trace preserving maps of Lindblad type [22, 23]. By assigning $\mathcal{L}_{I\not{n}_0}$ to the interaction part $\mathcal{L}_I$, we treat all N subsystems on an equal footing being consistent with the choices made for the projection operator in Eq. (1.8) and especially with the factorized Ansatz in Eq. (1.9).

We proceed with the equation of motion for the relevant fraction of the full density matrix

$$\begin{aligned} \dot{R}_{rel} = \frac{d}{dt}\left(P_t^{n_0} R(t)\right) &= \dot{P}_t^{n_0} R(t) + P_t^{n_0} \dot{R}(t) = \dot{P}_t^{n_0}\, \mathbb{1} R(t) + P_t^{n_0} \mathcal{L}\, \mathbb{1} R(t) \\ &= \dot{P}_t^{n_0}(P_t^{n_0} + Q_t^{n_0})R(t) + P_t^{n_0}\mathcal{L}(P_t^{n_0} + Q_t^{n_0})R(t) \\ &= \left(\dot{P}_t^{n_0} + P_t^{n_0}\mathcal{L}\right) P_t^{n_0} R(t) + P_t^{n_0}\mathcal{L}Q_t^{n_0} R(t), \end{aligned} \tag{1.17}$$

where we have exploited the identity $\mathbb{1} = P_t^{n_0} + Q_t^{n_0}$, the full dynamics given by Eq. (1.1) and the relation $\dot{P}_t^{n_0} Q_t^{n_0} = 0$. Note the term $\dot{P}_t^{n_0} P_t^{n_0} R(t)$ arising from the explicit time dependence of the environmental state $\rho_{\not{n}_0}(t)$. Next, we use the operator equality $\dot{Q}_t^{n_0} = -\dot{P}_t^{n_0}$ to obtain an equation of motion for the irrelevant part of the full density matrix. In analogy to Eq. (1.17) we find

$$\dot{R}_{irr} = \frac{d}{dt}\left(Q_t^{n_0} R(t)\right) = \left(-\dot{P}_t^{n_0} + Q_t^{n_0}\mathcal{L}\right) P_t^{n_0} R(t) + Q_t^{n_0}\mathcal{L}Q_t^{n_0} R(t). \tag{1.18}$$

Now, we turn to the treatment of the environmental density matrix and its time derivative. Therefore, we employ the properties of a trace preserving generator given for all superoperators from Eq. (1.16). In particular, we will use that $\mathrm{Tr}_n \mathcal{L}_n(\cdot) =$

0, $\forall n$ and find

$$\begin{aligned}
\dot{P}_t^{n_0} P_t^{n_0} R(t) &= \dot{\rho}_{\not{n}_0}(t) \otimes \rho_{n_0}(t) = \sum_{m\neq n_0} \dot{\rho}_m(t) \otimes \bigotimes_{n\neq m} \rho_n(t) \\
&= \sum_{m\neq n_0} \mathrm{Tr}_{\not{m}}\{\dot{R}(t)\} \otimes \bigotimes_{n\neq m} \rho_n(t) \\
&= \sum_{m\neq n_0} \mathrm{Tr}_{\not{m}}\left\{\left(\sum_{n=1}^{N} \mathcal{L}_n + \mathcal{L}_I\right) R(t)\right\} \otimes \bigotimes_{n\neq m} \rho_n(t) \\
&= \sum_{m\neq n_0} \left[\mathrm{Tr}_{\not{m}}\{\mathcal{L}_I R(t)\} + \mathcal{L}_m \rho_m(t)\right] \otimes \bigotimes_{n\neq m} \rho_n(t) \\
&\equiv \sum_{m\neq n_0} \mathcal{L}_m P_t^{n_0} R(t) + P_t^{\not{n}_0} \mathcal{L}_I (P_t^{n_0} + Q_t^{n_0}) R(t),
\end{aligned} \tag{1.19}$$

where, in analogy to the projector defined in Eq. (1.8), we have introduced the projector

$$P_t^{\not{n}_0}(\cdot) \equiv \sum_{m\neq n_0} P_t^m(\cdot) = \sum_{m\neq n_0} \bigotimes_{n\neq m} \rho_n(t) \otimes \mathrm{Tr}_{\not{m}}\{\cdot\}. \tag{1.20}$$

We observe that for an N-partite physical setup we have an ensemble of N projectors P_t^n with $n \in \{1, 2, ..., N\}$. By picking one part with $n = n_0$ as the subsystem of interest, we have picked $P_t^{n=n_0} = P_t^{n_0}$ as our projector of interest. Now, we find a connection between all N projectors due to the explicit time dependence of the self-consistent Mori projector or rather the time-dependence of the state $\rho_{\not{n}_0}(t)$. We stress that the projector $P_t^{\not{n}_0}$, see Eq. (1.20), depends on $P_t^{n_0}R(t)$ via $\rho_{n_0}(t) = \mathrm{Tr}_{\not{n}_0}\{P_t^{n_0}R(t)\}$. However, there is no dependence on $Q_t^{n_0}R(t)$ which will allow us to find a closed equation for the relevant part of the density matrix.

In addition to Eq. (1.19), we employ $P_t^{n_0}\mathcal{L}_{n_0}(\cdot) = \mathcal{L}_{n_0}P_t^{n_0}(\cdot)$ and $\mathrm{Tr}_n\mathcal{L}_n(\cdot) = 0$, $\forall n$ to find the relations

$$\begin{aligned}
Q_t^{n_0}\mathcal{L}P_t^{n_0}R(t) &= \sum_{m\neq n_0} \mathcal{L}_m P_t^{n_0} R(t) + Q_t^{n_0}\mathcal{L}_I P_t^{n_0} R(t) \\
Q_t^{n_0}\mathcal{L}Q_t^{n_0}R(t) &= \sum_{m} \mathcal{L}_m Q_t^{n_0} R(t) + Q_t^{n_0}\mathcal{L}_I Q_t^{n_0} R(t) \\
&= \mathcal{L}_0 Q_t^{n_0} R(t) + Q_t^{n_0}\mathcal{L}_I Q_t^{n_0} R(t).
\end{aligned} \tag{1.21}$$

Using relations (1.19) and (1.21), we restate the equation of motion (1.18) for the irrelevant part of the full density matrix

$$\begin{aligned}
\frac{d}{dt}(Q_t^{n_0}R(t)) &= \left(-\dot{P}_t^{n_0} + Q_t^{n_0}\mathcal{L}\right) P_t^{n_0}R(t) + Q_t^{n_0}\mathcal{L}Q_t^{n_0}R(t) \\
&= \mathcal{C}_t\mathcal{L}_I P_t^{n_0}R(t) + \left(\mathcal{C}_t\mathcal{L}_I + \mathcal{L}_0\right) Q_t^{n_0}R(t),
\end{aligned} \tag{1.22}$$

where we have introduced the correlation operator

$$\mathcal{C}_t = -P_t^{\not{n}_0} + Q_t^{n_0} = \mathbb{1} - \sum_{n=1}^{N} P_t^n\,. \tag{1.23}$$

Before we state the formal solution of Eq. (1.22), it is convenient to introduce a shorthand notation for the time-propagator $\mathcal{D}(t,t') = \hat{T}\exp\{\int_{t'}^{t} dt''(\mathcal{C}_{t''}\mathcal{L}_I + \mathcal{L}_0)\}$ including the time-ordering operator $\hat{T}$ which orders any product of superoperators such that the time arguments increase from right to left [4, 23]. By iteratively integrating Eq. (1.22) we are able to cast the formal solution of $Q_t^{n_0}R(t)$, for a given state $R(t_0)$ at an initial time t_0, into the form

$$Q_t^{n_0}R(t) = \int_{t_0}^{t} dt'\ \mathcal{D}(t,t')\mathcal{C}_{t'}\mathcal{L}_I P_{t'}^{n_0}R(t') + \mathcal{D}(t,t_0)\underbrace{Q_{t_0}^{n_0}R(t_0)}_{=0}. \tag{1.24}$$

In the context of this work, we focus on a physical situation with a factorized initial state, i.e. $Q_{t_0}^{n_0}R(t_0) = 0$. One can verify that the right hand side of Eq. (1.24) is indeed a solution of Eq. (1.22) by simply taking the derivative of Eq. (1.24) with respect to the time t and by considering that $\frac{d}{dt}\mathcal{D}(t,t') = (\mathcal{C}_t\mathcal{L}_I + \mathcal{L}_0)\mathcal{D}(t,t')$.

Finally, we insert the formal solution of Eq. (1.24) for $Q_t^{n_0}R(t)$ into Eq. (1.17) and obtain an exact equation of motion for the relevant part $R_{\text{rel}}(t)$ of the density matrix, it reads

$$\begin{aligned}\frac{d}{dt}(P_t^{n_0}R(t)) = \dot{P}_t^{n_0}\mathcal{L}P_t^{n_0}R(t) + \mathcal{L}_{n_0}P_t^{n_0}R(t) + P_t^{n_0}\mathcal{L}_I P_t^{n_0}R(t)\\ + P_t^{n_0}\mathcal{L}_I\int_{t_0}^{t} dt'\ \mathcal{D}(t,t')\mathcal{C}_{t'}\mathcal{L}_I P_{t'}^{n_0}R(t').\end{aligned} \tag{1.25}$$

We emphasize again, that this equation is an exact and closed equation for the relevant part of the density matrix. The irrelevant part of the density matrix has been integrated out of Eq. (1.25) which may be viewed as a generalization of the prominent Nakajima-Zwanzig equation for open systems as shown in Sec. (1.2).

In order to obtain an exact equation for the reduced state of the subpart n_0, we apply the trace operation $\text{Tr}_{\not{n}_0}$ on both sides of Eq. (1.25). Because the time derivative is a trace preserving operation, we clearly find that $\text{Tr}_{\not{n}_0}\{\dot{P}_t^{n_0}(\cdot)\} = 0$. Similarly, we find $\text{Tr}_{\not{n}_0}\mathcal{L}_I(\cdot) = \sum_{n=1}^{Z}\text{Tr}_{\not{n}_0}\mathcal{L}_{<n_0,n>}$ as $\mathcal{L}_{I\not{n}_0}$, see Eq. (1.16), is the generator of a trace preserving map acting solely on the Hilbert space of the remaining $N-1$ subparts excluding the subpart n_0, and hence $\text{Tr}_{\not{n}_0}\mathcal{L}_{I\not{n}_0} = 0$. Finally, we state an effective equation, given by

$$\boxed{\begin{aligned}\dot{\rho}_{n_0}(t) = \mathcal{L}_{n_0}\rho_{n_0}(t) + \sum_{n=1}^{Z}\text{Tr}_{\not{n}_0}\{\mathcal{L}_{<n_0,n>}P_t^{n_0}R(t)\}\\ + \sum_{n=1}^{Z}\text{Tr}_{\not{n}_0}\{\mathcal{L}_{<n_0,n>}\int_{t_0}^{t} dt'\ \mathcal{D}(t,t')\mathcal{C}_{t'}\mathcal{L}_I P_{t'}^{n_0}R(t')\},\end{aligned}} \tag{1.26}$$

for the reduced density matrix $\rho_{n_0}(t)$. This equation depends on all the remaining density matrices $\rho_n(t)$ with $n \neq n_0$. In order to obtain a closed set of N equations of motion for the reduced density matrices $\rho_1(t), \rho_2(t), ..., \rho_N(t)$ we exploit each of the generalized Mori projectors P_t^n and derive an exact equation of motion for each of the reduced states $\rho_n(t)$ in analogy to Eq. (1.26). We refer to this set of equations as the generalized Nakajima-Zwanzig equations or alternatively as the exact self-consistent Mori projector (c-MoP) equations.

The exact c-MoP equations exactly describes the dynamics of reduced density matrices for individual subsystems of an N-partite quantum few- or many-body system of arbitrary size and geometry. The N-partite system may be closed or it may even be open so that its dynamics is not necessarily unitary. Equation (1.26) takes the correlations between subsystems explicitly into account via the action of the projection operator $\mathcal{C}_t$, see Eq. (1.23). Moreover, whenever the total state $R(t)$ is pure, the growth of the von Neuman entropy of the states $\rho_n(t)$, as described by Eq. (1.26), accounts for the entanglement that is built up between each individual subsystem and its surrounding. Since the first line of Eq. (1.26) for this case describes a unitary evolution, entanglement between subsystems is only taken into account via the second line of Eq. (1.26).

1.5 Dyson Series, Born and Mean-field Approximations

The exact c-MoP equations are often exceedingly difficult to solve in full generality. Their great value as compared to the Liouville-von Neumann equation resides rather in the fact that they provide a starting ground for further approximations. In particular, due to the exponential structure of the time-propagator $\mathcal{D}(t,t')$, we can expand equation (1.26) as a Dyson series in powers of the system-environment interaction $\mathcal{L}_I$,

$$\begin{aligned}\dot{\rho}_{n_0}(t) = \mathcal{L}_{n_0}\rho_{n_0}(t) + \sum_{n=1}^{Z} \mathrm{Tr}_{\not{n}_0}\mathcal{L}_I P_t^{n_0} R(t) \\ + \mathrm{Tr}_{\not{n}_0}\mathcal{L}_I \int_{t_0}^{t} dt' e^{\mathcal{L}_0(t-t')}\, \mathcal{C}_{t'}\mathcal{L}_I P_{t'}^{n_0} R(t') + \sum_{m=3}^{\infty} \mathcal{Y}_m \,,\end{aligned} \tag{1.27}$$

where the m-th order terms read,

$$\begin{aligned}\mathcal{Y}_m =& \mathrm{Tr}_{\not{n}_0}\mathcal{L}_I \int_{t_0}^{t} dt' \int_{t'}^{t} dt_{m-1}\, e^{\mathcal{L}_0(t-t_{m-1})}\, \mathcal{C}_{t_{m-1}}\mathcal{L}_I \\ &\times \int_{t'}^{t_{m-1}} dt_{m-2}\, e^{\mathcal{L}_0(t_{m-1}-t_{m-2})}\, \mathcal{C}_{t_{m-2}}\mathcal{L}_I \\ &\times \cdots \times \int_{t'}^{t_3} dt_2\, e^{\mathcal{L}_0(t_3-t_2)}\, \mathcal{C}_{t_2}\mathcal{L}_I e^{\mathcal{L}_0(t_2-t')}\, \mathcal{C}_{t'}\mathcal{L}_I\, P_{t'}^{n_0} R(t') \,,\end{aligned} \tag{1.28}$$

with a time ordering as $t_0 \leq t' \leq t_2 \leq ... \leq t_{m-1} \leq t$. In order to understand the physical processes described by the m-th order correction, for $m \geq 2$, it is convenient to read Eq. (1.28) from right to left. There are always m different chronologically ordered points in time $\{t_0, t_1, ..., t_m\}$, with $t_1 = t'$ and $t_m = t$. At each point in time t_j, for $1 \leq j \leq m-1$, we find an interaction vertex described by the superoperator $\mathcal{C}_{t_j}\mathcal{L}_I$. The interaction vertices are linked via interaction-free time evolution $e^{\mathcal{L}_0(t_{j+1}-t_j)}$.

At the very right end of Eq. (1.28) we find the factorized state $P_{t'}^{n_0}R(t')$ or rather $P_{t_1}^{n_0}R(t_1)$ which, by maintaining the order in $\mathcal{L}_I$, can be rewritten into $P_{t_1}^{n_0}R(t_1) = e^{\mathcal{L}_0(t_1-t_0)}P_{t_0}^{n_0}R(t_0) = e^{\mathcal{L}_0(t_1-t_0)}R(t_0)$. Therefore, the term $\mathcal{Y}_m$ describes a process where the initially factorized state $R(t_0)$ evolves according to the interaction-free generator $\mathcal{L}_0$ to the first vertex point at $t_1 = t'$. At the vertex the action of the superoperator $\mathcal{L}_I$ builds up correlations which are then projected out by the action of $\mathcal{C}_{t_1}$. The resulting operator given by $A \equiv \mathcal{C}_{t_1}\mathcal{L}_I e^{\mathcal{L}_0(t_1-t_0)}R(t_0)$ solely contains the correlated part between any constituents of the entire N-partite setup which has been build up by the action of $\mathcal{L}_I$.

Similarly, this process continues from one point in time t_j to the following one t_{j+1} successively building up correlations until the last point in time $t = t_m$ is reached. The interaction vertex at the present time $t = t_m$, however, is not described by the superoperator $\mathcal{C}_t\mathcal{L}_I$ but rather by $\mathrm{Tr}_{\not{n}_0}\mathcal{L}_I \equiv \mathrm{Tr}_{\not{n}_0}P_t^{n_0}\mathcal{L}_I$. Clearly, the superoperator $P_t^{n_0}$ projects out the relevant part of the dynamics of the reduced density matrix $\rho_{n_0}(t)$.

In summary, we conclude that the m-th order corrections for $m \geq 2$ contain the influence of correlations which arise due to non-Markovian memory effects in the interaction between the subpart n_0 and the remaining $N-1$ subparts. In turn, the terms up to first order in $\mathcal{L}_I$ do neither contain any correlations nor non-Markovian memory effects. Hence, we expect a large improvement in the quality of the approximations by going from first order in $\mathcal{L}_I$ to second order in $\mathcal{L}_I$.

Motivated by these insights we apply the so-called Born approximation [4, 5] which takes all terms up to second order into account. By dropping all terms proportional to $\mathcal{L}_I$ from the exponent of the dynamical map $\mathcal{D}(t,t')$, we state an equation to which we will refer as the c-MoP equation in Born approximation,

$$\begin{aligned} \dot{\rho}_{n_0}(t) &= \mathcal{L}_{n_0}\rho_{n_0}(t) + \sum_{n=1}^{Z} \mathrm{Tr}_n\{\mathcal{L}_{<n_0,n>}\rho_n(t)\otimes\rho_{n_0}(t)\} \\ &+ \sum_{n=1}^{Z}\mathrm{Tr}_n\mathcal{L}_{<n_0,n>}\int_{t_0}^{t}dt'\,\mathcal{D}_{<n_0,n>}(t,t')\mathcal{C}_{t'}^{<n_0,n>}\mathcal{L}_{<n_0,n>}\rho_n(t')\otimes\rho_{n_0}(t'), \end{aligned} \tag{1.29}$$

with the shorthand notation $\mathcal{D}_{<n_0,n>}(t,t') \equiv e^{(t-t')(\mathcal{L}_n+\mathcal{L}_{n_0})}$ for the dynamical map describing the free local evolution of the n_0-th constituent and its Z different interaction partners, and with the shorthand notation for the pairwise correlation projector

$$\mathcal{C}_{t'}^{<n_0,n>} \equiv \mathbb{1} - \rho_n(t')\otimes\mathrm{Tr}_n - \rho_{n_0}(t')\otimes\mathrm{Tr}_{n_0}.$$

Interestingly, in the Born approximation we only find "non-mixing" terms proportional to $\mathcal{L}_{<n_0,n>}\mathcal{L}_{<n_0,m>}\delta_{n,m}$ and all possible terms containing $\mathcal{L}_{I\not{n}_0}$ vanish as well. In fact, this is the direct consequence of a factorized state Ansatz for $\rho_{\not{n}_0}(t)$, see Eq. (1.9).

We emphasize again that whereas one could derive an exact equation for ρ_{n_0} for any choice of the (reference) state $\rho_{\not n_0}$ fulfilling the initial conditions, the quality of the approximation in Eq. (1.29) depends on the ansatz for $\rho_{\not n_0}$. Here, our time dependent and self-consistent projector, defined in Eqs. (1.8) and (1.9), appears to be the best ansatz to account for a highly dynamical quantum few- or many-body environment, see Chapters 2 and 3. A Born or rather Born-Markov approximation as applied in open system theory is not accurate for the physical models considered in this work since reduced density matrices of the system of interest and its surrounding are treated on an equal footing and correlation functions of the surrounding can thus not be expected to decay faster than the dynamics generated by the coupling between subsystems. In fact, for models with time scale separations, which are the basis of approaches using adiabatic elimination [33] or approximate Schrieffer-Wolff transformations [34], Eq. (1.26) reduces to a standard master equation [4].

1.5.1 Mean-field approximation

The right hand side of Eq. (1.29) shows three terms, which are zeroth, first and second order in $\mathcal{L}_{<n_0,n>}$, respectively. The zeroth order term $\mathcal{L}_{n_0}\rho_{n_0}(t)$ denotes the free local evolution of the subpart n_0 which becomes exact for cases without interaction, i.e. $\mathcal{L}_{<n_0,n>} = 0$. The first and zeroth order terms taken together are equivalent to the well-known mean-field or Gutzwiller approach which has been exploited with remarkable success in equilibrium physics [9, 18, 35] as well as non-equilibrium physics [26, 36–39]. In the mean-field approach the full quantum state $R(t)$ is approximated as a product state on the level of the full Liouville von-Neumann equation [40]

$$\dot{R}(t) = \mathcal{L}R(t) \xrightarrow{\text{mean-field}} \frac{d}{dt}\left(\bigotimes_{n=1}^{N}\rho_n(t)\right) = \mathcal{L}\left(\bigotimes_{n=1}^{N}\rho_n(t)\right). \tag{1.30}$$

By applying the trace operation $\mathrm{Tr}_{\not n_0}$ one finds the first two terms on the right hand side of Eq. (1.29). Mean-field can thus be understood as an approximation to linear order in $\mathcal{L}_I$ of the exact self-consistent projection operator equation, see Eq. (1.26). Our theory therefore forms a systematic generalization of mean-field approaches.

As the non-Markovian properties, the explicit consideration of correlations via the projector $\mathcal{C}_t$, and entanglement between subsystems are only present in terms of higher than linear order in $\mathcal{L}_I$, Eq. (1.29) yields a different quality of approximation than mean-field. We will show that this is indeed the case in all examples to follow.

1.5.2 Notes on the superposition principle and the positivity

Since the Liouville von-Neumann equation, see Eq. (1.1), obeys a superposition principle, one might wonder whether this is still respected by the non-linear equations of our approach. The non-linearity can for example be understood from the term $\mathcal{C}_t\rho_n(t) \sim \rho_n(t)^2$ appearing in the integral kernel of Eq. (1.26) or more directly by writing the equation as $\dot{\rho}_{n_0}(t) = \mathcal{L}^{\mathrm{eff}}(\rho_1(t), \rho_2(t), ..., \rho_N(t))\rho_{n_0}(t)$ with an effective Liouvillian $\mathcal{L}^{\mathrm{eff}}$ depending on the reduced states of all N subparts.

In this context we first note that Eq. (1.26) does in general no longer allow for a superposition principle for $R(t)$, in contrast to Eq. (1.1). Nonetheless, for two reduced density matrices ρ_{n_0} and ρ'_{n_0} that are solutions of Eq. (1.26), their convex sum $c\rho_{n_0} + (1-c)\rho'_{n_0}$ $(0 \leq c \leq 1)$ is also a solution since Eq. (1.26) is exact and its solutions are therefore identical to $\mathrm{Tr}_{\not{n}_0} R$. Despite its nonlinearity, Eq. (1.26) thus fulfills a superposition principle for reduced density matrices ρ_{n_0}. Due to the applied approximations, the superposition principle of Eq. (1.26) for ρ_{n_0} does not necessarily hold for Eq. (1.29). We have confirmed that it does hold for systems where we found Eq. (1.29) to give exact results, see e.g. in Sec. 2.2.1 for the solution of Eq. (2.8), but in general, the superposition principle is lost whenever Eq. (1.29) ceases to be a good approximation.

Thus, the breaking of the superposition principle on the level of the relevant quantity, here the reduced states, is only a consequence of an approximation within the exact theory. In the literature one finds many more approximative theories whose corresponding dynamical equations are nonlinear and thus break the superposition principle. Among them the most prominent are mean-field theories [18, 40], nonlinear Boltzmann equations [41] or the semi-classical equations in the field of nonlinear optics [42].

Next, we remark that the c-MoP equations preserve the trace and the hermiticity but within the Born approximation they do not guarantee for the positivity of the density matrix. Such an issue is not unusual for projection operator theories, in fact, the same conditions can e.g. be found in the well established Redfield equations [43, 44] or rather the more general case of time-convolutionless projection operator methods [4]. Obviously whenever the c-MoP equations provide a good approximation, they will yield a positive density matrix. Hence the positivity of the eigenvalues of the reduced density matrices can be used as a consistency test for the accuracy of the approximation.

1.5.3 The c-MoP equations for unitary interactions

In this section we will derive a useful form of the c-MoP equations in Born approximation for all cases in which the interaction Liouvillian is unitary. Moreover, we will consider two-part interactions between any of the subparts in the full quantum system and thus we write

$$\mathcal{L}_I(\cdot) = -i \sum_{n,m} \left[\vec{A}_n \cdot \vec{B}_m, (\cdot) \right] , \tag{1.31}$$

with vectors $\vec{A}_n$ and $\vec{B}_m$ whose elements contain operators that solely act on the subpart n and m with $n, m \in \{1, 2, ..., N\}$, respectively. We further demand the operator $\sum_{n,m} \vec{A}_n \cdot \vec{B}_m$ to be hermitian.

It proves useful to investigate the action of the correlation projector $\mathcal{C}_t = \mathbb{1} - \sum_n P_t^n$ on the operator $\mathcal{L}_I P_t^{n_0} R(t)$ with the interaction defined as in Eq. (1.31) and with $P_t^{n_0} R(t) = \bigotimes_{n=1}^N \rho_n(t)$. We find

$$\mathcal{C}_t \mathcal{L}_I \bigotimes_{n=1}^{N} \rho_n(t) = -i \sum_{n,m} \sum_{\mu,\nu} \left[\delta A_n^\mu \, \delta B_m^\nu \delta_{\mu,\nu} \, , \bigotimes_{n=1}^{N} \rho_n(t) \right] , \tag{1.32}$$

with the vector components of the operators $\vec{A}$ and $\vec{B}$ denoted by the indices μ, ν, the Kronecker-delta $\delta_{\mu,\nu}$ which takes the value 1 for $\mu = \nu$ and the value 0 in any other case, and the fluctuation operators

$$\delta A_n^\mu(t) = A_n^\mu - \mathrm{Tr}_n\{A_n^\mu \rho_n(t)\} \text{ and } \delta B_m^\nu(t) = B_m^\nu - \mathrm{Tr}_m\{B_m^\nu \rho_m(t)\} \, . \tag{1.33}$$

As a result, the c-MoP equations in Born approximation for the reduced density matrix of the subpart n_0 are given by

$$\begin{aligned} \dot{\rho}_{n_0}(t) = \mathcal{L}_{n_0} \rho_{n_0}(t) + \sum_{n=1}^{Z} \sum_{\mu,\nu} \Big\{ (-i) \left[\mathrm{Tr}\{B_n^\mu \rho_n(t)\} \, A_{n_0}^\nu \delta_{\mu,\nu} \, , \rho_{n_0}(t) \right] \\ - \left[A_{n_0}^\nu \, , \int_0^t dt' \, e^{\mathcal{L}_{n_0}(t-t')} \left\{ \delta A_{n_0}^\mu(t') \rho_{n_0}(t') \, d_n^{\mu,\nu}(t,t') - \rho_{n_0}(t') \delta A_{n_0}^\mu(t') \, s_n^{\mu,\nu}(t,t') \right\} \right] \Big\} , \end{aligned} \tag{1.34}$$

with the two-time correlation functions of the n-th subpart

$$\begin{aligned} d_n^{\mu,\nu}(t,t') &= \mathrm{Tr}_n\{B_n^\nu e^{\mathcal{L}_n(t-t')} \delta B_n^\mu(t') \rho_n(t')\} \\ s_n^{\mu,\nu}(t,t') &= \mathrm{Tr}_n\{B_n^\nu e^{\mathcal{L}_n(t-t')} \rho_n(t') \delta B_n^\mu(t')\}. \end{aligned} \tag{1.35}$$

Throughout the thesis we will use the term c-MoP equation to refer to the simplified form of the self-consistent Mori projector equations given by Eq. (1.34) and Eq. (1.35). Note, that our theory is in principle not restricted to unitary interaction Liouvillians with two-body terms.

1.5.4 Scaling behavior of the c-MoP equations

The most striking advantage of any projection operator theory and in particular of the c-MoP theory is the reduction of the complexity of the problem. Clearly, the complexity of the Liouville-von Neumann equation (1.1) scales exponentially with the number of subparts as the total Hilbert space $\mathcal{H}$ can be written as $\mathcal{H} = \mathcal{H}_1 \otimes \mathcal{H}_2 \otimes ... \otimes \mathcal{H}_N$, with $\mathcal{H}_n$ denoting the local Hilbert space of each subpart $n \in \{1, 2, ..., N\}$. In general, the huge number of degrees of freedom thus renders an exact description infeasible, even if one resorts to numerical approaches.

In contrast, the complexity of the c-MoP equations scales linearly, i.e. it scales as $\mathcal{H}_1 + \mathcal{H}_2 + ... + \mathcal{H}_N$, with the number of subparts. The self-consistent Mori-projector theory thus offers a very significant reduction of complexity. However, whereas the Liouville-von Neumann equation is local in time the c-MoP equations exhibit an integro-differential structure which leads, despite the favorable scaling for the required Hilbert space dimension, to a more complicated form. Throughout the thesis we will introduce methods to deal with the difficulty of non-Markovian c-MoP equations which are adapted to the physical models at hand.

Chapter 2

Self-Consistent Projection Operator Theory for Quantum Many-Body Systems

2.1 Introduction

Quantum many-body systems give rise to a number of intriguing phenomena such as quantum phase transitions [9], topological insulators [45, 46] or high-temperature superconductivity [47]. Yet, their description is a formidable challenge as the dimension of the Hilbert space grows exponentially with the number of its constituents. Thus, the large set of degrees of freedom renders an exact description in general infeasible, even if one resorts to numerical approaches.

Exceptions to this intractability are quantum systems that do not explore their entire Hilbert space, where numerical optimization approaches such as the Density Matrix Renormalization Group [48] become efficient descriptions. Alternatively one may aim for only obtaining a subset of information that is the information of interest about the quantum state of the entire system and try to find accurate and efficient approximations for the sought quantities. Mean-field approaches [17] can be understood as representatives of this strategy as they only predict properties of a single constituent of the many-body system [9, 18].

In the same spirit, equations of motion for the part of the quantum state that is of interest to the researcher have been derived in the context of open quantum systems where the density matrix of the entire system is split into a ’relevant’ part describing the subsystem of interest and a complementary ’irrelevant’ part with the help of the Mori projector [3, 4, 21]. The guiding idea for a projection operator method in the context of a many-body lattice problem could consist in restricting the interest on an individual lattice site or clusters of lattice sites. Thus, the resulting effective theory will grant us with an equation of motion for the reduced density matrices and lead to a similar reduction of complexity as Mean-field approaches. We show

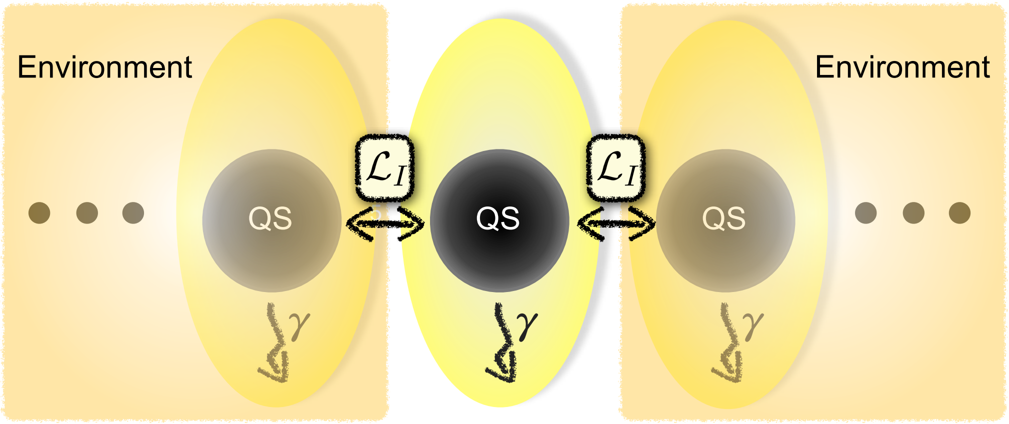

Figure 2.1: Illustration of our approach for a one-dimensional lattice. We consider a quantum many-body system where each subsystem (QS) has some unitary and potentially some non-unitary dynamics (indicated by the rate γ). The subsystems are coupled via the interaction $\mathcal{L}_I$. Within our theory we pick one QS of interest and trace out the remaining constituents.

a sketch of such an idea in Fig. 2.1 where we consider one local lattice site as the "system of interest" and treat the remainder of the lattice as the "environment". As we have understood from the arguments presented in Sec. 1.2, standard open system theories rely on a time-scale separation between system and environment and therefore they will not be able to account for the general case of a dynamically evolving environment.

With the self-consistent projection operator theory we introduce an approach to the calculation of local properties of a quantum many-body system. We have presented a detailed derivation of our theory in Chapter 1 and in particular we have argued that our approach does not require a clear separation of time scales. Therefore, we conclude that the time-dependent and self-consistent Mori projector is a very accurate ansatz to account for a highly dynamical quantum many-body environment.

As we show in what follows in this chapter, our theory is capable of describing stationary states and dynamical evolutions for a situation in which one is only interested in the physics of a part of the system under study. Most notably, it efficiently predicts non-equilibrium dynamics for long times, offers a methodology which applies to two- and higher-dimensional systems in the same way as to one-dimensional ones, and can directly and efficiently calculate stationary states of many-body systems with dissipation.

An increasing number of experimental settings, including arrays of Josephson junctions [49], ultra-cold atoms [50], ion traps [51, 52] and arrays of coupled cavities [24], offer the possibility to generate effective many-particle systems and hence trigger substantial research activity. One prominent application of these systems are investigations of the unitary dynamics of non-equilibrium states in closed systems [53, 54]. As a first test of the performance of our method we thus apply it to calculate local properties of time-evolving non-equilibrium states in closed systems. We find that it predicts these quantities with very high accuracy for a time range that strongly increases with the size of the considered subsystem.

In many experimental situations, the samples will however suffer from decoherence and dissipation. Hence dissipative and driven-dissipative quantum many-body systems are currently receiving enormous interest in the search for strongly correlated steady states and non-equilibrium analogs of quantum phase transitions [23, 25, 26, 36, 52, 55–57]. As a second test we thus apply our method to driven and dissipative quantum many-body systems and find that it predicts the values of local quantities with very good accuracy. Finally, we will exploit our approach in one and two spatial dimensions to investigate the dissipative mean-field phase transition of first order appearing in the steady state of the driven-dissipative Heisenberg XX model. We refer to this transition as the "quantum to classical transition" since in one of the phases the spins behave purely classically while in the other the spins exhibit highly non-classical behavior.

The remainder of Chapter 2 is organized as follows. In section 2.2 we show the applicability and accuracy of our method for both, the unitary dynamics in closed quantum systems 2.2.1, and non-unitary dynamics in one-dimensional 2.2.2 and two-dimensional 2.2.3 open quantum systems. Finally, we apply our method to the resonantly driven and locally dissipative Heisenberg XX model to investigate its steady state phases in 1D and 2D in Sec. 2.3 where we also discuss possible drawbacks of the c-MoP formalism as performed in this chapter that might arise in spatial dimension two and higher.

2.2 Applications and accuracy tests

We have laid the foundations and derived the main results of our theory in Chapter 1, and now we will turn to test the accuracy of Eq. (1.29) in applications to one-dimensional many-body lattice systems where either exact solutions or very accurate t-DMRG simulations are available for comparison. In doing so we focus on a lattice of two-level systems or spins and extensions thereof which include coherent drives and relaxation of individual spins. This model (with periodic boundary conditions) is described by Eq. (1.1) with ($\hbar = 1$),

$$\begin{aligned}\dot{R}(t) = -i &\left[\sum_{n=1}^{N}\left(\Delta\sigma_n^\dagger\sigma_n + \frac{\Omega}{2}(\sigma_n^\dagger + \sigma_n)\right) - J\sum_{n=1}^{N}\left(\sigma_n^\dagger\sigma_{n+1} + \sigma_n\sigma_{n+1}^\dagger\right), R(t)\right] \\ &+ \frac{\gamma}{2}\sum_{n=1}^{N}\left(2\sigma_n R(t)\sigma_n^\dagger - \sigma_n^\dagger\sigma_n R(t) - R(t)\sigma_n^\dagger\sigma_n\right) \equiv \mathcal{L}R(t)\,,\end{aligned} \tag{2.1}$$

where $\sigma_n = |0_n\rangle\langle 1_n|$ is the de-excitation operator on site n, N the number of lattice sites, and $\sigma_{N+1} = \sigma_1$. We have written the Hamiltonian in a rotating frame such that, $\Delta = \omega - \omega_L$ is the detuning between spin transition frequency ω and drive frequency ω_L. J is the tunneling rate between nearest-neighbor sites, and Ω the drive amplitude. The model of Eq. (2.1) allows us to study both, the unitary dynamics of a closed system as well as stationary states of driven-dissipative systems.

Within our c-MoP theory we split the entire quantum system of N lattice sites into identical subgroups or rather clusters containing a total of M adjacent lattice sites. Consistent with the notation throughout Chapter 1, each subgroup shall be described by the reduced density matrix $\rho_n^M(t)$ for the n-th subgroup with M sites. The index n thus labels the clusters. Accordingly, we split the full Liouvillian $\mathcal{L}$ consistent with Eq. (1.16) into parts which describe the local dynamics of each subgroup and the interaction between any of the parts. The former is given by

$$\begin{aligned}\mathcal{L}_n(\cdot) = -i &\left[\sum_{j_n=1}^{M} \left(\Delta \sigma^\dagger_{j_n}\sigma_{j_n} + \frac{\Omega}{2}(\sigma^\dagger_{j_n} + \sigma_{j_n}) \right) - J \sum_{j_n=1}^{M-1} \left(\sigma^\dagger_{j_n}\sigma_{j_{n+1}} + \sigma_{j_n}\sigma^\dagger_{j_{n+1}} \right), (\cdot) \right] \\ &+ \frac{\gamma}{2} \sum_{j_n=1}^{M} \left(2\sigma_{j_n}(\cdot)\sigma^\dagger_{j_n} - \sigma^\dagger_{j_n}\sigma_{j_n}(\cdot) - (\cdot)\sigma^\dagger_{j_n}\sigma_{j_n} \right),\end{aligned} \tag{2.2}$$

where we have introduced the index $j_n \in \{1, 2, ..., M\}$ which labels the lattice sites within the n-th cluster. In addition, the interaction Liouvillian reads

$$\mathcal{L}_I = iJ \left[\sum_{n=1}^{N/M} \sum_{j_n=1}^{M} \sum_{j_{n+1}=1}^{M} \left(\sigma^\dagger_{j_n}\sigma_{j_{n+1}} + \sigma_{j_n}\sigma^\dagger_{j_{n+1}} \right) \delta_{j_n,M}\delta_{j_{n+1},1}, (\cdot) \right], \tag{2.3}$$

where the Kronecker symbol δ, see Eq. (1.32), guarantees that the tunneling takes place only on the boundaries of the clusters. For example, site $j_n = M$ of the n-th site shall tunnel to the site $j_{n+1} = 1$ of the $(n+1)$-th cluster. Without loss of generality we shall assume N/M to take on integer values. Note, we can rewrite the term $\sigma^\dagger_{j_n}\sigma_{j_{n+1}} + \sigma_{j_n}\sigma^\dagger_{j_{n+1}}$ into a vector form $\vec{A}_n \cdot \vec{B}_{n+1}$ consistent with the notation used in Eq. (1.31) such that $\vec{A}_n = \{\sigma^\dagger_{j_n}, \sigma_{j_n}\}^\top$ and $\vec{B}_{n+1} = \{\sigma_{j_{n+1}}, \sigma^\dagger_{j_n}\}^\top$.

Instead of solving a set of coupled c-MoP equations for the reduced density matrices $\rho_1^M(t), \rho_2^M(t), ..., \rho_{N/M}^M(t)$ of the clusters, we will exploit the translation invariance of the lattice model and write $\rho_n^M(t) = \rho_m^M(t) \equiv \rho^M(t)$ for all $n, m \in \{1, 2, ..., N/M\}$. Thus we will be left with an equation of motion for the reduced state of one cluster $\rho^M(t)$ where we have dropped the cluster index for notational convenience. Similarly, we set $\mathcal{L}_n \to \mathcal{L}_0$ with $\mathcal{L}_0$ accounting for all local dynamics within a cluster. The resulting c-MoP equation, see Eq. (1.34), for the model of Eq. (2.1) reads

$$\begin{aligned}
&\dot{\rho}^M(t) = \mathcal{L}_0\rho^M(t) + iJ\left[\sigma_1\langle\sigma_M^\dagger\rangle(t) + \sigma_M\langle\sigma_1^\dagger\rangle(t) + \text{H.c.}\,, \rho^M(t)\right] \\
&- J^2\left\{\left[\sigma_1, \int_0^t dt' e^{\mathcal{L}_0(t-t')}\left(\delta\sigma_1^\dagger(t')\rho^M(t')d_M(t,t') - \rho^M(t')\delta\sigma_1^\dagger(t')s_M(t,t')\right)\right] + \text{H.c.}\right\} \\
&- J^2\left\{\left[\sigma_M, \int_0^t dt' e^{\mathcal{L}_0(t-t')}\left(\delta\sigma_M^\dagger(t')\rho^M(t')d_1(t,t') - \rho^M(t')\delta\sigma_M^\dagger(t')s_1(t,t')\right)\right] + \text{H.c.}\right\} \\
&- J^2\left\{\left[\sigma_1, \int_0^t dt' e^{\mathcal{L}_0(t-t')}\left(\delta\sigma_1(t')\rho^M(t')p_M(t,t') - \rho^M(t')\delta\sigma_1(t')h_M(t,t')\right)\right] + \text{H.c.}\right\} \\
&- J^2\left\{\left[\sigma_M, \int_0^t dt' e^{\mathcal{L}_0(t-t')}\left(\delta\sigma_M(t')\rho^M(t')p_1(t,t') - \rho^M(t')\delta\sigma_M(t')h_1(t,t')\right)\right] + \text{H.c.}\right\}
\end{aligned} \tag{2.4}$$

where, for any operator A, we have introduced the definitions $\langle A\rangle(t) = \text{Tr}\{A\rho^M(t)\}$ and $\delta A(t) = A - \langle A\rangle(t)$, while the correlation functions read

$$\begin{aligned}
d_{M(1)}(t,t') &= \text{Tr}\left\{\sigma_{M(1)}^\dagger e^{\mathcal{L}_0(t-t')}\left(\delta\sigma_{M(1)}(t')\rho^M(t')\right)\right\} \\
s_{M(1)}(t,t') &= \text{Tr}\left\{\sigma_{M(1)}^\dagger e^{\mathcal{L}_0(t-t')}\left(\rho^M(t')\delta\sigma_{M(1)}(t')\right)\right\} \\
p_{M(1)}(t,t') &= \text{Tr}\left\{\sigma_{M(1)}^\dagger e^{\mathcal{L}_0(t-t')}\left(\delta\sigma_{M(1)}^\dagger(t')\rho^M(t')\right)\right\} \\
h_{M(1)}(t,t') &= \text{Tr}\left\{\sigma_{M(1)}^\dagger e^{\mathcal{L}_0(t-t')}\left(\rho^M(t')\delta\sigma_{M(1)}^\dagger(t')\right)\right\}.
\end{aligned} \tag{2.5}$$

In contrast to Eq. (1.34) we have not used a compact form for the Born terms in Eq. (2.4) in order to illustrate the possible combinations of spin operators explicitly.

2.2.1 Unitary dynamics of closed systems

In a first example we consider a one-dimensional closed system version of Eq. (2.1) with $\omega_L = \Omega = \gamma = 0$ and periodic boundary conditions that is initially prepared in a pure state with one excitation in every second site and none otherwise, $|\psi_0\rangle = |\dots, 0, 1, 0, 1, \dots\rangle$ [54]. We are interested in the time-evolving state $|\psi(t)\rangle = e^{-iHt}|\psi(0)\rangle$ with $H = -J\sum_{j_n=1}^{N}\left(\sigma_{j_n}^\dagger\sigma_{j_{n+1}} + \sigma_{j_n}\sigma_{j_{n+1}}^\dagger\right)$.

As this model has an exact solution [58] in one dimension (due to the applicability of the Jordan-Wigner transfomation) for any number of lattice sites N, including the thermodynamic limit $N \to \infty$, we use it to test the accuracy of the c-MoP equation, see Eq. (1.29), for its explicit form for the model of Eq. (2.1). Thus, we will compare local observables resulting from the exact wave function $|\psi(t)\rangle$ with local observables obtained from the c-MoP density matrix $\rho^M(t)$.

For this particular case under study, the only remaining parameter is the tunneling rate J and the dynamics generated by the Liouvillian $\mathcal{L}_0$, see Eq. (2.2), is unitary. Therefore, it appears practical to rewrite Eq. (2.4) into a rotating frame with respect to $H_n = -J\sum_{j_n=1}^{M-1}\left(\sigma_{j_n}^{\dagger}\sigma_{j_{n+1}} + \sigma_{j_n}\sigma_{j_{n+1}}^{\dagger}\right)$, which leads to a c-MoP equation given by

$$\begin{aligned}
\dot{\rho}_I^M(t) =& - J^2\left\{\left[\sigma_1(t), \int_0^t dt'\sigma_1^{\dagger}(t')\rho_I^M(t')\tilde{d}_M(t,t') - \rho_I^M(t')\sigma_1^{\dagger}(t')\tilde{s}_M(t,t')\right] + \text{H.c.}\right\}\\
&- J^2\left\{\left[\sigma_M(t), \int_0^t dt'\sigma_M^{\dagger}(t')\rho_I^M(t')\tilde{d}_1(t,t') - \rho_I^M(t')\sigma_M^{\dagger}(t')\tilde{s}_1(t,t')\right] + \text{H.c.}\right\},
\end{aligned} \tag{2.6}$$

with the correlation functions

$$\begin{aligned}
\tilde{d}_{M(1)}(t,t') &= \text{Tr}\left\{\sigma_{M(1)}^{\dagger}(t)\,\sigma_{M(1)}(t')\rho_I^M(t')\right\}\\
\tilde{s}_{M(1)}(t,t') &= \text{Tr}\left\{\sigma_{M(1)}^{\dagger}(t)\,\rho_I^M(t')\sigma_{M(1)}(t')\right\},
\end{aligned} \tag{2.7}$$

and the interaction picture operators $\sigma_{1(M)}^{(\dagger)}(t) = e^{-iH_nt}\sigma_{1(M)}^{(\dagger)}e^{iH_nt}$ and $\rho_I^M(t) = e^{-iH_nt}\rho^M(t)e^{iH_nt}$.

We have neglected all terms of first order in the interaction, thus the mean-field term, and all counter-rotating terms in Eq. (2.6) as $\langle\sigma_{1(M)}\rangle(t) = p_{M(1)}(t,t') = h_{M(1)}(t,t') = 0$ for all times t. We have verified this statement numerically. However, the absence of these terms becomes clear in light of the invariance of the c-MoP equation (2.6) under the simultaneous transformation $\sigma \to e^{i\phi}\sigma$ with $\phi \in [0, 2\pi)$ of all spin operators present in the equation (this holds for the exact equation of motion (2.1) as well). This global $U(1)$ symmetry is preserved in the initial state $|\psi(0)\rangle\langle\psi(0)|$ and consequently in the dynamics as well. A mean-field calculation for clusters of m lattice sites will thus be identical to the result for an m-site open boundary lattice, and therefore be much less accurate, see Fig. 2.2 (*c*) and (*d*).

We have solved the c-MoP Eq. (2.6) by numerically integrating it in time using an Euler method [59]. Therefore, we have discretized time and solved from $t = 0$ to $t = T$ for time steps Δt. We needed to choose time steps of $\Delta t = 10^{-3}J^{-1}$ in order to avoid significant discretization errors. The main difficulty in solving the c-MoP equation arrises due to its integro-differential structure. The correlation functions in particular, see Eq. (2.7), force us to contract the interaction picture spin-matrix at time t with the complete history of the system for times $0 \leq t' \leq t$ in order to calculate e.g. $\sigma_M^{\dagger}(t')\rho^M(t')\text{Tr}\left\{\sigma_1^{\dagger}(t)\,\sigma_1(t')\rho^M(t')\right\}$. As a consequence, the number of matrix operations (including matrix multiplication and contraction for matrices of size $2^M \times 2^M$) required to step from $t \to t + \Delta t$ is given by $t/\Delta t$. Thus, the number of matrix operations needed for a simulation of the c-MoP equation up to $t = T$ scales quadratically in time as $\sum_{t_n=1}^{T/\Delta t} t_n \sim (T/\Delta t)^2/2$.

Moreover, the procedure requires to save both the interaction picture spin operators and more significantly the reduced state $\rho^M(t)$ for every instant of time in the main memory storage of the CPU. As a result the memory occupancy scales linearly

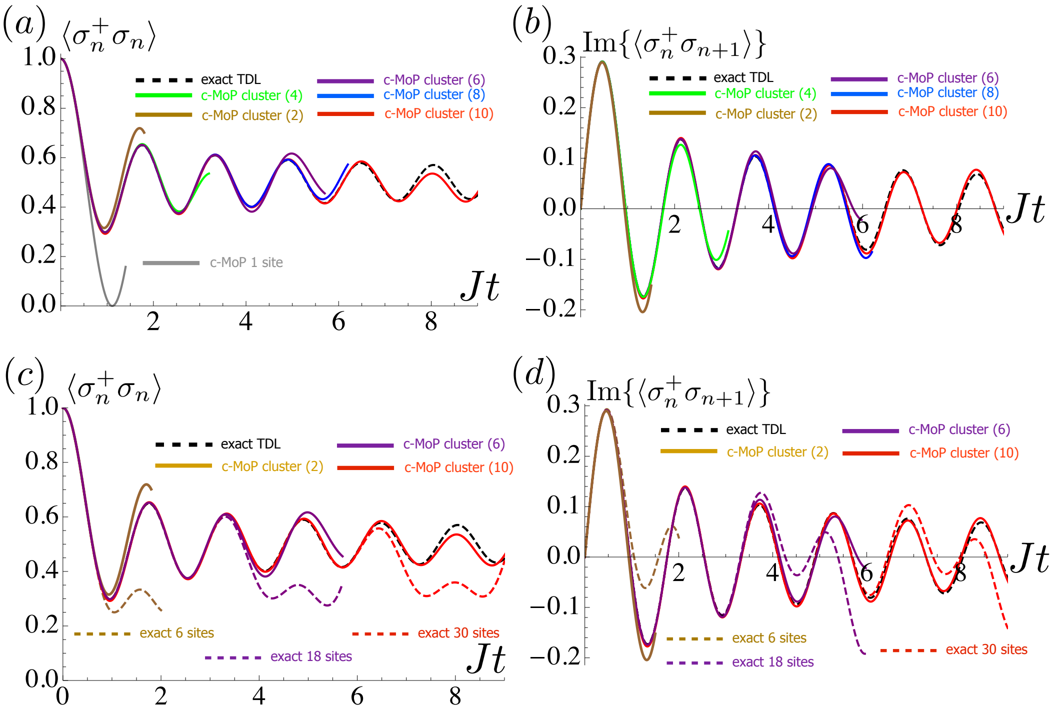

Figure 2.2: Application of the c-MoP approach to unitary dynamics of closed quantum many-body systems. We consider the unitary dynamics of a Heisenberg XX spin chain in one dimension for staggered initial conditions $|\psi_0\rangle = |\ldots,0,1,0,1,\ldots\rangle$ [54]. In part (a) and (c) we show the local occupation number $\langle\sigma_n^\dagger\sigma_n\rangle(t)$ of initially occupied cites, and in parts (b) and (d) we compare nearest neighbor correlations $\langle\sigma_n^\dagger\sigma_{n+1}\rangle(t)$ as a function of time Jt in units of the tunneling rate. The solid lines show c-MoP results for single-site c-MoP (gray), 2-site cluster c-MoP (brown), 4-site cluster c-MoP (green), 6-site cluster c-MoP (purple), 8-site cluster c-MoP (blue) and 10-site cluster c-MoP (red). The dashed lines show exact simulations of the full Liouville-von Neumann equation for periodic boundary conditions [58] in the thermodynamic limit (black), for $N = 6$ sites (brown), for $N = 18$ (purple) and for $N = 30$ sites (red). The real part of $\langle\sigma_n^\dagger\sigma_{n+1}\rangle(t)$ vanishes for all t.

in time. Whereas the spin operators are described by highly sparse matrices, the sparseness of the density matrix $\rho^M(t)$ decreases as the entanglement between the subsystems grows.

We show the result of the c-MoP approach for different cluster sizes with $M = 2, 4, 6, 8$ and 10 [60] in Fig. 2.2. In parts (a) and (c) we compare c-MoP to exact results for the local observable $\langle\sigma_n^\dagger\sigma_n\rangle(t)$ of initially occupied cites, and in parts (b) and (d) we compare nearest neighbor correlations $\langle\sigma_n^\dagger\sigma_{n+1}\rangle(t)$. For both quantities we observe that the accuracy of our approach is excellent for short times, but as expected eventually deteriorates for longer times from the exact result in the thermodynamic limit (TDL) of $N \to \infty$ as shown in Fig. 2.2 (a) and (b).

Remarkably the time range in which the approximation is highly accurate grows significantly as one applies the c-MoP approach to increasingly larger clusters. In Fig. 2.2 (c) and (d) we illustrate that the simulation of the c-MoP equations for an M-site cluster reaches time ranges which are even slightly larger than the ones obtained by the exact solution of the full Liouville-von Neumann equation for $N = 3M$ sites. Thus, the Born terms indeed contain a very significant amount of correlations and the system-size scaling of the c-MoP equation is much more favorable as compared to the system-size scaling of the Liouville-von Neumann equation.

With this example we stress the usefulness and efficiency of the c-MoP equations as the number of variables needed for a full cMoP simulation scales as 2^{2M} which is still feasible despite the computational difficulties arising due to the non-Markovian structure of the Born terms. The Liouville-von Neumann equation, in contrast, is an ordinary differential equation which is local in time but for an accuracy of local observables comparable to those of the c-MoP simulation one needs to solve for a much larger number of constituents. In the above example one would need to solve for at least $2^{2(3M)}$ variables. For the example of $M = 10$ the c-MoP equations contain $2^{20} \sim 10^6$ variables whereas the Liouville-von Neumann equation contains 2^{60} variables.

To further appreciate the perspective given by the cluster c-MoP approach one should also compare the time ranges that we are able to accurately describe here (although only for local quantities within a cluster) to those reached with t-DMRG approaches ($Jt \approx 6$) on high performance computing clusters [58]. What we present here are straight forward (brute force) integrations of Eq. (2.6) and the overall procedure for solving the c-MoP equations are the result of first steps which where taken to find the solutions rather than reach any optimization goals. In contrast, current DMRG achievements are the result of more than 20 years effort in optimizing the technique by a global community. Whereas it is clearly beyond the scope of this thesis, the purpose of which is to introduce the c-MoP approach, there can thus be little doubt that optimizations on the numerical integration of Eq. (2.6) will significantly increase the covered time range and widen the applicability of the c-MoP theory to quench problems beyond the Heisenberg XX spin chain [61]. Natural candidates are for example Bose Hubbard models [53, 54]. An obvious, very significant advantage of c-MoP, in particular in comparison with t-DMRG, is that it can be applied to two or three dimensional lattices using the same formalism and techniques presented here. We will elaborate on the higher dimensional case in more detail in Sec. 2.3.

Lastly, we would like to introduce a very simple c-MoP equation which is obtained by not taking a cluster of M sites as the subsystem of interest but rather a single lattice site. In this case the translation invariance of the subsystems as assumed generally in Eq. (2.4) and more specifically in Eq. (2.6) is broken due to the initial state. However, the translation invariance over the subgroup of two lattice sites still remains and we introduce the density matrix $\rho_A(t)$ which describes the reduced state of a single initially occupied site and $\rho_B(t)$ which describes the reduced state of an initially empty site. Most significantly, the free local evolution in this case turns out to be $\mathcal{L}_0 = 0$, see Eq. (2.2). As a consequence, the t-dependence in the Born terms of Eq. (2.6) vanishes, which allows us to rewrite the c-MoP equations into ordinary differential equations of second order. This step is achieved by taking the derivative of Eq. (2.6) with respect to time t, after which we arrive at the coupled c-MoP equations in their most simplified form

$$\begin{aligned}\ddot{\rho}_A(t) &= ZJ^2\langle\sigma^\dagger\sigma\rangle_B(t)\,\mathcal{D}_{\sigma^\dagger}[\rho_A(t)] + ZJ^2\langle\sigma\sigma^\dagger\rangle_B(t)\,\mathcal{D}_\sigma[\rho_A(t)]\\ \ddot{\rho}_B(t) &= ZJ^2\langle\sigma^\dagger\sigma\rangle_A(t)\,\mathcal{D}_{\sigma^\dagger}[\rho_B(t)] + ZJ^2\langle\sigma\sigma^\dagger\rangle_A(t)\,\mathcal{D}_\sigma[\rho_B(t)].\end{aligned} \tag{2.8}$$

Here, we have introduced the number of nearest neighbors or rather the coordination number Z, the expectation values $\langle G\rangle_{A(B)}(t) = \mathrm{Tr}_{A(B)}\{G\rho_{A(B)}(t)\}$ and the standard Lindblad superoperators $\mathcal{D}_G[\rho] = 2G\rho G^\dagger - G^\dagger G\rho - \rho G^\dagger G$ for an arbitrary operator G [5]. It is straight forward to solve Eq. (2.8) and we find $\langle\sigma^\dagger\sigma\rangle_A(t) = \cos^2(\sqrt{Z}Jt) = 1 - \langle\sigma^\dagger\sigma\rangle_B(t)$. We illustrate the result by the solid gray line in Fig. 2.2 (a) for $Z = 2$.

In addition, for $Z = 1$ we would like to mention that Eq. (2.8) corresponds to the c-MoP equations which describes the dynamics of two coherently coupled qubits with a Liouville-von Neumann equation given by $\dot{\rho} = iJ[\sigma_A^\dagger\sigma_B + \sigma_A\sigma_B^\dagger, \rho]$. Interestingly, for the initial condition $|1_A 0_B\rangle$ the exact result becomes identical to the c-MoP result for all local observables. Thus, we found an example where the self-consistent projection operator equations in Born approximation become exact even for a highly non-Markovian system and an arbitrarily large interaction rate J. We conclude from this simple example that the c-MoP theory clearly extends beyond the perturbative approaches of standard open system theory [4] as explained in Chapter 1.

2.2.2 Stationary states of driven-dissipative systems

We now focus on the physically very interesting scenario of steady states in driven-dissipative quantum many-body systems [23, 25, 26, 36, 52, 55–57] to further illustrate the power of the c-MoP approach. In fact, a very significant part of this thesis focuses rather on steady states of dissipative systems, see Section 2.3 and also Part II, than on unitary time evolution in closed systems. We thus consider the model of Eq. (2.1) with $\Omega \neq 0$, $\gamma \neq 0$ and $\Delta \neq 0$ which results in the c-MoP equation (2.4).

Instead of numerically integrating Eq. (2.4) in time up to a range where the steady state of the system is reached, we will now introduce a procedure which allows us to solve directly for the steady state by solving an algebraic equation rather than an integro-differential equation. Such a possibility is of crucial importance especially when considering the difficulties of a full time simulation as explained above in subsection 2.2.1.

For the validity of our procedure we need to assume that the dynamical map $e^{\mathcal{L}_0 t}$ fulfills the properties of a relaxing map [23]. A relaxing map satisfies $\lim_{t\to\infty} e^{\mathcal{L}_0 t}A = \mathrm{Tr}\{A\}\rho_0$ with $\mathcal{L}_0\rho_0 = 0$ for any matrix A. Most importantly for our purposes, we will exploit $\lim_{t\to\infty} e^{\mathcal{L}_0 t}\tilde{A} = 0$ for all traceless matrices $\tilde{A}$. By carefully examining Eq. (2.4) together with the correlation function in Eq. (2.5) we find for every dynamical map $e^{\mathcal{L}_0(t-t')}$ present in the equations to be acting on traceless matrices. And thus for $\tau = t - t' \to \infty$ the integral kernels vanish which we will explain in more detail in what follows.

For this purpose it is useful to consider a general superoperator picture [20, 23]. In this superspace we write the density operator $\rho^M(t)$ with M denoting the number of lattice sites in the cluster as a vector of dimension $2^{2M} \times 1$ rather than as a matrix of dimension $2^M \times 2^M$. The action of all remaining operators can then be written as super matrices of dimension $2^{2M} \times 2^{2M}$. For a detailed description of this idea see for example Ref. [62].

It can be shown [23] that the dynamical map $e^{\mathcal{L}_0 t}$ is relaxing if and only if the zero eigenvalue of the $2^{2M} \times 2^{2M}$ dimensional matrix $\mathcal{L}_0$ is non-degenerate and the rest of the eigenvalues have negative real part. We have confirmed this property numerically for all examples throughout this thesis. The mathematical conditions which guarantee for a dynamical map to be relaxing can be found in [63]. In short for our purposes, the mathematical theorem states that all dynamical maps defined on a finite dimensional Hilbert space which include non-zero local Markovian dissipators of Lindblad type for all modes or rather sites are relaxing maps.

Thus, in our approach we numerically diagonalize the $2^{2M} \times 2^{2M}$ matrix $\mathcal{L}_0$ and write $\mathcal{L}_0 = UDU^{-1}$ where U is the transformation matrix containing all eigenvectors of $\mathcal{L}_0$ and $D = \mathrm{diag}\{\lambda_0, \lambda_1, ..., \lambda_{2^{2M}}\}$ is the diagonal matrix containing all eigenvalues with $\lambda_0 = 0$ and $\mathrm{Re}\{\lambda_n\} < 0$ for all $n \in \{1, 2, ..., 2^{2M}\}$. As a consequence, we find an exponential decay of the memory kernel in Eq. (2.4) as the memory time $\tau = t - t'$ reaches further and further into the past history of the density matrix. Note, under the variable transformation $t' \to t - \tau$ the main changes for the Born terms in Eq. (2.4) are given by $\int_0^t dt' \to \int_0^t d\tau$, $\rho^M(t') \to \rho^M(t-\tau)$ and $e^{\mathcal{L}_0(t-t')} \to e^{\mathcal{L}_0\tau}$.

In order to rewrite the integro-differential c-MoP equations (2.4) into algebraic equations in the limit of $t \to \infty$ we take three steps. First, we write $\lim_{t\to\infty} \int_0^t d\tau = \int_0^\infty d\tau$. Second, we write $e^{\mathcal{L}_0\tau} = \sum_{l=0}^{2^{2M}} e^{\lambda_l \tau}\mathcal{M}_l$ with the matrices $\mathcal{M}_l = U\Pi_l U^{-1}$ and Π_l which is a projector in the l'th direction, that is, a matrix with zeros everywhere but in element (l,l) where it is one. Since all eigenvalues λ_l have negative real parts with the only exception of $\lambda_0 = 0$ we immediately find that $\lim_{\tau\to\infty} e^{\mathcal{L}_0\tau} = \mathcal{M}_0$. And as a consequence of $\lim_{\tau\to\infty} e^{\mathcal{L}_0\tau}A = \mathcal{M}_0 A = 0$ for all traceless matrices A, we can deduce $e^{\mathcal{L}_0\tau}A = \sum_{l=1}^{2^{2M}} e^{\lambda_l\tau}\mathcal{M}_l A$. We emphasize that this step allows us to integrate from $\tau = 0$ to $\tau = \infty$ over the superoperator $\sum_{l=1}^{2^{2M}} e^{\lambda_l\tau}\mathcal{M}_l$ in contrast to the full dynamical map $e^{\mathcal{L}_0\tau} = \sum_{l=0}^{d^2} e^{\lambda_l\tau}\mathcal{M}_l$ which would yield a divergence linear in time due to $\lim_{t\to\infty} \int_0^t d\tau \mathcal{M}_0 = \mathcal{M}_0 \lim_{t\to\infty} t$.

In the third step we approximate $\lim_{t\to\infty} \rho^M(t-\tau) \approx \lim_{t\to\infty} \rho^M(t) \equiv \rho^M_{ss}$ since the contributions of $\rho^M(t-\tau)$ to the integral kernel for large τ-values where $\tau \approx t$ are exponentially suppressed.

Exploiting these three steps we finally state the algebraic c-MoP equations for the steady state

$$
\begin{aligned}
\dot{\rho}_{ss}^{M} = 0 = {} & \mathcal{L}_0\rho_{ss}^{M} + iJ\left[\sigma_1\langle\sigma_M^\dagger\rangle_{ss} + \sigma_M\langle\sigma_1^\dagger\rangle_{ss} + \text{H.c.}\,, \rho_{ss}^{M}\right] \\
& - J^2\left\{\left[\sigma_1, \sum_{l,k=1}^{2^{2M}}\left(\frac{-1}{\lambda_l+\lambda_k}\right)\mathcal{M}_l\left(\delta\sigma_1^\dagger(ss)\,\rho_{ss}^{M} d_{M,k} - \rho_{ss}^{M}\delta\sigma_1^\dagger(ss)\,s_{M,k}\right)\right] + \text{H.c.}\right\} \\
& - J^2\left\{\left[\sigma_M, \sum_{l,k=1}^{2^{2M}}\left(\frac{-1}{\lambda_l+\lambda_k}\right)\mathcal{M}_l\left(\delta\sigma_M^\dagger(ss)\,\rho_{ss}^{M} d_{1,k} - \rho_{ss}^{M}\delta\sigma_M^\dagger(ss)\,s_{1,k}\right)\right] + \text{H.c.}\right\} \\
& - J^2\left\{\left[\sigma_1, \sum_{l,k=1}^{2^{2M}}\left(\frac{-1}{\lambda_l+\lambda_k}\right)\mathcal{M}_l\left(\delta\sigma_1(ss)\,\rho_{ss}^{M} p_{M,k} - \rho_{ss}^{M}\delta\sigma_1(ss)\,h_{M,k}\right)\right] + \text{H.c.}\right\} \\
& - J^2\left\{\left[\sigma_M, \sum_{l,k=1}^{2^{2M}}\left(\frac{-1}{\lambda_l+\lambda_k}\right)\mathcal{M}_l\left(\delta\sigma_M(ss)\,\rho_{ss}^{M} p_{1,k} - \rho_{ss}^{M}\delta\sigma_M(ss)\,h_{1,k}\right)\right] + \text{H.c.}\right\}
\end{aligned}
\tag{2.9}
$$

where, for any operator A, we have introduced the definitions $\langle A\rangle_{ss} = \text{Tr}\{A\rho_{ss}^{M}\}$ and $\delta A(ss) = A - \langle A\rangle_{ss}$, while the correlation functions read

$$
\begin{aligned}
d_{M(1),k} &= \text{Tr}\left\{\sigma_{M(1)}^\dagger\mathcal{M}_k\left(\delta\sigma_{M(1)}(ss)\rho_{ss}^{M}\right)\right\} \\
s_{M(1),k} &= \text{Tr}\left\{\sigma_{M(1)}^\dagger\mathcal{M}_k\left(\rho_{ss}^{M}\delta\sigma_{M(1)}(ss)\right)\right\} \\
p_{M(1),k} &= \text{Tr}\left\{\sigma_{M(1)}^\dagger\mathcal{M}_k\left(\delta\sigma_{M(1)}^\dagger(ss)\rho_{ss}^{M}\right)\right\} \\
h_{M(1),k} &= \text{Tr}\left\{\sigma_{M(1)}^\dagger\mathcal{M}_k\left(\rho_{ss}^{M}\delta\sigma_{M(1)}^\dagger(ss)\right)\right\}.
\end{aligned}
\tag{2.10}
$$

We have been able to solve equations (2.9) and (2.10) for cluster sizes of $M = 1, 2, ..., 6$. The numerical challenges reside in the full diagonalization of the $2^{2M} \times 2^{2M}$ dimensional matrix $\mathcal{L}_0$, in the nonlinear character of the Eq. (2.9) and most significantly in the large number of terms scaling as 2^{4M} due to the sum $\sum_{l,k=1}^{2^{2M}}$ in Eq. (2.9). The issues arising because of the nonlinearity of the steady state c-MoP equation can be overcome by solving it iteratively. In particular, we guess a test matrix for ρ_{ss}^{M} and insert it inside any of the trace operations in Eq. (2.9) and then solve the resulting linear equation for ρ_{ss}^{M}. Accordingly, the obtained solution is used for the guess in the next iteration process until convergences to some desired accuracy is reached.

We test the accuracy of Eq. (2.9) for different cluster sizes by comparing its predictions for local observables to t-DMRG integrations of the one-dimensional model in Eq. (2.1) with $N = 21$ lattice sites and open boundary conditions [56, 64]. From this t-DMRG numerics, which integrated Eq. (2.1) for a time range $T = 20/\gamma$ using a second order Trotter expansion with steps $\delta t = 10^{-3}/\gamma$, we extract the reduced density matrix for the central site $n_0 = 11$, denoted by ρ_{ss}^{DMRG}. For comparison

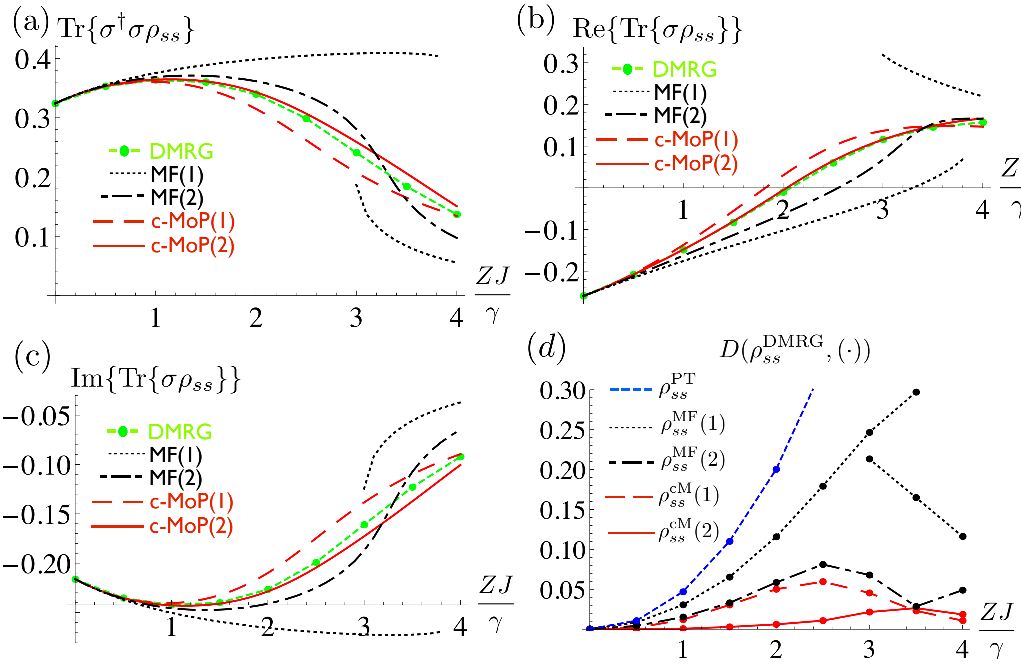

Figure 2.3: Accuracy test for stationary states of driven-dissipative quantum many-body systems. **(a)** On-site steady state occupation number $\mathrm{Tr}\{\sigma^\dagger\sigma\rho_{ss}\}$, **(b)** real part, and **(c)** imaginary part of $\mathrm{Tr}\{\sigma\rho_{ss}\}$ as a function of ZJ/γ. Here, $Z = 2$ denotes the coordination number of a one-dimensional lattice. Other parameters are $\Delta = 0.6\gamma$ and $\Omega = 1.5\gamma$. We plot results for t-DMRG (dashed green), single-site mean-field (dotted black), two-site cluster mean-field (dash-dotted black), single-site c-MoP (dashed red), and two-site cluster c-MoP (solid red). **(d)** Trace distances $D(\rho_{ss}^{\mathrm{DMRG}}, \rho_{ss}^{\mathrm{MF}}(1))$ (dotted black), $D(\rho_{ss}^{\mathrm{DMRG}}, \rho_{ss}^{\mathrm{MF}}(2))$ (dash-dotted black), $D(\rho_{ss}^{\mathrm{DMRG}}, \rho_{ss}^{\mathrm{cM}}(1))$ (dashed red), $D(\rho_{ss}^{\mathrm{DMRG}}, \rho_{ss}^{\mathrm{cM}}(2))$ (solid red), and $D(\rho_{ss}^{\mathrm{DMRG}}, \rho_{ss}^{\mathrm{PT}})$ (blue) for the same parameters as (a).

we also consider mean-field results, thus only terms up to first oder in Eq. (2.9), for different cluster sizes, and results of standard perturbation theory to second order in the interactions [65, 66] to show the significant quantitative and qualitative improvement of c-MoP over these approaches.

Therefore, we compare expectation values of on-site observables and calculate the trace distance $D(\rho_1, \rho_2) = \frac{1}{2}|\rho_1 - \rho_2|$ with $|A| = \sqrt{AA^\dagger}$ [67] between the t-DMRG result, $\rho_1 = \rho_{ss}^{\mathrm{DMRG}}$, and the approximations, $\rho_2 = \rho_{ss}^{\mathrm{cM}}(j)$, $\rho_{ss}^{\mathrm{MF}}(j)$ or ρ_{ss}^{PT} with the index $(j) = (1), (2), ..., (6)$ labeling the cluster size. Here, ρ_{ss}^{PT} denotes the result from standard perturbation theory to second order in the interactions [65, 66]

Figure 2.3(a) shows the occupation number $\mathrm{Tr}\{\sigma^\dagger\sigma\rho_{ss}\}$, whereas Figs. 2.3(b) and (c) show the real and imaginary parts of $\mathrm{Tr}\{\sigma\rho_{ss}\}$ for t-DMRG, c-MoP and mean-field calculations. We find a very good agreement between the c-MoP results (red) and t-DMRG results (green), which again improves significantly for two-site clusters (solid red lines) compared to individual lattice sites (dashed red lines). The mean-field results however deviate from the t-DMRG results to an extend which makes them unreliable over a large parameter range for both, single-site (black dotted) as well as two-site cluster (black dash-dotted) versions. These findings are further illustrated by Fig. 2.3 (d) which shows the trace distances $D(\rho_{ss}^{\mathrm{DMRG}}, \rho_{ss}^{\mathrm{MF}}(1))$ (dotted black), $D(\rho_{ss}^{\mathrm{DMRG}}, \rho_{ss}^{\mathrm{MF}}(2))$ (dash-dotted black), $D(\rho_{ss}^{\mathrm{DMRG}}, \rho_{ss}^{\mathrm{cM}}(1))$ (dashed red), $D(\rho_{ss}^{\mathrm{DMRG}}, \rho_{ss}^{\mathrm{cM}}(2))$ (solid red), and $D(\rho_{ss}^{\mathrm{DMRG}}, \rho_{ss}^{\mathrm{PT}})$. We see that whereas even $D(\rho_{ss}^{\mathrm{DMRG}}, \rho_{ss}^{\mathrm{cM}})$ is appreciably smaller than $D(\rho_{ss}^{\mathrm{DMRG}}, \rho_{ss}^{\text{MF-cl}})$, significantly smaller trace distances are achieved by two-site cluster c-MoP.

In the context of this section, all the density matrices describe reduced states of a single site, in case of a cluster calculation for $M \geq 2$ we trace out all sites from the cluster result but the site in the center of the cluster. The parameters in Fig. 2.3 are chosen in order to exemplify the bistability in the single-site meanfield solution [68]. The bistability vanishes for our example in the results of all approaches which are expected to be more precise than single-site mean-field. We will discuss the bistability and its physical meaning in more detail in Section 2.3.

As the c-MoP theory uses an expansion of the generalized Nakajima-Zwanzig equation, see Eq. (1.26), up to second order in the interactions between subsystems, one might wonder whether the same degree of approximation could be achieved with perturbation theory [65, 66]. To show that this is clearly not the case, we plotted for comparison $D(\rho_{ss}^{\mathrm{DMRG}}, \rho_{ss}^{\mathrm{PT}})$ for ρ_{ss}^{PT} as obtained from a perturbation theory approach up to order J^2 to the steady state, c.f. [65, 66], which is only accurate for $ZJ/\gamma \ll 1$.

In Fig. 2.4(a) we also show the result of the c-MoP cluster approach for larger cluster sizes with $M = 2, ..., 6$ by calculating again the trace distances with respect to the result obtained by t-DMRG. We find a fast convergences towards the t-DMRG result as the cluster size is increased, see also Fig 2.4(b), which is a precise control handle for verifying the reliability of the c-MoP result. To further appreciate the accuracy of the c-MoP approach we also show the trace distance of a 6-site cluster mean-field calculation to the t-DMRG result in Fig 2.4(a). Clearly, we find a much higher quantitative accuracy for the c-MoP approach than for the mean-field result. Moreover, given the finite integration range $[0, T]$, our t-DMRG results may still deviate slightly from the exact steady state and our c-MoP results could thus be even more accurate than suggested by Fig. 2.3 and Fig. 2.4. Here, our t-DMRG calculations required bond dimensions up to 400 which indicates that substantial correlations between subsystems are accurately taken into account by Eq. (2.9).

In addition to the remarkable quantitative accuracy of the c-MoP approach we find it to be very efficient. All the numerical c-MoP calculations where performed on standard desktop computers and the computation time for cluster sizes $M = 1, 2, 3$ was at the order of a few seconds, whereas the computation time for $M = 4(5)$ reached a few minutes (hours) and a day for $M = 6$. The full transient t-DMRG simulation required a computation time of several days. However, the t-DMRG

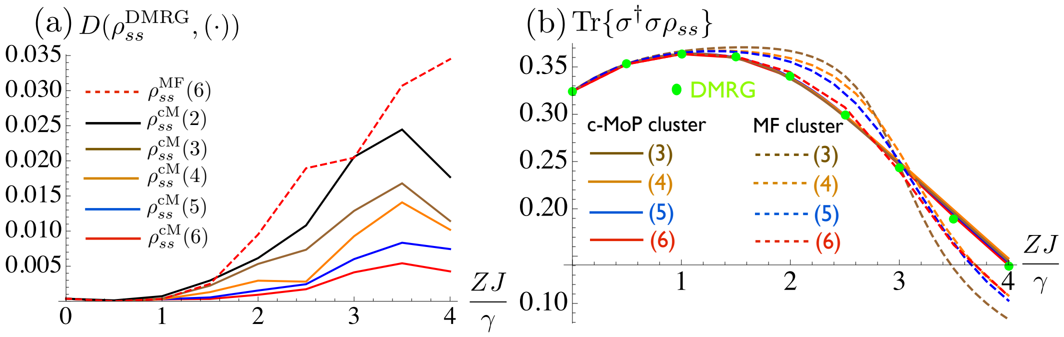

Figure 2.4: Accuracy test for stationary states of driven-dissipative quantum many-body systems. **(a)** Trace distances $D(\rho_{ss}^{\mathrm{DMRG}}, \rho_{ss}^{\mathrm{MF}}(6))$ (dashed red), $D(\rho_{ss}^{\mathrm{DMRG}}, \rho_{ss}^{\mathrm{cM}}(j))$ for $j = 2$ (solid black), $j = 3$ (solid brown), $j = 4$ (solid orange), $j = 5$ (solid blue), $j = 6$ (solid red) for the same parameters as in Fig. 2.3. **(b)** On-site steady state occupation number $\mathrm{Tr}\{\sigma^\dagger \sigma \rho_{ss}\}$ as a function of ZJ/γ for the same set of parameters as in Fig. 2.3. We plot results for t-DMRG (green points), cluster mean-field for cluster sizes of $M = 3$ (brown dashed), $M = 4$ (orange dashed), $M = 5$ (blue dashed), $M = 6$ (red dashed), and cluster c-MoP for cluster sizes of $M = 3$ (solid brown), $M = 4$ (solid orange), $M = 5$ (solid blue), $M = 6$ (solid red). The differences in the c-MoP curves are not easily visible as convergence has been reached for the whole parameter range.

method gives access to long-range correlation, whereas the c-MoP cluster method gives access to correlations of lengths below or equal to the cluster size.

In contrast to the closed system example of Sec. 2.2.1 we do not know of any exact analytic results that might give us an insight about the system in the TD limit $N \to \infty$. Nevertheless, we have performed a finite system size analysis using the t-DMRG method and thus calculated the results for $N = 18, 19, 20, 21$ lattice sites. The results for the local observables, which we are testing here, have converged and thus we expect the t-DMRG result to represent the behavior of the systems local observables in the TD limit. In the same spirit, one can also perform a finite system size analysis with both a mean-field approach and a c-MoP approach. In Fig. 2.4(b) we show the system-size scaling for the local on-site occupation number for a mean-field cluster approach (dashed lines) and a c-MoP cluster approach (solid lines) with the t-DMRG result (green points) for comparison. Clearly, the mean-field approach does not show any convergence as the cluster size is increased and thus using a mean-field approach can not give any insights about the system in the TD limit. In contrast, the c-MoP result shows a clear convergence, already for 3-site and 4-site clusters. Thus, the c-MoP approach is able to give a quasi exact picture for the steady state of this driven and dissipative many-body spin system in the TD limit.

2.2.3 Comparison of accuracy for stationary states of one- and two-dimensional lattices

To further elucidate the versatility of our approach, we here examine its accuracy for stationary states of two-dimensional lattices in comparison to one-dimensional chains. Figure 2.5 compares the solutions of a single-site c-MoP approach, a single-cite mean-field approach and a numerically exact approach for small lattices of one ($Z = 2$) and two ($Z = 4$) dimensions. Due to translational invariance the single-site c-MoP equations in the stationary state reduce from Eq. (2.4) and Eq. (2.5) to

$$\begin{aligned}\dot{\rho}_{ss} = 0 = &\mathcal{L}_1\rho_{ss} + i(ZJ)\left[\sigma\langle\sigma^\dagger\rangle_{ss} + \sigma^\dagger\langle\sigma\rangle_{ss}\,, \rho_{ss}\right]\\ &- \frac{(ZJ)^2}{Z}\left\{\left[\sigma, \int_0^\infty d\tau e^{\mathcal{L}_1\tau}\left(\delta\sigma^\dagger(ss)\rho_{ss}d(\tau) - \rho_{ss}\delta\sigma^\dagger(ss)s(\tau)\right)\right] + \text{H.c.}\right\}\\ &- \frac{(ZJ)^2}{Z}\left\{\left[\sigma, \int_0^\infty d\tau e^{\mathcal{L}_1\tau}\left(\delta\sigma(ss)\rho_{ss}p(\tau) - \rho_{ss}\delta\sigma(ss)h(\tau)\right)\right] + \text{H.c.}\right\}\end{aligned} \tag{2.11}$$

where we have dropped the lattice site index for the density matrix and the spin operators. Further, for any operator A, we have introduced the definitions $\langle A\rangle_{ss} = \text{Tr}\{A\rho_{ss}\}$ and $\delta A(ss) = A - \langle A\rangle_{ss}$, the single-site Liouvillian

$$\mathcal{L}_1(\cdot) = -i\left[\Delta\sigma^\dagger\sigma + \frac{\Omega}{2}(\sigma + \sigma^\dagger), (\cdot)\right] + \frac{\gamma}{2}\left(2\sigma(\cdot)\sigma^\dagger - \sigma^\dagger\sigma(\cdot) - (\cdot)\sigma^\dagger\sigma\right), \tag{2.12}$$

and the on-site correlation functions

$$\begin{aligned}d(\tau) &= \text{Tr}\left\{\sigma^\dagger e^{\mathcal{L}_1\tau}\left(\delta\sigma(ss)\rho_{ss}\right)\right\} \quad & s(\tau) &= \text{Tr}\left\{\sigma^\dagger e^{\mathcal{L}_1\tau}\left(\rho_{ss}\delta\sigma(ss)\right)\right\}\\ p(\tau) &= \text{Tr}\left\{\sigma^\dagger e^{\mathcal{L}_1\tau}\left(\delta\sigma^\dagger(ss)\rho_{ss}\right)\right\} \quad & h(\tau) &= \text{Tr}\left\{\sigma^\dagger e^{\mathcal{L}_1\tau}\left(\rho_{ss}\delta\sigma^\dagger(ss)\right)\right\}.\end{aligned} \tag{2.13}$$

Trace distances between mean-field approximations and exact solutions are plotted in the upper row of Fig. 2.5 whereas the lower row shows trace distances between c-MoP approximations and exact solutions.

Figures 2.5(a) and (c) show $D(\rho_{ss}^{\text{1D}}, \rho_{ss}^{\text{MF}})$ and $D(\rho_{ss}^{\text{1D}}, \rho_{ss}^{\text{cM}})$ respectively for $Z = 2$, $\Delta = 0.5\gamma$, and $N = 3$ with periodic boundary conditions as functions of ZJ/γ and Ω/γ. Figs. 2.5(b) and (d) in turn show $D(\rho_{ss}^{\text{2D}}, \rho_{ss}^{\text{MF}})$ and $D(\rho_{ss}^{\text{2D}}, \rho_{ss}^{\text{cM}})$ respectively for $Z = 4$, $\Delta = 0.5\gamma$, and $N = 5$ with periodic boundary conditions as functions of ZJ/γ and Ω/γ. The lattice sizes $N = 3$ in one dimension and $N = 5$ in two dimensions are chosen because these are the minimal lattice sizes where each lattice site has distinct left and right neighbors which close the lattice in periodic boundary conditions in each dimension. Nonetheless both lattices are small enough to allow for full numerical solutions for their stationary states. We are aware that a comparison with finite size lattices is not as convincing as the comparison with a full t-DMRG calculation but it suffices to give a picture of the tendency for two dimensional lattices. A more detailed presentation for a cluster c-MoP approach in two spatial dimensions is presented in Sec. 2.3.

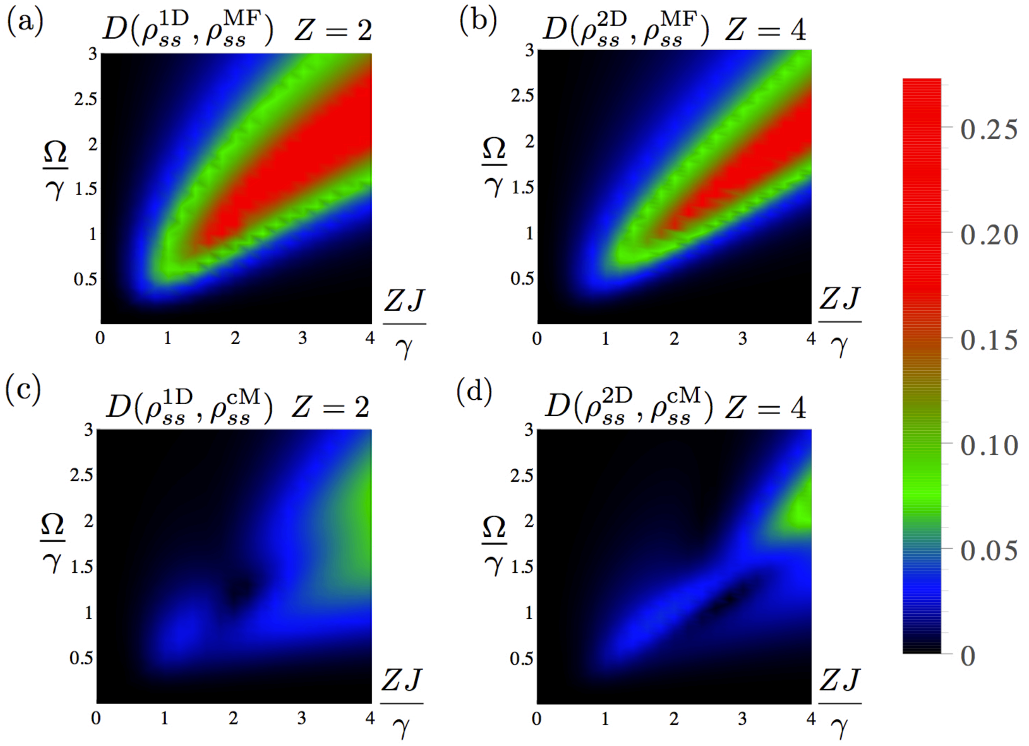

Figure 2.5: Performance of the method in terms of trace distances from exact solutions for small systems. (a) and (c): $D(\rho_{ss}^{1D}, \rho_{ss}^{MF})$ and $D(\rho_{ss}^{1D}, \rho_{ss}^{cM})$ respectively for $Z = 2$, $\Delta = 0.5\gamma$, and $N = 3$ with periodic boundary conditions as functions of ZJ/γ and Ω/γ. (b) and (d): $D(\rho_{ss}^{2D}, \rho_{ss}^{MF})$ and $D(\rho_{ss}^{2D}, \rho_{ss}^{cM})$ respectively for $Z = 4$, $\Delta = 0.5\gamma$, and $N = 5$ with periodic boundary conditions as functions of ZJ/γ and Ω/γ. In the bistable regions of the mean-field approximation we have chosen the branch which is closer to the exact solution.

We notice that there is no bistability for ρ_{ss}^{cM} in the whole parameter range. In the bistable regions of the mean-field approximation we have here chosen the branch which is closer to the exact solution. Further, we find a remarkable quantitative improvement of c-MoP over mean-field especially for regions where the on-site parameter Ω is comparable to the tunneling, i.e. $\Omega \approx ZJ$. For $\Omega \gg ZJ$ both approximations become very good as the dynamics is dominated by the on-site Liouvillian $\mathcal{L}_{\text{LT}}$. In the opposite case of $ZJ \gg \Omega$ the steady state of the lattice system is close to the vacuum state which is here a product state leading to high accuracy for both approximations. Finally, we find that both approaches become more accurate for a two dimensional lattice, see Fig. 2.5(b) and (d), where mean-field however still remains unsatisfactory.

2.3 The Quantum to classical transition in the driven and dissipative XX Spin model

So far we have mainly focused on the introduction of c-MoP theory into the field of quantum many-body physics. As a first step it was important to test the accuracy of the c-MoP predictions for cases where exact or quasi exact solutions can be found to allow for a quantitative comparison. In this section, however, we will aim for insights into the physics of non-equilibrium or rather driven-dissipative phase transition in many-body lattice problems.

Dissipative phase transition have been of interest for a long time, the most prominent examples include lasing [4], optomechanics [69], optical bistability [6, 11], optical parametric oscillators [20], see also Chapters 3 and 4, and the dissipative Dicke model [38], see also Chapter 5. The interest in dissipative phase transitions in the many-body context, in contrast, has emerged rather recently [24, 26, 37, 55, 56, 68]. In all of these approaches the steady state phase diagram has been obtained by a classical or a semi-classical mean-field Ansatz.

We will follow this guiding idea and present the mean-field phase diagram of the driven and dissipative XX spin model. Thus, we consider the model of Eq. (2.1) but allow for its generalization to hypercubic lattices of arbitrary dimension $d = 2Z$ with Z being the coordination number of the lattice. For simplicity we further choose $\Delta = 0$ throughout this section. Due to translational invariance, the master equation in mean-field approximation is given by Eq. (2.11) with the Born term neglected. Using the master equation, we find the mean-field equations to read

$$\partial_t \vec{v}(t) = A(\vec{v}(t))\vec{v}(t) + \vec{\gamma} \tag{2.14}$$

where

$$\vec{v}(t) = \begin{pmatrix} \langle\sigma_z\rangle(t) \\ \langle\sigma^\dagger\rangle(t) \\ \langle\sigma\rangle(t) \end{pmatrix}, \vec{\gamma} = \begin{pmatrix} -\gamma \\ 0 \\ 0 \end{pmatrix} \text{ and } A(\vec{v}(t)) = \begin{pmatrix} -\gamma & -i\Omega & i\Omega \\ -f^*(t) & -\frac{\gamma}{2} & 0 \\ -f(t) & 0 & -\frac{\gamma}{2} \end{pmatrix} \tag{2.15}$$

with the Pauli operator $\sigma_z = \sigma^\dagger\sigma - \sigma\sigma^\dagger$ and $f(t) = i(ZJ\langle\sigma\rangle(t) - \Omega/2)$. The steady state solution of Eq. (2.14) is then given by $\vec{v}_{ss} = -A(\vec{v}_{ss})^{-1}\vec{\gamma}$ which is a nonlinear algebraic equation typically appearing in nonlinear optics [6, 11, 42]. We proceed in the standard fashion [70]. First, we identify the physical steady state solutions by solving for $\vec{v}_{ss}$ in $\vec{v}_{ss} = -A(\vec{v}_{ss})^{-1}\vec{\gamma}$. Second, we perform a stability analysis in order to identify the stable solutions out of the possible set of physical solutions.

For the stability analysis we consider the vector $\vec{w}(t) = \vec{v}_{ss} + \delta\vec{v}(t)$ which describes small fluctuations around the stationary solution. We insert the Ansatz $\vec{w}(t)$ into Eq. (2.14) and linearize in the fluctuations which grants us with the linear stability matrix $L(\vec{v}_{ss})$ defined by

$\partial_t \delta\vec{v}(t) = L(\vec{v}_{ss})\delta\vec{v}(t)$ with

$$L(\vec{v}_{ss}) = \begin{pmatrix} -\gamma & -i\Omega & i\Omega \\ -f_{ss}^{*} & iZJ\langle\sigma_z\rangle_{ss} - \frac{\gamma}{2} & 0 \\ -f_{ss} & 0 & -iZJ\langle\sigma_z\rangle_{ss} - \frac{\gamma}{2} \end{pmatrix}. \tag{2.16}$$

It can be easily shown that there exist always three solutions for $\vec{v}_{ss}$ where for some regions of parameter space all three solutions are physical with one of which being unstable. The turning points or rather bifurcation points (BP) can then be found by solving for $\det L(\vec{v}_{ss}) = 0$ [11, 70]. In regions of the parameter space where the physical solution is unique, it is also always stable. We do not find any dynamical instabilities or rather Hopf bifurcation points since $\mathrm{Tr}\{L(\vec{v}_{ss})\} = -2\gamma < 0$ [11].

Note, that for $\Delta = 0$ there are only two free parameters in the mean-field equations, these are $(ZJ)/\gamma$ and Ω/γ. The number of total lattice sites N drops out. Moreover, the mean-field equations (2.14) lead to symmetric results for positive and negative tunneling rates J. This allows us to show the complete phase diagram of the resonantly driven and locally dissipative XX model in Fig. 2.6(a). We characterize three phases and a dissipative phase transition of first order exhibiting the typical bistable feature [71].

We refer to one of the phases as the classical phase since we find a unique stable solution where the spins behave classically in the sense that the $g^{(1)}$ function defined by $g^{(1)} = \langle\sigma^\dagger\sigma\rangle/|\langle\sigma\rangle|^2$ tends towards unity which is indicated in Fig. 2.6(b) by the red ($\langle\sigma^\dagger\sigma\rangle$ for $\Omega = 2\gamma$) and orange curve ($|\langle\sigma\rangle|^2$ for $\Omega = 2\gamma$), and by the black ($\langle\sigma^\dagger\sigma\rangle$ for $\Omega = 5\gamma$) and blue curve ($|\langle\sigma\rangle|^2$ for $\Omega = 5\gamma$). Thus, in the classical phase the spins behave as a bosonic field in a coherent state. In contrast to the classical phase, we find a phase with a unique stable solution but with $g^{(1)} \neq 1$ to which we refer as the quantum phase. In the shaded area we find three solutions with two of them being stable. We call this bistable phase the quantum+classical mixture, referring to the fact that we expect the full quantum solution to be a mixture of the upper (quantum) and lower (classical) stable branch. The three phases coexist in the triple point (TP) at $\Omega \approx 2\gamma$ and $ZJ \approx 2.75\gamma$. In order to further illustrate the behavior we show a cut through the phase diagram along the two white horizontal lines for $\Omega = 2\gamma$ and $\Omega = 5\gamma$ in Fig. 2.6(b). The solid lines in Fig. 2.6(b) indicate the stable branches while the dashed lines indicate the unstable branch for the observables of the corresponding color. The branches cross each other at the bifurcation points (PB) shown in Fig. 2.6(b) by the red rectangles.

2.3.1 Limit of infinite coordination

The mean-field ansatz finds a phase transition of 1st order as the local observables exhibit a discontinuous jump. The presented bistability is a common phenomenon in nonlinear optics. In all known cases which allow for an exact quantum mechanical

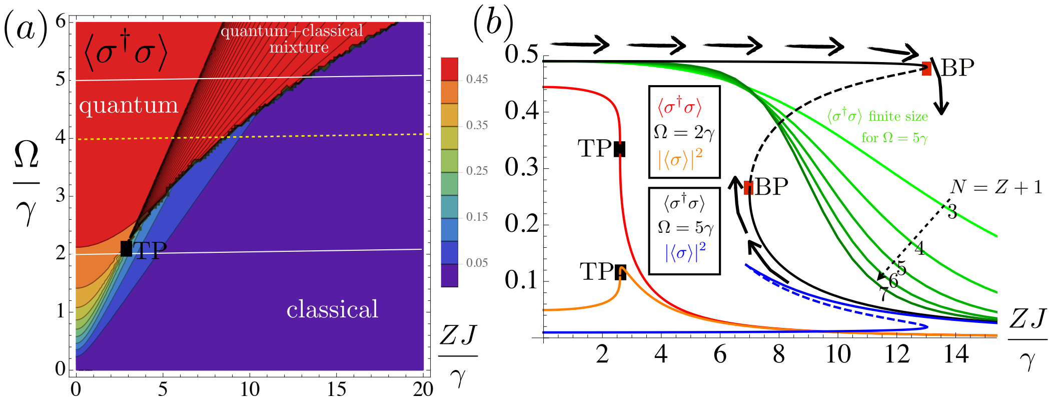

Figure 2.6: (a) Phase diagram of the resonantly driven and locally dissipative Heisenberg XX spin model. For a detailed discussion see the text. (b) Cut through the phase diagram for $\Omega = 2\gamma$ and $\Omega = 5\gamma$. We show $\langle\sigma^\dagger\sigma\rangle$ ($|\langle\sigma\rangle|^2$) as a function of ZJ/γ for $\Omega = 2\gamma$ in red (orange) color and for $\Omega = 5\gamma$ black (blue) color. The solid lines indicate stable branches while the dashed lines indicate unstable solution branches. The green solid lines show $\langle\sigma^\dagger\sigma\rangle$ as a function of ZJ/γ with $\Omega = 5\gamma$ for a finite system of $N = Z + 1 = 3, 4, \ldots 7$ sites for the infinite range model, see text for details.

treatment of the problem, however, the steady state is found to be unique [11, 72] in agreement with mathematical theorems [63, 73] which demand the uniqueness of the steady state for all finite dimensional Hilbert spaces. Thus, regarding the questions about the strict stationary state, the bistability found from a mean-field analysis has to be judged wrong. Nonetheless, a meaningful physical interpretation of the bistability relies on the concept of hysteresis. In the bistable phase both branches are meta-stable, quasi stationary or rather long lived. For adiabatic process steps moving from right to left (left to right) on the ZJ/γ axis in Fig. (2.6)(b) the system will follow the upper (lower) branch as indicated by the black arrows in Fig. 2.6(b). Moreover, the lifetime of the metastable branches scales with the system size. In this case, the system size parameter seems to be given by the coordination number Z and not by the number of sites N. It is in this sense in which the well-known statement about mean-field to become exact in infinite dimensions or infinite coordination has to be understood in the context investigated here.

At this point we believe, that the exact quantum steady state solution will never show a bistability and in the limit of infinite system size we will find a discontinuous jump between the stable branches occurring at some critical point. However, we have no strong tool at hand to proof our conclusion for the driven and dissipative XX model. Nonetheless, we will now present an argument which strongly substantiates our believe. Instead of considering the model of Eq. (2.1) with the nearest neighbor tunneling or rather coupling term, we will consider an infinite range coupling

$$\sum_{n=1}^{N}\sum_{\substack{m=1\\m\neq n}}^{N}\left(\sigma_n^\dagger\sigma_m+\sigma_n\sigma_m^\dagger\right)\quad\text{(infinite range model)}$$

such that tunneling processes can occur from each lattice site to any other site in the system. As a consequence, the coordination number Z and the total number of sites N relate according to $N = Z + 1$. The key point of our argument is that the mean-field equations for the nearest neighbor XX model and the infinite range model are equivalent. Thus, the phase diagram is identical for both models and we expect the mean-field predictions to become exact in the limit of infinite coordination in the sense we have understood above for both models. However, for the infinite range model it becomes evident that for any arbitrarily large but finite system size N or equivalently Z the total Hilbert space will be finite and therefore the steady state will be unique [63] according to the mathematical theorem. We show the local excitation number $\langle\sigma^\dagger\sigma\rangle$ for the infinite range model by the green solid lines in Fig. (2.6)(b) for increasing system size $N = 3, 4, 5, 6$ and $N = 7$. Indeed, we can see a clear tendency towards the mean-field solution.

In the infinite coordination number limit we find the c-MoP theory to converge towards mean-field theory. This can be immediately understood by a close inspection of Eq. (2.11). As the Born term scales as $(ZJ)^2/Z$ it will vanish for $Z \to \infty$ with ZJ fixed. The mean-field theory predicts the correct semi-classical behavior of the system but the full quantum behavior in the vicinity of the phase transition is illusive even to the c-MoP theory (in Born approximation). We consider this feature, also present in the variational approach of Ref. [74], a major drawback of the c-MoP theory as it is conducted here. The issue arrises as a direct consequence of the self-consistent Mori projector defined in Eq. (1.8) and in particular of the factorized state for $\rho_{\not{0}}(t)$, see Eq. (1.9). We will elaborate on this point in more detail in Chapter 5.

Phase transitions similar to the one presented here have also been reported in other works using mean-field theory. In Ref. [68] the transition occurs from a ”high” to a ”low” density phase whereas in Ref [74] the phases are called ”liquid” or ”gas” phases. Thus, our findings are not new with respect to known results but in contrast to these works the analogy to nonlinear optics has been made much clearer. Especially, the appearance of an unstable solution connecting the stable branches, the interpretation in terms of hysteresis and most importantly the identification of the system size parameter which is given by the coordination number Z allowed us to obtain a much better understanding of the physical picture. The apparent contradiction between the mathematical theorem demanding for a unique steady state and the bistability found by mean-field theory are now resolved.

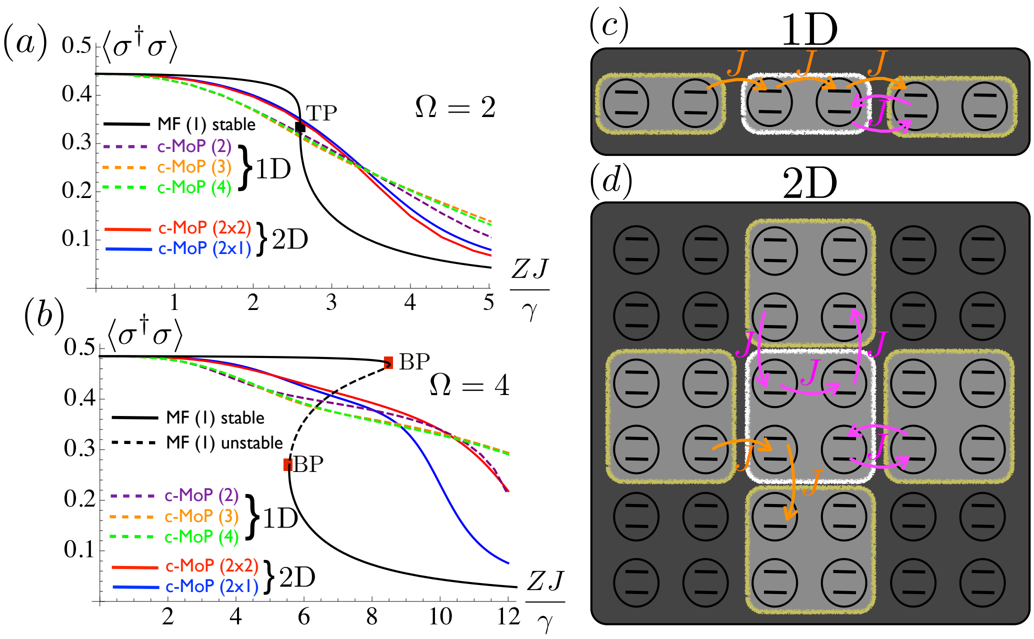

Figure 2.7: Cut through the phase diagram of the resonantly driven locally dissipative Heisenberg XX model for $\Omega = 2\gamma$ in (a) and $\Omega = 4\gamma$ in (b). We show $\langle\sigma^\dagger\sigma\rangle$ as a function of ZJ/γ.The black solid (dashed) lines indicate the result of the semi-classical mean-field analysis for the stable (unstable) branches with the triple point (TP) (bifurcation points (BP)) marked by the black (red) squares. The colored dashed lines show the result of clustered c-MoP approaches in 1D for a 2-site cluster (purple), 3-site cluster (orange), and a 4-site cluster (green). Finally, the colored solid lines show the result of clustered c-MoP approaches in 2D for a 2x1-cluster (blue) and a 2x2-cluster (red). Sketch the cluster c-MoP approach for a 1D ($Z = 2$) and a 2D ($Z = 4$) square lattice in (c) and (d), respectively. The tunneling processes indicated by the purple color are taken into account by the cluster c-MoP approach but the processes indicated by the orange color are neglected.

2.3.2 Absence of the phase transition in 1D and 2D

Mean-field theory has taught us about the role of the coordination number Z, yet, at the same time the total number of sites has been completely lost in the formalism. It is therefore a very interesting question whether a phase transition occurs as the number of sites tends towards the thermodynamic limit $N \to \infty$ with a fixed spatial dimension of the lattice. We will use the cluster c-MoP approach presented in Sec. 2.2.2 to answer this question in 1D and indicate how the question could be answered in 2D and possible even 3D using c-MoP theory.

We sketch the cluster c-MoP approach for a 1D ($Z = 2$) and a 2D ($Z = 4$) square lattice in Fig. 2.7(c) and (d), respectively. The tunneling processes indicated by the purple color in Fig. 2.7 are taken into account by the cluster c-MoP approach but the processes indicated by the orange color are neglected. In 1D these processes are of order $M + 1$ in the tunneling J for an M-site cluster but in 2D these corner processes are always second order in J. The absence of these processes occurs as a direct consequence of the self-consistent Mori projector defined in Eq. (1.8) and in particular of the factorized state for $\rho_{\not{\gamma}_0}(t)$, see Eq. (1.9). For a local c-MoP approach without clustering these corner processes scale with the coordination number as $Z(Z-1) \sim Z^2$ and the direct processes, indicated by the purple arrows in Fig. 2.7(c) and (d), scale as $\sim Z$. Hence, from such a combinatorial point of view the corner processes dominate for a non-clustered c-MoP Ansatz. However, as the cluster size increases the corner processes will become less in number relative to the direct processes, and thus less significant for large clusters in 2D or 3D. Nonetheless, since it is numerically very expensive to reach large cluster sizes in 2D and especially in 3D it is highly desirable to find a c-MoP theory which includes the corner processes. We will leave this task for future reasearch.

For now, we show a cut trough the mean-field phase diagram for $\Omega = 2$ in Fig. 2.7(a) and for $\Omega = 4$ in Fig 2.7(b). The black lines show the mean-field result for the on-site occupation $\langle \sigma^\dagger \sigma \rangle$ as a function of ZJ/γ. The dashed colored line show the c-MoP cluster results for different cluster sizes in 1D and the solid colored lines the cluster c-MoP results for a 2D lattice.

We expect from our results of Sec. 2.2.2 for the c-MoP results in 1D to reveal the behavior of the system in the thermodynamic limit $N \to \infty$ and we clearly find the absence of the phase transition. Thus, in 1D the number of sites does not trigger the phase transition. Even for $\Omega = 4$ in Fig. 2.7(b) where the tunneling rate reaches up to $J = 6\gamma$ the c-MoP results for an $M = 3$ site (orange dashed curve) and an $M = 4$ site (green dashed curve) cluster have converged such that there is almost no notable difference between the solutions. We emphasize, a mean-field analysis does not lead to a fast enough convergence with increased cluster size, similarly to what we show in Fig. 2.4(a), and a DMRG calculation would be much less efficient than the c-MoP approach.

Similarly, we find the absence of the phase transition in two spatial dimensions. Despite that the c-MoP results for a 2×1 (blue solid curve) and a 2×2 (red solid curve) cluster have not fully converged over the whole parameter range of Fig. 2.7(a) and (b), close to the phase transition points, however, the convergences seems to become apparent for $\Omega = 2$ in Fig. 2.7(a). We therefore conclude again for the absence of the phase transition in two spatial dimensions. A more solid statement can be obtained by performing a c-MoP calculation for a 3×2 or even a 3×3 cluster. These calculation are demanding but certainly within reach and shall be presented in future work, possibly together with a cluster c-MoP calculation for a 3D cubic lattice.

Summary of Part I

In the first half of Part I we have derived exact equations of motion for the reduced density matrices of subsystems embedded in quantum few or many-body system. The subparts of the system can have similar sizes and characteristic dynamical time scales, so that there is no clear distinction between system and environment. Thus, our theory generalizes the concept of open system theory by not relying on any time-scale separation between the constituents of interest.

At the heart of our theory lies the self-consistent Mori projector which accounts for the dynamical evolution of each subpart. The resulting exact equations can be expanded in powers of the interaction between the subparts resulting in coupled equations for each reduced density matrix of the subparts. The expansion up to first order is shown to be equivalent to mean-field theory. We further introduced all terms up to second order, which in contrast to mean-field theory, account for quantum correlations between the subparts.

In the second half of Part I we applied our method to spin lattices, both open and closed, to exemplify its applicability to quantum many-body systems. We show for various models that our equations provide a highly efficient and very accurate description of the dynamics of local quantities. Although only of the same computational complexity, our method yields a significant improvement of mean-field approaches and can also be straightforwardly extended to describe clusters of subsystems, as has been shown in 1D and to some extend in two dimensions. The accuracy of the approach improves very fast as the size of the clusters is increased and the convergence of the results with increasing cluster size is a control handle for verifying their reliability.

For unitary dynamics the c-MoP method is capable of covering time ranges comparable to those accessible with cutting edge t-DMRG calculations for small cluster sizes already. Whereas, for steady states in dissipative systems, where the c-MoP equations can be reduced to simple algebraic equations, we put up an efficient and yet very accurate technique for exploring phase diagrams of driven-dissipative systems.

As a direct application, we have shown on the example of the locally driven and dissipative Heisenberg XX spin model that a cluster c-MoP approach is able to reach the thermodynamic limit via a simple system-size scaling with increasing cluster size. The convergence is reached very fast as shown for a 1D lattice (to some extend also for a 2D lattice) and it therefore allows based on the findings from the c-MoP method to draw a conclusion on the behavior of the system in the $N \to \infty$ limit for a fixed spatial dimension. In both cases we find a strong signature for the absence of the nonequilibrium first order phase transition predicted by a single-site mean-field ansatz. Our investigations let us suggest that the phase transition is driven by the coordination number Z rather than by the number of lattice sites N.

Part II

The self-consistent projection operator theory for nonlinear quantum optical systems

Chapter 3

A case study on Degenerate Optical Parametric Oscillators

3.1 Introduction

Nonlinear optical systems play an important role in the field of optics both in classical [42, 75] and in quantum [6, 7, 76–78] regimes. Quantum mechanical effects, in particular, which are not explainable by classical optics, have triggered substantial research, especially in connection to modern applications such as high-precission measurements [79–82] and quantum information communication and processing [83, 84]. Importantly, the nonlinear nature of these systems leads to non-Gaussian states, which typically precludes an analytic treatment and therefore requires elaborate theoretical approaches [19, 20].

In a system where the dynamical degrees of freedom evolve on different time scales, approximate descriptions of reduced complexity may be found. For example, adiabatic elimination techniques can be exploited to derive effective equations of motion [5, 21]. In this chapter, we apply the self-consistent projection operator theory to the degenerate optical parametric oscillator. We exemplify in the present context how it generalizes adiabatic elimination approaches by taking dynamical back-action between the degrees of freedom into account, therefore reaching beyond the scope of time-scale separation. We expect the c-MoP method to be directly applicable to other nonlinear quantum optical models such as those for nondegenerate or multimode parametric oscillation [85–88], lasing [4, 6, 7, 89], optomechanical parametric oscillation [70, 90], or the dissipative Dicke model [38, 91, 92]. For the latter we will present results within the framework of this thesis in Chapter 5.

Degenerate optical parametric oscillators (DOPOs) have been extensively studied in the past [20, 76] and are one of the paradigm examples of a system subject to a driven and dissipative phase transition. It is formulated as a bosonic problem with two modes, signal and pump, subject to dissipation and interacting nonlinearly. In the adiabatic limit of a fast decaying pump mode, an effective master equation can be derived by means of standard projection operator approaches [20] and due to its reduced complexity, the steady state can be found by solving the corresponding Fokker-Planck equations for the positive P distribution [12, 93]. Yet away from the adiabatic limit one has to resort to numerical simulations or perturbative treatments [94–98]. Non-equilibrium many-body techniques such as the Keldysh formalism have also been employed to study steady-state properties [99–101]. While the application of all these techniques has allowed to deepen our understanding of DOPOs and phase transitions in driven dissipative quantum systems enormously, it is important to note that they are naturally built to determine the evolution of observables, making the determination of the quantum state of the optical fields very challenging, if not impossible.

The c-MoP approach, in contrast, derives a set of coupled equations for the reduced states of the two optical modes of the DOPO. By numerically solving these equations, we find the reduced density matrices of both the pump and the signal modes. We test the accuracy of our method by comparing its results with those of the full DOPO problem in regions of the parameter space where this is numerically tractable. Our findings show that our method is remarkably close to the exact results, both for steady states and dynamics, while being less numerically demanding than the full simulation of the DOPO problem. Not only that the accuracy of the c-MoP equations outperform linearization, mean-field and even Keldysh field theoretical approaches, they also give access to the entire reduced density matrix of the cavity modes in regions of the parameters that are inaccessible to full simulations of the DOPO master equation.

The possibly largest reduction of complexity in nonlinear quantum optical systems, however, comes from the application of Gaussian approximations on the state of the system. Within a Gaussian theory one can basically cover the whole parameter space efficiently to determine both steady-state and dynamical quantities such as two-time correlation functions. The simplest and most widely used Gaussian approach is known as the linearization technique [93, 102], which consists of assuming that the system configuration is, on average, in its classical state, but is constantly driven out of it by some "small" quantum fluctuations. While this technique provides a good qualitative picture of the physics in many, albeit not all, systems, it leads to unphysical predictions close to the critical points of the classical theory, e.g., to infinite photon numbers in the case of the DOPO [103]. These unphysical predictions can be regularized by applying a more elaborate Gaussian state approximation where the system is not forced to stay in its classical state, but chooses instead an average configuration more consistent with the quantum fluctuations that perturb it [104]. Motivated by such an idea, we apply a Gaussian approximation within the self-consistent projection operator theory, and show that it gives more accurate quantitative results than any of the usual Gaussian techniques, as it does not assume a Gaussian state for the entire system, but only for the reduced state of one of the modes.

The remainder of this Chapter is organized as follows. In Sec. 3.2 we introduce the DOPO model. We also discuss its symmetries and briefly elaborate on the standard linearization approach in Sec. 3.2.1. We briefly review the main concepts of the self-consistent projection operator theory in Sec. 3.3 and state the self-consistent Mori projector (c-MoP) equations, which lie at the center of our study. We exemplify on the DOPO problem that the c-MoP theory provides a systematic extension of mean-field approaches in Sec. 3.3.1 and reproduces known results in the adiabatic and the diabatic limits introduced in Sec. 3.3.3. An efficient procedure, different from the procedure exploited in Chapter 2, designed to deal with the non-Markovian structure of the c-MoP equations is provided in Sec. 3.3.2, which we use in Sec. 3.4 to test the accuracy of our method for steady-state quantities and to present quantum states of the signal mode. We also compare the performance of the c-MoP theory to the Keldysh formalism [99] in Sec. 3.5. A Gaussian state approximation on the c-MoP equations is performed in Sec. 3.6, which is shown to lead to highly accurate quantitative results as compared to previous linearization techniques. As a further test, we check in Sec. 3.7 that our method provides the same level of accuracy for the dynamics, as it does for steady states.

3.2 The degenerate optical parametric oscillator

A DOPO consists of a driven optical cavity containing a crystal with second-order optical nonlinearity, see Fig. 3.1. Two relevant resonances at frequencies ω_s (signal mode) and $\omega_p = 2\omega_s$ (pump mode) exist in the cavity, which are nonlinearly coupled via parametric down-conversion inside the crystal, capable of transforming a pump photon into a pair of signal photons, and vice versa. We assume that the external driving laser is resonant with the pump mode. Including damping through the partially transmitting mirrors at rates γ_p and γ_s for the pump and signal modes, respectively, the equation governing the evolution of the state ρ of the system in a picture rotating at the laser frequency is given by [20, 76]

$$\dot{\rho}(t) = \Big[\epsilon_p(a_p^\dagger - a_p) + \frac{\chi}{2}(a_p a_s^{\dagger\,2} - a_p^\dagger a_s^2)\,,\rho(t)\Big] + \gamma_p D_{a_p}\rho(t) + \gamma_s D_{a_s}\rho(t), \qquad (3.1)$$

where $\chi/2$ is the down-conversion rate and ϵ_p is proportional to square root of the injected laser's power. We have defined bosonic operators a_p and a_s for the pump and signal modes, respectively, which satisfy canonical commutation relations $[a_j, a_l^\dagger] = \delta_{jl}$ and $[a_j, a_l] = 0$. Further, we have defined the standard Lindblad superoperator $D_J(\cdot) = 2J(\cdot)J^\dagger - J^\dagger J(\cdot) - (\cdot)J^\dagger J$, with J being an arbitrary operator.

Note that the nonlinear interaction is third order in the field operators, precluding a general analytic solution of Eq. (3.1) to which we refer as the Liouville-von Neumann equation or simply the full master equation of the DOPO. The right hand side of Eq. (3.1) can also be written in a shorthand notation by introducing a superoperator $\mathcal{L}$ (Liouvillian), such that $\dot{\rho}(t) = \mathcal{L}\rho(t)$ which is the starting point of our theory as explained in Sec. 1.1.

3.2.1 Linearization approach and symmetry breaking

We will often be interested in the steady or rather stationary state $\rho_{ss} = \lim_{t\to\infty} \rho(t)$, which fulfills the equation $\mathcal{L}\rho_{ss} = 0$. Due to the dissipation acting on both modes and because an arbitrarily large but finite truncation will always provide an arbitrarily good approximation, we expect the steady state to be unique [23, 63] and the dynamical map $e^{\mathcal{L}t}$ to be relaxing, see also the explanations throughout Sec. 2.2.2.

We further note the invariance of the Liouvillian under a unitary transformation U_2 of Ising-type Z_2 which transforms a_s as $U_2 a_s U_2^\dagger = -a_s$. Since the steady state is unique, this implies that it has to be invariant under the Z_2 transformation too, i.e. $U_2 \rho_{ss} U_2^\dagger = \rho_{ss}$. This in turn leads to vanishing steady-state expectation values which include odd powers of the signal field operator a_s. In particular $\langle a_s\rangle = 0 = \langle a_p a_s^\dagger\rangle$, as for example $\langle a_s\rangle = \mathrm{Tr}\{a_s\rho_{ss}\} = \mathrm{Tr}\{U_2 a_s U_2^\dagger U_2 \rho_{ss} U_2^\dagger\} = -\langle a_s\rangle$. Overall, we emphasize that the full quantum solution for the steady state should not break the symmetry.

However, the most common technique used to analyze Eq. (3.1), known as the linearization approach, breaks this Z_2 symmetry [93, 102], which has to be restored "by hand" at the end of the calculation, following the procedure that we explain at the end of Sec. 3.4. In the linearization approach one first performs a unitary transformation with $U = U_s \otimes U_p$, where the displacement operator is given by $U_j \equiv e^{\alpha_j a_j^\dagger - \alpha_j^* a_j}$, on the Liouvillian $\mathcal{L}$ of Eq. (3.1). As a result of the transformation, the bosonic operators will be shifted according to $a_j \to \alpha_j + a_j$.

So far, however, it is not clear how to determine the mean amplitudes α_j. In fact, it is exactly at this point where different choices can be made leading to either the standard linearization approach, the self-consistent linearization approach presented in detail in Ref. [104], or a linearization approach within the c-MoP theory presented in Sec. 3.6.

In the standard linearization approach one calculates the field amplitudes by finding the Bloch equations for the expectation values $\langle a_j\rangle$ from the full DOPO master equation (3.1) and by additionally assuming a coherent state $|\alpha_p(t)\rangle\langle\alpha_p(t)|\otimes|\alpha_s(t)\rangle\langle\alpha_s(t)|$ for the full quantum state $\rho(t)$. Following these steps one obtains the nonlinear equations

$$\begin{aligned} \dot{\alpha}_p =& \epsilon_p - \gamma_p\alpha_p - \frac{\chi}{2}\alpha_s^2 \\ \dot{\alpha}_s =& -\gamma_s\alpha_s + \chi\alpha_p\alpha_s^*, \end{aligned} \tag{3.2}$$

which correspond to the classical equations of the system, as they can be obtained directly from Eq. (3.1) by assuming a coherent state for $\rho(t)$, or simply from Maxwell's equations. Depending on the injection parameter $\sigma = \chi\epsilon_p/\gamma_s\gamma_p$ one finds two types of steady-state solutions of Eq. (3.2) that is solutions with $\dot{\alpha}_s = \dot{\alpha}_p = 0$. One of them has $\alpha_s = 0$ and $\alpha_p = \epsilon_p/\gamma_p$, and hence it does not break the symmetry; it is known as the below-threshold solution, and is only stable for $\sigma < 1$. The other solution is bistable and has $\chi\alpha_s = \pm\sqrt{2(\chi\epsilon_p - \gamma_s\gamma_p)}$ and $\chi\alpha_p = \gamma_s$, hence breaking the Z_2 symmetry; it is known as the above-threshold solution, and exists only for $\sigma > 1$. The threshold point $\sigma = 1$ marks a critical point where the classical theory predicts a phase transition from a signal-off phase with $\alpha_s = 0$ to a signal-on phase with $\alpha_s \neq 0$. In the signal-off phase all injected power ϵ_p goes into the pump mode, while after crossing the critical point all the extra injection is transferred to the signal mode, see the gray thin solid line in Fig. 3.2.

Once the classical solutions have been identified, the second approximation consists in coming back to the original master equation with the bosonic operators written in the shifted basis as $a_j \to \alpha_j + a_j$, and neglecting any term which goes beyond quadratic order in the fluctuation operators a_j, in particular the term $\frac{\chi}{2}(a_p^\dagger a_s^2 - a_p a_s^{\dagger 2})$. This leads to the so-called linearized master equation

$$\dot{\rho}(t) = \left[\frac{\chi}{2}(\alpha_p a_s^{\dagger 2} - \alpha_p^* a_s^2) + \chi(\alpha_s^* a_s^\dagger a_p - \alpha_s a_s a_p^\dagger)\,, \rho(t)\right] + \gamma_p D_{a_p}\rho(t) + \gamma_s D_{a_s}\rho(t) \tag{3.3}$$

which can be easily solved. The state $\rho(t)$ resulting from Eq. (3.3) describes the Gaussian fluctuations around the classical state. Note that all linear terms in the field operators have been cancelled in Eq. (3.3) due to the choices made for the mean amplitudes α_j. Thus, it is also possible to obtain Eqs. (3.2) and (3.3) by transforming $a_j \to \alpha_j + a_j$ in the full master equation (3.1) and by further choosing α_j such that all linear terms in the transformed master equation vanish.

One has to keep in mind that this linearized theory can only be trustworthy when the classical solution is a strong attractor, because only then the quantum fluctuations driving the system out of equilibrium are strongly damped, and quantum noise can be treated as a small perturbation. This means that, in particular, any predictions obtained through this method cannot be trusted in the vicinities of critical points of the classical theory: points of the parameter space where one solution becomes unstable, making way for a new solution to kick in, hence creating non-analytic behaviour in some observable, that is, a classical phase transition. Indeed, this is exactly the case for the DOPO, in which this linearized description breaks down at threshold, offering unphysical predictions such as infinite photon numbers in the signal field (as illustrated by the gray thin line in Fig. 3.5).

3.3 Self-consistent Mori Projector Approach to the DOPO problem

We will now apply the self-consistent Mori projector approach to the DOPO based on the main steps and results shown in Chapter 1 of this work. In the course of this section, we will recall the general concept of our theory and also introduce the model specific steps for the DOPO. In the first step, we divide the entire system into subsystems. In the DOPO this naturally amounts to consider the pump mode described by its reduced state $\rho_p(t) \equiv \mathrm{Tr}_s\{\rho(t)\}$ and the signal mode described by $\rho_s(t) \equiv \mathrm{Tr}_p\{\rho(t)\}$ as the subsystems of interest. In order to obtain a closed set we

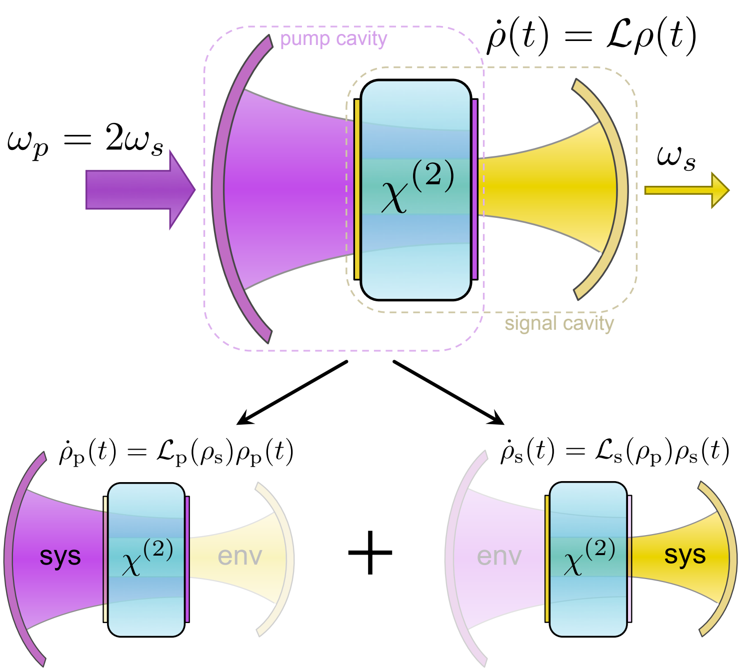

Figure 3.1: Sketch of the self-consistent projection operator theory for the DOPO [105, 130]. In the c-MoP approach, the full problem described by the state $\rho(t)$ and the Liouvillian $\mathcal{L}$ is mapped onto two coupled equations for the signal and pump modes. In one of the equations, the signal mode considered as the system is described by an effective master equation for its reduced state $\dot\rho_s(t) = \mathcal{L}_s(\rho_p)\rho_s(t)$ with an effective Liouvillian depending on the state of the pump, which plays here the role of an environment. The other equation considers the reversed scenario with the pump taking the role of the system while the signal is interpreted as the environment, leading to the effective equation $\dot\rho_p(t) = \mathcal{L}_p(\rho_s)\rho_p(t)$. In this way the two equations form a closed set.

also revers the scenario where we treat the pump mode as the system of interest, see Fig. 3.1 for an illustration.

In the next main step of the c-MoP theory, we split the full Liouvillian $\mathcal{L}$ from Eq. (3.1) into three parts. After performing a displacement $a_p \to a_p + \tilde\alpha_p$, where $\tilde\alpha_p$ will be chosen later, see Sec. 3.3.1, we write $\mathcal{L} = \mathcal{L}_p + \mathcal{L}_s + \mathcal{L}_I$, with

$$\begin{aligned}
\mathcal{L}_p(\cdot) &= \left[a_p^\dagger(\epsilon_p - \gamma_p\tilde\alpha_p) - a_p(\epsilon_p - \gamma_p\tilde\alpha_p^*)\,,\,(\cdot)\,\right] + \gamma_p D_{a_p}(\cdot),\\
\mathcal{L}_s(\cdot) &= \frac{\chi}{2}\left[\tilde\alpha_p a_s^{\dagger 2} - \tilde\alpha_p^* a_s^2\,,\,(\cdot)\,\right] + \gamma_s D_{a_s}(\cdot),\\
\mathcal{L}_I(\cdot) &= \frac{\chi}{2}\left[a_p a_s^{\dagger 2} - a_p^\dagger a_s^2\,,\,(\cdot)\,\right].
\end{aligned} \tag{3.4}$$

The displacement $a_p \to a_p + \tilde\alpha_p$ moves the large coherent background of the pump field into the free evolution of the signal $\mathcal{L}_s$, keeping only the pump mode's fluctuations within the nonlinear signal-pump interaction $\mathcal{L}_I$. Such a step is important as our theory expands in powers of the interaction Liouvillian $\mathcal{L}_I$ in order to solve the Nakajima-Zwanzig equation as shown Sec. 1.5. Throughout the thesis we will expand to second order in the system-environment interaction. This approximation is known as the Born approximation [4]. Note that in the context of continuous variable systems a transformation of type $a \to \alpha + a$ is well-defined by the unitary displacement operator in contrast to the spin physics in Chapter 2.

The effective equations of the signal and the pump mode can be directly deduced from Eq. (1.34) if one sets $\vec{A} = (\chi/2)\{a_s^2, a_s^{\dagger\,2}\}$ and $\vec{B} = \{a_p^\dagger, a_p\}$ in Eq. (1.31). The c-MoP equation of the DOPO read,

$$\begin{aligned}\dot{\rho}_s(t) = {} & \mathcal{L}_s\rho_s(t) + \frac{\chi}{2}\left[a_s^{\dagger 2}\langle a_p\rangle(t) - a_s^2\langle a_p\rangle^{*}(t), \rho_s(t)\right] \\ & + \left(\frac{\chi}{2}\right)^2\left\{\left[a_s^2\,, \int_0^t dt' e^{\mathcal{L}_s(t-t')}\mathcal{K}_s(t,t')\rho_s(t')\right] + \text{H.c.}\right\},\end{aligned} \tag{3.5}$$

$$\begin{aligned}\dot{\rho}_p(t) = {} & \mathcal{L}_p\rho_p(t) + \frac{\chi}{2}\left[a_p\langle a_s^2\rangle^{*}(t) - a_p^\dagger\langle a_s^2\rangle(t)\,, \rho_p(t)\right] \\ & + \left(\frac{\chi}{2}\right)^2\left\{\left[a_p\,, \int_0^t dt' e^{\mathcal{L}_p(t-t')}\mathcal{K}_p(t,t')\rho_p(t')\right] + \text{H.c.}\right\},\end{aligned} \tag{3.6}$$

where we have defined the Kernel superoperators

$$\begin{aligned}\mathcal{K}_s(t,t')(\cdot) = {} & \delta a_s^2(t')(\cdot)\, d_p^+(t,t') - (\cdot)\delta a_s^2(t')\, \tilde{d}_p^+(t,t') \\ & - \delta a_s^{\dagger 2}(t')(\cdot)\, d_p^-(t,t') + (\cdot)\delta a_s^{\dagger 2}(t')\, \tilde{d}_p^-(t,t'),\end{aligned} \tag{3.7}$$

$$\begin{aligned}\mathcal{K}_p(t,t')(\cdot) = {} & \delta a_p(t')(\cdot)\, d_s^+(t,t') - (\cdot)\delta a_p(t')\, \tilde{d}_s^+(t,t') \\ & - \delta a_p^\dagger(t')(\cdot)\, d_s^-(t,t') + (\cdot)\delta a_p^\dagger(t')\, \tilde{d}_s^-(t,t'),\end{aligned} \tag{3.8}$$

and for any operator A_j acting on the signal ($j = s$) or pump ($j = p$) subspace, we have defined the corresponding fluctuation operator $\delta A_j(t) \equiv A_j - \text{Tr}_j\{A_j\, \rho_j(t)\}$.

The state of the pump mode $\rho_p(t)$ enters the signal mode's dynamics, eq. (3.5), via $\langle a_p\rangle(t) \equiv \text{Tr}_p\{a_p\rho_p(t)\}$ and the correlation functions

$$\begin{aligned} d_p^+(t,t') &= \text{Tr}_p\{a_p^\dagger e^{\mathcal{L}_p(t-t')}\delta a_p^\dagger(t')\rho_p(t')\}, \\ \tilde{d}_p^+(t,t') &= \text{Tr}_p\{a_p^\dagger e^{\mathcal{L}_p(t-t')}\rho_p(t')\delta a_p^\dagger(t')\}, \\ d_p^-(t,t') &= \text{Tr}_p\{a_p^\dagger e^{\mathcal{L}_p(t-t')}\delta a_p(t')\rho_p(t')\}, \\ \tilde{d}_p^-(t,t') &= \text{Tr}_p\{a_p^\dagger e^{\mathcal{L}_p(t-t')}\rho_p(t')\delta a_p(t')\}.\end{aligned} \tag{3.9}$$

In turn, the state of the signal mode $\rho_s(t)$ enters the pump mode's dynamics, eq. (3.6), via the expectation value $\langle a_s^2\rangle(t) \equiv \text{Tr}_s\{a_s^2\rho_s(t)\}$ and the correlation functions

$$\begin{aligned} d_s^+(t,t') &= \text{Tr}_s\{a_s^{\dagger\,2} e^{\mathcal{L}_s(t-t')}\delta a_s^{\dagger\,2}(t')\rho_s(t')\}, \\ \tilde{d}_s^+(t,t') &= \text{Tr}_s\{a_s^{\dagger\,2} e^{\mathcal{L}_s(t-t')}\rho_s(t')\delta a_s^{\dagger\,2}(t')\}, \\ d_s^-(t,t') &= \text{Tr}_s\{a_s^{\dagger\,2} e^{\mathcal{L}_s(t-t')}\delta a_s^2(t')\rho_s(t')\}, \\ \tilde{d}_s^-(t,t') &= \text{Tr}_s\{a_s^{\dagger\,2} e^{\mathcal{L}_s(t-t')}\rho_s(t')\delta a_s^2(t')\}.\end{aligned} \tag{3.10}$$

Equations (3.5) and (3.6) should be understood as two coupled equations which represent effective equations for the reduced states of the signal and the pump mode. They can be thought of as non-Markovian and nonlinear master equations which do not rely on any time-scale separation between the modes. We will elaborate in detail on the limits where time-scale separation is present in Sec. 3.3.3.

The only assumptions made so far are the Born approximation and the assumption of an initially factorized state $\rho(0) = \rho_p(0) \otimes \rho_s(0)$. The latter seems very reasonable by considering the vacuum as the state of the two modes before the driving laser is switched on. We also emphasize, our approach does not ignore system-environment or rather signal-pump correlations as shown in Chapter 1. Indeed, we will show the crucial importance of the Born term in several examples below. Of course, c-MoP theory or any theory based on the concept of projection operators does not give access to explicit expressions for system-environment correlation functions. An example in this context could be the cross-correlation function $\langle a_p^\dagger a_s\rangle - \langle a_p^\dagger\rangle\langle a_s\rangle$.

The most striking advantage of projection operator theories and in particular of the c-MoP theory is the reduction of the complexity of the problem. In the example of the DOPO the complexity of the Liouville-von Neumann eq. (3.1) scales as $\dim \mathcal{H}_s \times \dim \mathcal{H}_p$, where $\mathcal{H}_{s/p}$ denotes the Hilbert space of the signal/pump modes, while the complexity of the c-MoP equations scale as $\dim \mathcal{H}_s + \dim \mathcal{H}_p$. The self-consistent Mori-projector theory thus offers a very significant reduction of complexity.

3.3.1 Mean-field Approximation for the DOPO

A merely approximate but very simple way of solving the c-MoP equations is to consider all terms up to first order in the interaction $\mathcal{L}_I$ only. Hence we drop all terms proportional to χ^2 from eqs. (3.5) and (3.6). It can be easily understood that within this approximation it does not make a difference whether the pump field is displaced or not. For simplicity we put the displacement $\tilde{\alpha}_p$ from eq. (3.4) to zero and obtain two coupled equations

$$\begin{aligned} \dot{\rho}_p(t) &= \Big[(\epsilon_p - \frac{\chi}{2}\langle a_s^2\rangle^*)\, a_p^\dagger - \text{H.c.}\,, \rho_p(t)\Big] + \gamma_p D_{a_p}\rho_p(t), \\ \dot{\rho}_s(t) &= \frac{\chi}{2}\,\Big[\langle a_p\rangle a_s^{\dagger\,2} - \text{H.c.}\,, \rho_s(t)\Big] + \gamma_s D_{a_s}\rho_s(t), \end{aligned} \tag{3.11}$$

known as mean-field equations [39]. These equations are quadratic in the field operators and therefore it is straightforward to solve them either numerically for the dynamics or analytically for the fixed points [39, 104]. The stationary state of the signal mode will be a Gaussian state [83, 84, 106] centered around a vanishing field amplitude $\langle a_s\rangle = 0$ as the mean-field equations do not break the Ising-type Z_2 symmetry. The steady state of the pump mode will be a coherent state with an amplitude given by $\langle a_p\rangle_{ss}^{MF} = (\epsilon_p - \frac{\chi}{2}\langle a_s^2\rangle_{ss}^{MF})/\gamma_p$.

Just like the c-MoP equations (3.5) and (3.6), the mean-field equations are coupled nonlinear equations which have to be solved self-consistently. Within mean-field theory fluctuations of the pump mode are disregarded. Fluctuations of the signal mode, however, are (at least to some extend) taken into account [39, 104]. This leads to the regularization of the divergences appearing in the classical theory or rather the standard linearization approach. For our purposes it is important to note that the pump field amplitude always stays below the classical above-threshold solution, i.e. $\langle a_p \rangle_{ss}^{MF} < \gamma_s/\chi$. Thus, we use it as the displacement in eq. (3.4), i.e. $\tilde{\alpha}_p = \langle a_p \rangle_{ss}^{MF}$. This will guarantee a well-behaved Liouvillian for the free system $\mathcal{L}_s$ as we will explain in more detail in Sec. 3.3.2.

The mean-field equations can also be found by putting the factorized state Ansatz $\rho(t) = \rho_p(t) \otimes \rho_s(t)$ into the Liouville-von Neumann equation, here given by eq. (3.1), before tracing out each of the modes separately. This well-known procedure, indeed, neglects all signal-pump correlations. Within the self-consistent projection operator theory, mean-field can be understood as an approximation to linear order in the interaction $\mathcal{L}_I$ for the dynamics of reduced density matrices. Our theory therefore provides a systematic generalization of mean-field approaches. It is due to the Born terms, which are second order in $\mathcal{L}_I$, that signal-pump correlations are taken into account. Therefore, we expect a higher quality of approximation by going from first order to second order in the interaction.

3.3.2 From integro-differential to ordinary differential equations

In order to solve the full c-MoP equations including the Born terms we will need to overcome two main difficulties. While the c-MoP equation (3.6) of the pump mode is quadratic in the field operators, granting us with a closed set of equations including only first and second moments of the pump field, the c-MoP equation (3.5) of the signal mode is quartic in the field operators. We will therefore either solve the latter fully numerically, see Sec. 3.4, or apply a Gaussian state approximation as presented in Sec. 3.6. In any of these two approaches, we need to overcome the second difficulty which arrises due to the non-Markovian structure of our theory. In the remainder of this section we will thus show how to rewrite the integro-differential c-MoP equations (3.5) and (3.6) into a set of coupled ordinary differential equations. For the present problem this step is crucial, as solving the integro-differential equations is significantly more demanding for both numerical and analytical approaches.

We start by evaluating the correlation functions of the pump. By taking derivatives of the pump correlators $d_p^{\pm}(t,t')$ and $\tilde{d}_p^{\pm}(t,t')$ with respect to t, see eqs. (3.9), considering initial conditions at $t = t'$ (note that we understand from the c-MoP equations that $t' \leq t$), and exploiting the fact that the operator $\delta a_p^{\dagger}(t')\rho_p(t')$ is traceless, we find

$$\begin{aligned} d_p^{+}(t,t') &= \tilde{d}_p^{+}(t,t') = [\langle a_p^{\dagger 2} \rangle(t') - \langle a_p \rangle^{*2}(t')] e^{-\gamma_p(t-t')}, \\ \tilde{d}_p^{-}(t,t') &= [1 + \langle a_p^{\dagger} a_p \rangle(t') - |\langle a_p \rangle(t')|^2] e^{-\gamma_p(t-t')}, \\ d_p^{-}(t,t') &= [\langle a_p^{\dagger} a_p \rangle(t') - |\langle a_p \rangle(t')|^2] e^{-\gamma_p(t-t')}. \end{aligned} \tag{3.12}$$

Hence, all correlation functions of the pump can be written in a form where the t dependence only enters in a simple exponential factor.

A bit more effort is needed in order to simplify the correlation functions of the signal, but the main steps are mainly identical. All the functions in eq. (3.10) are of the form $f(t,t') = \mathrm{Tr}_s\{a_s^{\dagger 2} e^{\mathcal{L}_s(t-t')} A(t')\}$ with a traceless operator $A(t')$ depending solely on t'. Again, we take the derivative of $f(t,t')$ with respect to t and find an equation of motion of the form $\partial_t \vec{v}_{t'}(t) = M\vec{v}_{t'}(t)$ with a column vector

$$\vec{v}_{t'}(t) = \mathrm{col}\left(\widetilde{\langle a_s^\dagger a_s\rangle}, \widetilde{\langle a_s^2\rangle}, \widetilde{\langle a_s^{\dagger 2}\rangle}\right), \tag{3.13}$$

where the expectation values with the tilde are defined in the usual way as the trace over the signal mode but with a density matrix given by $\tilde{\rho}_{t'}(t) = e^{\mathcal{L}_s(t-t')}A(t')$. The matrix M reads

$$M = \begin{pmatrix} -2\gamma_s & \chi\tilde{\alpha}_p & \chi\tilde{\alpha}_p^* \\ 2\chi\tilde{\alpha}_p^* & -2\gamma_s & 0 \\ 2\chi\tilde{\alpha}_p & 0 & -2\gamma_s \end{pmatrix}.$$

It is straight forward to diagonalize M. We write $M = U\Lambda U^{-1}$, with a similarity matrix U and Λ the diagonal form of M containing its eigenvalues $\lambda_1 = -2\gamma_s$, and $\lambda_{2,3} = -2\gamma_s \mp 2\chi|\tilde{\alpha}_p|$. We now solve for the vector $\vec{v}_{t'}(t)$, to find

$$\vec{v}_{t'}(t) = Ue^{\Lambda(t-t')}U^{-1}\vec{v}_{t'}(t') \equiv \sum_{n=1}^{3} e^{\lambda_n(t-t')}\, M_n \vec{u}_{A(t')}, \tag{3.14}$$

where we have defined the initial condition vector

$$\vec{u}_{A(t')} = \vec{v}_{t'}(t') = \begin{pmatrix} \mathrm{Tr}_s\{a_s^\dagger a_s A(t')\} \\ \mathrm{Tr}_s\{a_s^2 A(t')\} \\ \mathrm{Tr}_s\{a_s^{\dagger 2} A(t')\} \end{pmatrix}, \tag{3.15}$$

and the matrices $M_n = U\Pi_n U^{-1}$, where Π_n is a projector in the n'th "direction", that is, a matrix with zeros everywhere but in element (n,n) which is one.

Note that for the limit $\lim_{t\to\infty} \vec{v}_{t'}(t)$ to be uniquely defined, and therefore for $\mathcal{L}_s$ to be well-behaved, all the eigenvalues of M must satisfy $\mathrm{Re}\{\lambda_n\} < 0$, which in turn leads to a requirement for the displacement $\chi\tilde{\alpha}_p < \gamma_s$. This requirement is indeed fulfilled by choosing the mean-field displacement as mentioned above, see Sec. 3.3.1. In contrast, taking the classical solution as the displacement would lead to an ill-behaved $\mathcal{L}_s$ above and at the classical threshold point, that is, for $\sigma \geq 1$.

Coming back to the correlation functions in eq. (3.10), the general solution (3.14) allows us to write them all as

$$d_s(t,t') = \sum_{n=1}^{3} e^{\lambda_n(t-t')} d_{s,n}(t'), \tag{3.16}$$

with $d_{s,n}(t) = \left[M_n \vec{u}_{A(t)}\right]_3$ (the subscript denoting the third vector component), where d_s denotes any of the correlation functions $\{d_s^+, \tilde{d}_s^+, d_s^-, \tilde{d}_s^-\}$, for which A is taken, respectively, as $\{\delta a_s^{\dagger 2}\rho_s, \rho_s \delta a_s^{\dagger 2}, \delta a_s^2 \rho_s, \rho_s \delta a_s^2\}$. Let us emphasize that, just as with the pump mode, we have been able to write all the correlation functions of the signal mode into a form where the t dependence only enters in simple exponential factors.

Finally, let us show how this form for the correlation functions allows us to turn the c-MoP equations, which are coupled integro-differential equations, into coupled ordinary differential equations. For this aim, let us rewrite eqs. (3.5) and (3.6) as

$$\begin{aligned}\dot{\rho}_s(t) = \mathcal{L}_s \rho_s(t) + \frac{\chi}{2}\left[a_s^{\dagger 2}\langle a_p\rangle(t) - a_s^2 \langle a_p\rangle^*(t), \rho_s(t)\right] \\ + \left(\frac{\chi}{2}\right)^2 \left\{\left[a_s^2\,,\, h_s(t)\right] + \text{H.c.}\right\},\end{aligned} \tag{3.17}$$

$$\begin{aligned}\dot{\rho}_p(t) = \mathcal{L}_p \rho_p(t) + \frac{\chi}{2}\left[a_p \langle a_s^2\rangle^*(t) - a_p^\dagger \langle a_s^2\rangle(t)\,, \rho_p(t)\right] \\ + \left(\frac{\chi}{2}\right)^2 \left\{\left[a_p\,, \sum_{n=1}^{3} h_{p,n}(t)\right] + \text{H.c.}\right\},\end{aligned} \tag{3.18}$$

where we have defined the operators

$$\begin{aligned} h_s(t) &= \int_0^t dt' e^{\mathcal{L}_s(t-t')} \mathcal{K}_s(t,t')\rho_s(t'), \\ h_{p,n}(t) &= \int_0^t dt' e^{\mathcal{L}_p(t-t')} \mathcal{K}_{p,n}(t,t')\rho_p(t'), \end{aligned} \tag{3.19}$$

with the superoperator $\mathcal{K}_{p,n}$ defined as $\mathcal{K}_p$ in eq. (3.8), but with the correlation functions $d_{s,n}(t)$ instead of $d_s(t)$. Using their definition, and the solutions found for the correlation functions, eqs. (3.12) and (3.16), their evolution equations are found to be

$$\partial_t h_s(t) = (-\gamma_p + \mathcal{L}_s) h_s(t) + \mathcal{K}_s(t,t)\rho_s(t), \tag{3.20}$$

$$\partial_t h_{p,n}(t) = (\lambda_n + \mathcal{L}_p) h_{p,n}(t) + \mathcal{K}_{p,n}(t,t)\rho_p(t). \tag{3.21}$$

Together with eqs. (3.17) and (3.18), these form a closed set of coupled nonlinear ordinary differential equations for the reduced states ρ_s and ρ_p, and the traceless operators h_s and $\{h_{p,n}\}_{n=1,2,3}$. These are the equations that we analyze further in the remainder of this chapter.

Overall we have shown for the example of the DOPO that it is indeed possible to rewrite the integro-differential c-MoP equations into a set of ordinary differential equations. Whereas in the integro-differential form of the c-MoP equations we would need to solve for $D_s^2 + D_p^2$ variables, the ordinary differential form requires to solve for a number of $2D_s^2 + 4D_p^2$ variables. Here, $D_{s(p)}$ denotes the Hilbert space dimension of the signal (pump) state for an adequate numerical truncation. Given the complications of solving an integro-differential c-MoP equation numerically, see the details in Sec. 2.2.1, especially when aiming for the steady state, the ordinary differential form of the c-MoP equations is much more favorable despite the larger number of variables.

The steps presented here are quite general and can be pursued for all c-MoP equations describing any physical system. The complexity of the resulting set of coupled equations will depend on the complexity of the subparts of the full quantum system, here given by the complexity of the local Liouvillians $\mathcal{L}_p$ and $\mathcal{L}_s$. Both local Liouvillians of the DOPO are quadratic in the field operators allowing to find simple expressions for the correlation functions appearing in the integral kernels of the Born terms as explained above in this Section. In particular, we only need up to three eigenvalues of $\mathcal{L}_p$ and $\mathcal{L}_s$ for an exact calculation of the two-time correlation functions. As a consequence the number of coupled differential equations for matrix-valued variables increases from 2 integro-differential equations to 6 ordinary differential equations.

To further illustrate the scaling behavior of this idea, let us consider a bipartite system with coupled subparts A and B with Hilbert space dimensions D_A and D_B, respectively. Within the integro-differential form of the c-MoP approach we find two coupled equations for the reduced states $\rho_A(t)$ and $\rho_B(t)$ which requires to solve for $(D_A)^2 + (D_B)^2$ variables. In the general case in which the local Liouvillians $\mathcal{L}_A$ and $\mathcal{L}_B$ do not allow for an analytic solution of the two-time correlation functions in the Born terms, we would need to numerically diagonalize $\mathcal{L}_A$ and $\mathcal{L}_B$ as it has been explained in the driven and dissipative many-body example of Sec. 2.2.2. In this case, every eigenvalue of the local Liouvillians generates a new matrix-valued variable. As a result, the coupled ordinary differential equation form of the c-MoP approach requires to solve for a total of $(D_B)^2 \times (D_A)^2 + (D_A)^2 \times (D_B)^2$ variables which scales even worse than the number of variables needed to solve the full Liouville-von Neumann equation. Thus, the advantage of the approach presented here over a direct numerical integration of the integro-differential c-MoP equations is only present for cases where the local Liouvillians do not have a nonquadratic internal structure which includes a vast number of nonlinear quantum optical models such as those for nondegenerate or multi-mode parametric oscillation [85–88], lasing [4, 6, 7, 89], optomechanics [69], or the dissipative Dicke model [38, 91, 92]. For the latter we will present results within the framework of this thesis in Chapter 5

Finally, we remark that the c-MoP equations preserve the trace and the hermiticity but they do not guarantee for the positivity of the density matrix. Such an issue is not unusual for projection operator theories, in fact, the same conditions can be found in the well established Redfield equations [43, 44]. Obviously whenever the c-MoP equations provide a good approximation, they will yield a positive density matrix. Hence the positivity of the eigenvalues can be used as a consistency test for the approximation. Sometimes, the numerical results give negative entries on the diagonal elements of the density matrix, but with a magnitude which is too small to contribute.

3.3.3 Exact limits: The adiabatic and the diabiatic limit

In standard open system theory one relies on a separation of time scales between the system dynamics and the environmental relaxation rates as explained in Sec. 1.2. An equivalent reasoning is applied in adiabatic elimination approaches, where in the case of the DOPO one relies on a separation between the rates γ_p and γ_s at which the pump and the signal, respectively, relax to the steady state of their unperturbed Liouvillians $\mathcal{L}_p$ and $\mathcal{L}_s$. The c-MoP theory can, in fact, be understood as a generalization of adiabatic elimination procedures where one considers the back-action of the "system" onto the "environment". We will now show that the effective equations for the reduced state of the signal known in the adiabatic [20] and the diabatic [39] limits can, indeed, be obtained as limiting cases of the c-MoP equations.

The adiabatic limit in which the time scale of the pump mode is much faster than the time scale of the signal mode is defined such that $\gamma_p/\gamma_s \to \infty$ while $\gamma_s\gamma_p$ is kept finite. The diabatic limit describes the opposite scenario where $\gamma_p/\gamma_s \to 0$. We proceed by comparing the Born terms with the free evolution operators $\mathcal{L}_p$ and $\mathcal{L}_s$, for which we consider the scaling of h_s/γ_s and $h_{p,n}/\gamma_p$, which can be obtained by simple inspection of eqs. (3.20) and (3.21) divided by γ_s and γ_p, respectively.

In the adiabatic limit, we infer from eq. (3.21)/γ_p that $h_{p,n}(t)/\gamma_p = 0$ for all n and $t \geq 0$. Introducing this result into eq. (3.18), we see that the state of the pump will be coherent with a field amplitude obeying the equation of motion

$$\partial_t\langle a_p\rangle = \epsilon_p - \gamma_p(\langle a_p\rangle + \tilde{\alpha}_p) - \frac{\chi}{2}\langle a_s^2\rangle. \tag{3.22}$$

Additionally, eq. (3.20)/γ_s leads to $h_s(t)/\gamma_s = \mathcal{K}_s(t,t)\rho_s(t)/\gamma_s\gamma_p = \rho_s(t)\delta a_s^{\dagger 2}(t)/\gamma_s\gamma_p$, where we have used eqs. (3.7) and (3.12) and the fact that when the pump is in a coherent state all the expectation values in eq. (3.12) cancel. Introducing this result into eq. (3.17), together with the steady-state solution of eq. (3.22) for $\langle a_p\rangle$, we end up with the effective master equation of the signal mode in the adiabatic limit

$$\gamma_s^{-1}\partial_t\rho_s = \frac{\sigma}{2}\left[a_s^{\dagger\,2} - a_s^2\,,\,\rho_s\right] + \frac{g^2}{4}D_{a_s^2}\rho_s + D_{a_s}\rho_s, \tag{3.23}$$

where $\sigma = \epsilon_p\chi/\gamma_p\gamma_s$ is an injection parameter corresponding to a coherent exchange of excitations between the signal and pump modes, while $g^2 = \chi^2/\gamma_p\gamma_s$ accounts for signal photon pairs that are lost to the strongly damped pump mode. Eq. (3.23) has been extensively studied in the literature [12, 93, 107]. It can be derived via standard adiabatic elimination which in the language of projection operator theory uses a time-independent projection superoperator $\mathcal{P}_{\text{ad}}$ projecting out the coherent laser field [20]. Its action on the full density matrix is given by $\mathcal{P}_{\text{ad}}\,\rho(t) \equiv |\alpha\rangle\langle\alpha| \otimes \rho_s(t)$, where $|\alpha\rangle$ is a coherent state with $\alpha = \epsilon_p/\gamma_p$. The fast exponential decay $e^{-\gamma_p(t-t')}$ of the pump correlation functions allows in this case for a Markovian approximation in the Born terms, that is $\int_0^t dt' e^{\mathcal{L}_s(t-t')}\mathcal{K}_s(t,t')\rho_s(t') \approx \mathcal{K}_s(t,t)\rho_s(t)/\gamma_p$.

Let us now analyze the c-MoP equations in the diabatic limit. There, eq. (3.20)/γ_s provides us with $h_s(t)/\gamma_s = 0$, which introduced in eq. (3.17) leads to an effective master equation

$$\dot{\rho}_s(t) = \frac{\chi}{2}\left[\langle a_p\rangle a_s^{\dagger\,2} - \langle a_p\rangle^* a_s^2\,,\rho_s(t)\right] + D_{a_s}\rho_s(t)\,. \tag{3.24}$$

for the signal state. The pump state only enters this equation trough the amplitude $\langle a_p\rangle$ which obeys eq. (3.22) since $h_{p,n}$ is traceless. Noting that this equation is equivalent to eq. (3.11), we conclude that the diabatic limit reduces the full c-MoP equations to the mean-field equations. In contrast to the adiabatic limit, we are not aware of any projection operator based approach, apart from the one presented here with a self-consistent projector, which describes the diabatic limit.

We emphasize that within these limits both eqs. (3.11) and (3.23) become exact which can be understood from the full generalized Nakajima-Zwanzig Kernel of the c-MoP theory, see Sec 1.4. The exact kernel includes a time-ordered dynamical map given by $\hat{T}e^{\int_{t'}^{t} dt'(\mathcal{L}_0+\mathcal{C}_{t'}\mathcal{L}_I)}$ with the time-ordering operator $\hat{T}$. In the case of the DOPO we have $\mathcal{L}_0 = \mathcal{L}_p+\mathcal{L}_s$ and the projector $\mathcal{C}_t = \mathbb{1}-\rho_p(t)\otimes\mathrm{Tr}_p\{\cdot\}-\rho_s(t)\otimes\mathrm{Tr}_s\{\cdot\}$ which projects onto signal-pump correlations. In the Born approximation we drop the interaction part from this exponential. Such a step becomes exact in cases where $(t-t')\mathcal{L}_0$ dominates completely over $(t-t')\mathcal{C}_{t''}\mathcal{L}_I$ for a fixed $t''\in[t',t]$.

We have thus shown that the c-MoP theory provides us with exact equations of motion in the limits $\gamma_p/\gamma_s\to\infty$ (adiabatic) and $\gamma_p/\gamma_s\to 0$ (diabatic) where it therefore becomes equivalent with well established theories [20, 39]. We will now step beyond the cases in which time-scale separation is present and use the c-MoP theory to access the signal state in the $\gamma_p\approx\gamma_s$ scenario.

3.4 Accuracy tests and full quantum states of the signal mode

In the previous sections we have shown how to deal with the non-Markovian structure of the c-MoP equations. The only remaining difficulty is given by the quartic structure of the effective equations of motion derived for the signal mode, eqs. (3.17) and (3.20). In this section we will treat the problem numerically in the Fock state basis by introducing a truncation D_s for the Hilbertspace $\mathcal{H}_s$ of the signal, where D_s is chosen such that the results for the observables we are interested in converge up to some desired accuracy. Thus, the reduced state ρ_s and the operator $h_s(t)$ will be $D_s\times D_s$ dimensional matrices. We will not change into the superspace representation here in contrast to the approach presented in Sec. 2.2.2.

Instead of treating the pump mode in an analogous manner, we exploit the fact that the c-MoP equations of the pump mode (3.18) and (3.21) are quadratic in the bosonic operators. As a consequence we are able to describe the pump state by a set of five variables only, the mode amplitude $\langle a_p\rangle$ plus the fluctuations $\langle a_p\delta a_p\rangle$ and $\langle a_p^\dagger\delta a_p\rangle$ (note that the first two are complex variables). These five variables can be determined by solving Eqs. (3.18) and (3.21) as a function of the signal state $\rho_s(t)$ for

14 variables which includes the pump field amplitudes $\langle a_p \rangle(t)$, $\langle a_p^\dagger \rangle(t) = \langle a_p \rangle^*(t)$ and the fluctuation variables $\mathrm{Tr}_p\{a_p^\dagger \delta a_p A(t)\}$, $\mathrm{Tr}_p\{a_p \delta a_p A(t)\}$ and $\mathrm{Tr}_p\{a_p^\dagger \delta a_p^\dagger A(t)\}$ with $A(t)$ being either $h_{p,1}(t)$, $h_{p,2}(t)$, $h_{p,3}(t)$ or $\rho_p(t)$. At the end, we are thus effectively left with two coupled nonlinear differential equations for the matrices $\rho_s(t)$ and $h_s(t)$. The number of variables in our c-MoP simulation amounts to $2D_s^2 + 14$.

In the following we compare the steady states of the classical theory from eq. (3.2), the steady states of the mean-field equations (3.11), and the steady states of the c-MoP equations. In order to show the accuracy of the latter we also determine the steady state of the full Liouville-von Neumann equation (3.1) in parameter regimes where it is numerically tractable. This numerical simulation is done as follows: first, we eliminate the large coherent background of the laser drive from the Liouvillian $\mathcal{L}$ by writing $a_p = \alpha_p + \delta a_p$, where α_p is taken to be the classical steady-state solution of eqs. (3.2); then, we use the superspace formalism, where the steady-state operator ρ_{ss} and the Liouville superoperator $\mathcal{L}$ are represented, respectively, by a vector $\vec{\rho}_{ss}$ and a matrix $\mathbb{L}$, and $\vec{\rho}_{ss}$ can be found as the eigenvector with zero eigenvalue of $\mathbb{L}$ [62, 107]. As the dimension of the matrix $\mathbb{L}$ is $(D_p \times D_s)^2$, with D_p denoting the pump mode's Hilbert space dimension, this exact simulation is limited to small photon numbers.

In all the simulations we consider cases without time-scale separation between the two modes and rescale all units to the dissipation rates, i.e. we put $\gamma_p = \gamma_s = 1$. The only remaining parameters are the nonlinear coupling χ and the injection parameter $\sigma = \epsilon_p \chi$.

In Fig. 3.2 we present results in parameter regimes where the full DOPO equation (3.1) can be solved numerically. In Figs. 3.2$(a) - (c)$ and 3.2$(d) - (f)$ we show different steady-state observables for $\chi = 1$ and $\chi = 0.1$, respectively. It can be appreciated how the c-MoP results (blue solid line) coincide almost perfectly with the numerical results from the full master equation (red stars). The observables that we show are the pump mode's amplitude $\langle a_p \rangle$ in Figs. 3.2(a) and 3.2(d), the signal photon number $\langle a_s^\dagger a_s \rangle$ in Figs. 3.2(b) and 3.2(e), and the $g^{(2)}$ function $g_s^{(2)}(0) \equiv \langle a_s^{\dagger 2} a_s^2 \rangle / \langle a_s^\dagger a_s \rangle^2$ of the signal in Figs. 3.2(c) and 3.2(f). We also compare with the mean-field predictions of eqs. (3.11) (black dashed line), which in this context should be understood as the c-MoP theory up to first order, and with the classical steady-state solutions (gray thin solid line) given after eq. (3.2). Let us remark that despite the nonlinear nature of the mean-field and the c-MoP equations, we only find one physical solution for each of them.

All four theories agree quite well far below the critical point $\sigma = 1$ as the states of the signal and pump modes are close to vacuum and a coherent state induced by the external laser drive, respectively. Far above the threshold point, where the classical theory is expected to be approximately valid, we find that both the c-MoP predictions and the full numerics agree well with the classical solutions for all observables, but with the fundamental difference that the classical theory breaks the Z_2 symmetry, while c-MoP and the full solution preserve it. The mean-field solution, on the other hand, fails to describe the state of the signal above threshold as can be

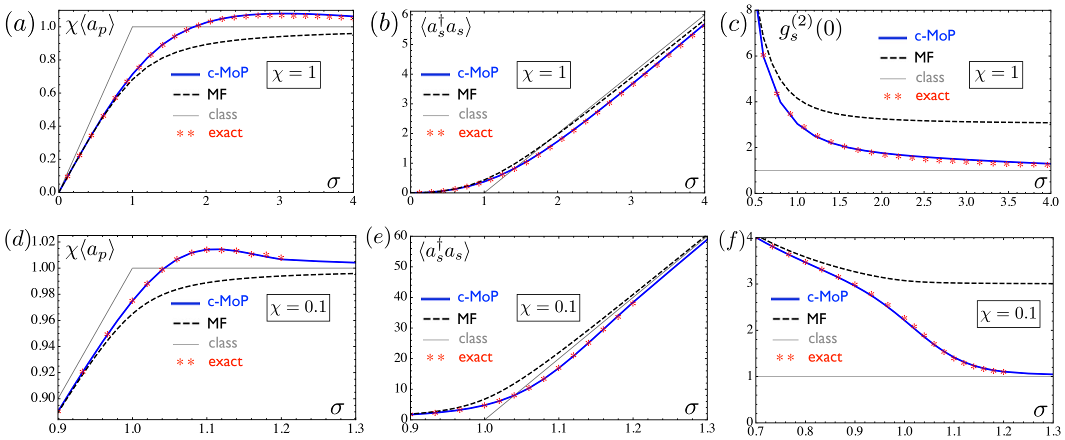

Figure 3.2: Accuracy tests of the c-MoP theory for steady-state expectation values as a function of the injection parameter σ. In all plots we set $\gamma_p = \gamma_s = 1$. The cases $\chi = 1$ and $\chi = 0.1$ are considered in (a)-(c) and (d)-(f), respectively. The rescaled pump amplitude $\chi\langle a_p\rangle$ is shown in (a) and (d); (b) and (e) show the signal photon number $\langle a_s^\dagger a_s\rangle$; finally, (c) and (f) show the $g^{(2)}$ function of the signal, which is equal to 1 for a coherent state (or a balanced mixture of coherent states differing only in phase). The gray thin solid lines show the classical prediction from eqs. (3.2), showing that the classical threshold where the signal field is switched on lies at $\sigma = 1$. The blue solid curves represent the results obtained from the numerical solution of the c-MoP equations (3.17), (3.18), (3.20), and (3.21). The red stars show the result obtained from the full master equation (3.1) up to injection parameters σ where the numerics are tractable for us. Finally, the black dashed curves represent the mean-field theory, see eq. (3.11). Apart from the classical solution, all theories conserve the Z_2 symmetry, i.e. $\langle a_s\rangle = 0$.

appreciated from the $g^{(2)}$ function in Figs. 3.2(c) and 3.2(f). As expected, mean-field theory and the classical theory break down in the vicinity of the threshold point. Remarkably, this is not true for c-MoP which appears to give quasi exact results for all values of σ, even in cases where the interaction rate χ is comparable to all other system parameters.

For the experimentally relevant scenario with $\chi \ll 1$, the Hilbert space dimension needs to be so large that we are not able to find the numerical solution of the full master equation (3.1) for injection parameters close to (or above) threshold. However, we can compare the c-MoP predictions (red stars), see Fig. (3.5), with the perturbative approach which Drummond et al. (dark yellow dot-dashed line) developed in the vicinities of the critical point, by making a consistent multiple-scale expansion of the system's stochastic variables within the positive P representation [96, 97]. This procedure has the virtue of being valid for any values of γ_p and γ_s, and close to threshold, concretely for $|\sigma - 1| < \chi/\sqrt{2\gamma_p\gamma_s}$ it is expected to be quasi-exact. As shown in Figs. 3.5(a) and 3.5(b), we find perfect agreement between this approach and the c-MoP theory for $\chi = 0.01$.

Overall, we have indeed shown the drastic impact of the Born terms, which do not only lead to a quantitative improvement as compared to the classical theory or to mean-field, but to a qualitatively different state of the signal mode. The classical theory predicts a coherent state, while the mean-field theory, i.e. the c-MoP theory up to first order, predicts a Gaussian state of the signal centered around $\langle a_s \rangle = 0$ [104]. The c-MoP theory including the born terms, hence including signal-pump correlations within a projection operator based theory, is capable of finding the full quantum state of the signal which is neither coherent nor Gaussian as shown through the $g^{(2)}$ function in Figs. 3.2(c) and 3.2(f).

In order to illustrate the full quantum state, we plot the Wigner function $W(x_s, p_s)$ of the signal density matrix obtained from the c-MoP equations in Fig. 3.3(a) for $\chi = 0.1$ and different values of σ. Let us remark that in our case in which the Wigner function is positive everywhere in the phase-space formed by the quadratures $x_s = a_s^\dagger + a_s$ and $p_s = i(a_s^\dagger - a_s)$, it can be simply interpreted as the joint probability distribution describing the statistics of measurements of these observables [83, 84, 106]. From a computational point of view, we evaluate it from the steady-state density matrix following the method detailed in [108]. Far below threshold, the Wigner function shows a perfect vacuum for the signal state, see top panel of Fig. 3.3(a) for $\sigma = 0$ as a reference. As we cross through the critical point, two significant effects take place. First, approaching the threshold we find the well-known quadrature-noise reduction or squeezing [20, 109, 110], which is highest around the critical point $\sigma = 1$ [97], and reaches its asymptotic value $\langle \delta p_s^2 \rangle = (\gamma_s + \gamma_p)/(2\gamma_s + \gamma_p)$ for $\sigma \to \infty$, with corresponding antisqueezing $\langle \delta x_s^2 \rangle = 1 + \gamma_s/\gamma_p$ [104]. Second, as we cross the threshold we appreciate how the state develops two peaks centered (asymptotically) at the quadrature values predicted by the classical solution. Hence, even though the true quantum state always preserves the Z_2 symmetry, it does so in two qualitatively different ways depending on whether we are below or above threshold. This behavior is reminiscent of the one appearing in the adiabatic limit [12], and it has been recently observed for the first time by making use of a circuit QED architecture [111].

In retrospect, we see that the symmetry-breaking states predicted above threshold by the standard linearization approach correspond each to one of the two distinct peaks appearing in the exact state. Far above threshold $\sigma \gg 1$ the two peaks have zero overlap and such states provide reasonable predictions for all observables which are not sensitive to symmetry breaking, that is, all observables containing even numbers of signal field operators. Of course, such a deficit can be corrected by simply using a balanced mixture of the symmetry-breaking states [104]; this construction will guide us in the next section, where we will perform a Gaussian state approximation which necessarily breaks the Z_2 symmetry. It is then close to the critical point where both linearization and mean-field approaches fail, whereas c-MoP provides an accurate description of the quantum state.

Let us remark that we have compared the Wigner function obtained from the c-

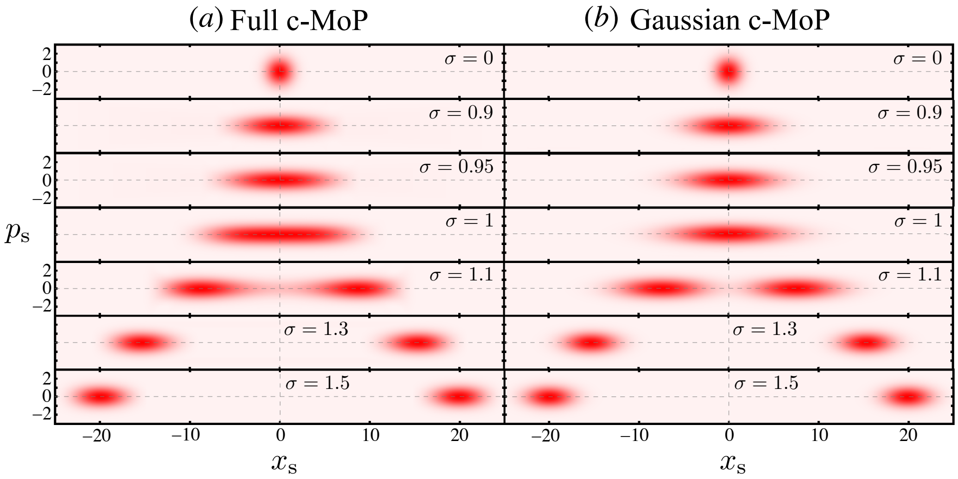

Figure 3.3: Wigner functions of the c-MoP density matrix for the signal mode without (a) and with (b) the Gaussian state approximation for $\gamma_p = \gamma_s = 1$, $\chi = 0.1$, and for different values of σ. In the absence of injection, $\sigma = 0$, the signal state is in vacuum. Upon approaching the threshold, it becomes squeezed, with the highest squeezing levels obtained around $\sigma = 1$. Above threshold two symmetric peaks appear and the squeezing reaches some asymptotic value as we move away from threshold. Note how above threshold the state can be approximated by a balanced mixture of two symmetry breaking states. Indeed, let us remark that while for $\sigma < 1$ we are plotting the unique solution that appears when applying the Gaussian state approximation onto the c-MoP equations (which we have called below threshold solution in the text), for $\sigma > 1$ we have chosen to plot the Wigner function corresponding to a balanced mixture of the two above threshold symmetry breaking solutions with opposite phase which coexist with the symmetry-preserving Gaussian solution.

MoP theory with the reduced signal states obtained from the full master equation, which was only possible for $\sigma \leq 1.2$, and found very good agreement, the differences being completely unnoticeable to the naked eye. We emphasize again that, with the numerical solution of the c-MoP equations we are able to find the full reduced density matrices of the modes away from the adiabatic limit. This is in contrast to other approaches such as stochastic simulations [96–98] or the Keldysh formalism [99–101] which are naturally designed to provide expectation values of the system operators.

3.5 Comparison to the Keldysh formalism

So far, we have been mainly comparing the quantitative predictions of the c-MoP theory to the predictions of the semi-classical approach and to a mean-field ansatz [39]. We now also compare the c-MoP performance with nonequilibrium many-body

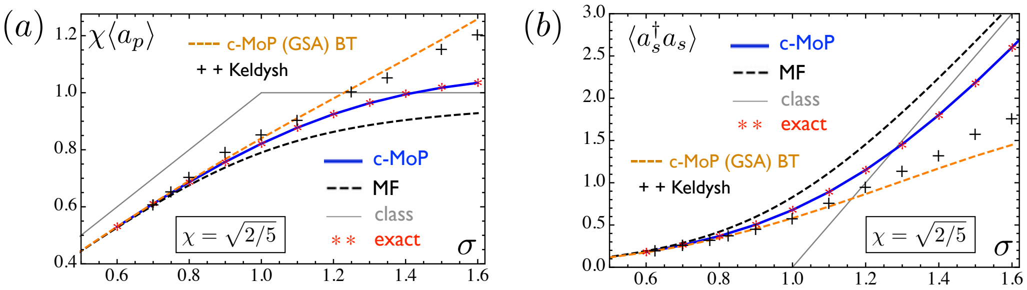

Figure 3.4: Performance test of the c-MoP theory with and without the Gaussian state approximation in comparison with the Keldysh approach [99] for steady-state observables as a function of the injection σ. The remaining parameters are $\gamma_p = \gamma_s = 1$ and $\chi = \sqrt{2/5}$. We show the rescaled pump field amplitude $\chi\langle a_p \rangle$ and the signal photon number $\langle a_s^\dagger a_s \rangle$ in (a) and (b), respectively. The red stars show the results obtained from an exact solution of the Liouville-von Neumann equation. The blue solid line shows the results obtained from the full c-MoP eqs. (3.17), (3.18), (3.20), and (3.21). For comparison, the results of the Keldysh approach obtained from an extraction of the data of Ref. [99] are shown by the black + signs. The orange dashed curve represent the below threshold solution obtained from a Gaussian state approximation on the c-MoP equations. The black dashed curve displays the results of mean-field theory, and finally the gray thin solid lines represent the prediction of the classical theory.

techniques beyond mean-field which have been successfully applied to the DOPO [99–101]. For this purpose we extract the signal photon number and the pump field amplitude from Reference [99] where a Keldysh treatment has been conducted in order to find the nonequilibrium steady state of the DOPO. The parameters investigated in Ref. [99] are $\gamma_p = \gamma_s = 1$ and $\chi = \sqrt{2/5}$. In Fig. 3.4 we compare the c-MoP results with (orange dashed line) and without Gaussian state approximation (blue solid curve), for the former see Sec. 3.6, the Keldysh formalism results (black + signs), mean-field (black dashed line) and finally the classical predictions (gray thin line) to exact results (red stars).

As expected from the results of Sec. 3.4 we find the c-MoP theory to give quasi exact solutions while the Keldysh results deviate from the exact numerical solution. The quantitative accuracy of the Keldysh approach can be compared to the accuracy of the Gaussian c-MoP theory which we present in the next section. However, similar to the Gaussian c-MoP theory the Keldysh approach features a symmetry broken solution above threshold. This solution has not been shown for the investigated parameters in Ref. [99]. We emphasize, that the approach presented in Ref. [99] is a self-consistent Hartree-Fock calculation which means that it is exact up to χ^2 within the diagrammatic Keldysh framework. In that sense the comparison between c-MoP theory in Born approximation and the self-consistent Hartree-Fock Keldysh approach is based on equal grounds.

Most importantly, however, we exemplify with the results for the DOPO model that the c-MoP theory differs from the Keldysh approach. Within the framework of this thesis it has not been possible to investigate the details of many-body field theoretical approaches and to draw an elaborate comparison to the c-MoP theory. Nonetheless, we would like to comment on the possibly most important difference between the c-MoP theory and nonequilibrium Green's function methods, in particular the Keldysh formalism.

In Ref. [99] the quantity of interest is for example given by the exact two-point Green's function $\langle T_C S_C a_s^\dagger a_s \rangle$, with the time-ordering operator T_C on the Keldysh contour and $S_C = T_C e^{-i \int_C d\tau H_I(\tau)}$ the time evolution operator in the interaction picture. Most importantly, the trace is taken over a density matrix which allows for the application of Wick' theorem meaning that the state is Gaussian. In Ref. [99] the steady state of the mean-field equations are used as the reference state. Up to this point the Keldysh formalism is exact. The approximation enters via expanding S_C as a Dyson series in powers of the interaction which can be done in two ways. One way leads to a perturbative approximation by cutting the Dyson series at some order. In this case the exact two-point Greens' function will depend on "free" two-point Greens' functions only due to contractions according to Wick's theorem. Alternatively, in the self-consistent treatment as performed in Ref. [99] the bare Greens' functions are replaced by the interacting Greens' functions in the resummed Dyson equation. This leads to a formally exact and closed nonlinear equation for the exact two-point Green's functions. We emphasize, however, that within the second order of the self energy n-point Green's function with $n > 2$ are not accounted for in the Keldysh framework. Overall, one can say that higher correlations are formed from Green's functions and vertices, reducing the degrees of freedom to some finite n in the extent to which n-point functions are being considered.

In contrast the c-MoP theory, relies on density matrices which at every vertex point account for all possible correlation functions up to arbitrary order, at least for correlation functions which are local on the Hilbert spaces of either the pump or the signal. Thus c-MoP accounts for everything but the weakest connections remaining in the (fluctuations of the) signal-pump interaction. Thus, we can suppose that the c-MoP approach of a certain power in the interaction is indeed more powerful than a self-consistent diagrammatic Keldysh approach [99] of that same power. And, indeed, we have exemplified such an observation in this section. However, the computational effort of c-MoP scales with system-size of the local Hilbert spaces whereas the Keldysh method does not.

Moreover, we like to mention that many other theoretical techniques, including dynamical mean-field theory [112], have been developed based on the Keldysh formalism. Thus, we expect the c-MoP theory to differ from dynamical mean-field theory as well. Certainly, it is an intriguing task for future research to further investigate the differences between field theoretical approaches and the c-MoP approach, and even aim for a strong combination of the two theories.

3.6 Gaussian state Approximation within the c-MoP theory

Despite the fact that the complexity of solving the c-MoP equations fully numerically scales in a more favorable way than the numerical complexity of the full master equation, it still requires to integrate a number of differential equations that scales quadratically with the dimension of the truncated Hilbert space for the signal field. Therefore, it is very desirable to find an effective description of the underlying theory which is numerically more efficient and can thus cover the whole parameter space. In the remainder of this section, we implement such an idea by applying a Gaussian state approximation (GSA) consistent with the c-MoP equations (3.5) and (3.6).

Another great advantage of a Gaussian theory, apart from reaching the whole parameter space, is the efficiency in the evaluation of both steady states and dynamical quantities such as two-time correlation functions. The disadvantage of a Gaussian theory, however, is the lack of quantitative accuracy especially in the vicinity of the critical point. Nonetheless, as we show in the following, a Gaussian theory consistent with the c-MoP equations offers better quantitative accuracy than any of the previously developed Gaussian methods, particularly linearization around the classical solution or the recently-developed self-consistent linearization [104].

The general procedure for finding a GSA for the state of a certain bosonic master equation is very simple. In a first step, we write the bosonic operators as $a_j = \alpha_j + \delta a_j$, with $\alpha_j = \langle a_j \rangle$, such that $\langle \delta a_j \rangle = 0$. In the next step we find the evolution equation for the first and second moments, which will depend on higher-order moments in general. Thus, in the final step we assume the state to be Gaussian at all times, so that all higher order moments factorize into products of first and second order moments [20, 104]; in particular, we will encounter third order moments such as, e.g. $\langle \delta a_s^{\dagger 2} \delta a_s \rangle$, which vanish identically within the GSA, and forth order moments which factorize according to, e.g.

$$\begin{aligned} \langle \delta a_s^{\dagger 4} \rangle &\approx 3 \langle \delta a_s^{\dagger 2} \rangle^2, \\ \langle \delta a_s^{\dagger 3} \delta a_s \rangle &\approx 3 \langle \delta a_s^{\dagger 2} \rangle \langle \delta a_s^{\dagger} \delta a_s \rangle, \\ \langle \delta a_s^{\dagger 2} \delta a_s^2 \rangle &\approx \langle \delta a_s^{\dagger 2} \rangle \langle \delta a_s^2 \rangle + 2 \langle \delta a_s^{\dagger} \delta a_s \rangle^2. \end{aligned} \tag{3.25}$$

After this final step, we are then left with a closed set of nonlinear equations for the amplitudes α_j and the second order moments of the fluctuations δa_j that have to be solved self-consistently.

The standard linearization theory can be understood as a GSA on the full master equation, but with the exception that the amplitudes α_j are not determined self-consistently, but are obtained from the classical theory. As shown by the gray thin solid line in Fig. 3.5(b) the complete suppression of quantum fluctuations when determining these amplitudes leads to unphysical results at the threshold point in the DOPO.

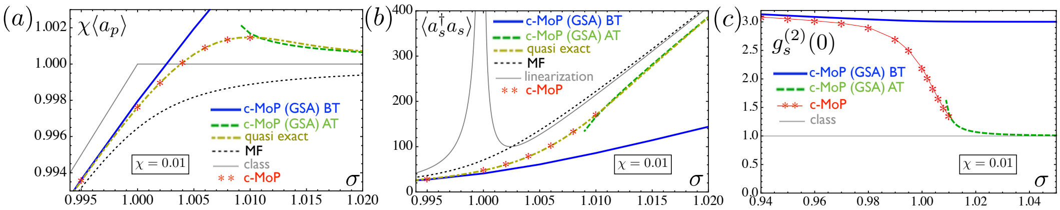

Figure 3.5: Accuracy tests of the c-MoP theory with and without the Gaussian state approximation for steady-state observables as a function of the injection σ. In all the plots we set $\gamma_p = \gamma_s = 1$ and $\chi = 0.01$. As in Fig. 3.2, we show the rescaled pump field amplitude $\chi\langle a_p\rangle$, the signal photon number $\langle a_s^\dagger a_s\rangle$, and the $g^{(2)}$ function of the signal, in (a), (b), and (c), respectively. The red stars show the results obtained from the c-MoP eqs. (3.17), (3.18), (3.20), and (3.21), up to injection parameters σ where the numerics are tractable. For comparison, the quasi exact method of Drummond and collaborators [96, 97] is shown as a dark yellow dot-dashed line. The blue solid and the green dashed curves represent the below and above threshold solutions, respectively, obtained from a Gaussian state approximation on the c-MoP equations. The black thin dotted curve displays the results of mean-field theory, see eq. (3.11), which in this context can be understood as the below threshold solution of a Gaussian state approximation on the full master equation (3.1). Finally, the gray thin solid lines represent the prediction of the standard linearization theory in (a) and (b), and the coherent-state prediction $g^{(2)} = 1$ of the classical equations (3.2) in (c).

The self-consistent linearization method, as it is coined in Ref. [104], goes one step beyond standard linearization by consistently finding the amplitudes α_j from the GSA still applied to the full master equation. Due to the nonlinear nature of the resulting equations of motion, one can find several solutions in a given point of parameter space. However, it was shown that at the end only two types of solutions were physical, qualitatively similar to the solutions found from standard linearization, but quantitatively regularized in such a way that the unphysical results of the latter disappear. In particular, a below threshold (BT) solution was found, which does not break the Z_2 symmetry, i.e. $\alpha_s = 0$, but in contrast to the classical theory exists for all values of the injection parameter, not only for $\sigma < 1$. Two above threshold (AT) solutions were also found. These solutions have opposite phase and break the symmetry, that is, $\langle a_s\rangle = \pm|\alpha_s| \neq 0$, but appear only above a certain injection parameter $\sigma > 1$ which is larger than the classical threshold value. Interestingly, we point out that the BT solution found through this self-consistent linearization is exactly equivalent to the mean-field theory introduced in Sec. 3.3.1.

Motivated by these findings, we apply a GSA to the c-MoP equations. Concretely, we calculate all first and second order moments of the pump and signal fluctuations from the c-MoP eqs. (3.17), (3.18), (3.20), and (3.21), and apply the factorization of higher order moments as explained above. In strong contrast to the GSA on the full master equation, we do not need to assume a Gaussian form for the full state ρ

but only for the reduced state of the signal ρ_s. Hence, we expect similar qualitative results but with a higher quantitative accuracy.

Indeed, this is what we find and illustrate in Fig. 3.5 for $\gamma_p = \gamma_s = 1$ and $\chi = 0.01$. We plot steady-state expectation values for the pump amplitude $\chi\langle a_p\rangle$ in Fig. 3.5(a), the signal photon number $\langle a_s^\dagger a_s\rangle = \langle \delta a_s^\dagger \delta a_s\rangle + |\alpha_s|^2$ in Fig. 3.5(b), and the $g^{(2)}$ function of the signal in Fig. 3.5(c), all as a function of the injection parameter σ. The blue solid line shows the below threshold solution of the GSA on the c-MoP equation, while the green dashed line illustrates the above threshold solution. The latter fulfills $\langle \delta a_s^\dagger \delta a_s\rangle \ll |\alpha_s|^2$ and is therefore more likely to provide physically consistent results than the BT solution whenever they coexist. In Fig. 3.5(c) we show how the AT solution indeed gives the correct value for the $g^{(2)}$ function, what indicates that each of the AT solutions corresponds to one of the lobes of the Wigner function, see Fig. 3.3(a). In order to illustrate this point even further, we show in Fig. 3.3(b) the Wigner function [83, 84, 106] corresponding to the GSA on the c-MoP equations (as explained in the previous section, above threshold we take the balanced mixture of the two symmetry breaking solutions, such that the resulting state preserves the Z_2 symmetry).

Importantly, there is an increased quantitative accuracy of the BT solution obtained from the c-MoP theory as compared with the mean-field theory (or the self-consistent linearization), see Figs. 3.5(a) and 3.5(b), for parameters below and especially at the classical threshold point. As mentioned in Sec. (3.4) we test the accuracy of our method by comparing with the quasi exact method of Drummond and collaborators [96, 97], illustrated by the dark yellow dot-dashed line in Figs. 3.5(a) and 3.5(b). This increase in accuracy can be attributed to the born terms, since the mean-field equations can be understood on the one hand as the first order approximation of the c-MoP theory, and on the other hand as the below threshold solution of the GSA on the full master equation of the DOPO.

To summarize this section, we have shown that the c-MoP equations also provide a highly accurate Gaussian theory which is still as effective as every other linearized theory but, in contrast, it takes significant signal-pump correlations into account. This is relevant because, as stated above, a Gaussian theory has the virtue that both steady-state as well as dynamical quantities such as two-time correlation functions can be found efficiently for any time and set of parameters. To emphasize this practical aspect of the GSA, we will show in Sec. 3.7 that the level of accuracy that we have found here in the evaluation of the steady states is also present in the transient time evolution.

3.7 Dynamics

So far we have only presented steady-state quantities for the various methods of our interest. In this section we will briefly elaborate on the possibility to simulate dynamical evolution as well. The steady state of the full master equation (3.1)

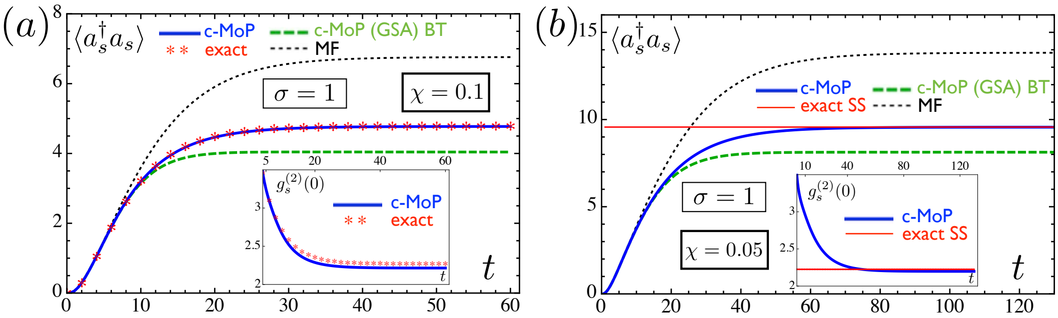

Figure 3.6: Accuracy tests of the c-MoP theory for transient time evolution. The initial state is chosen to be the vacuum. We set $\gamma_p = \gamma_s = 1$, investigate the classical threshold point $\sigma = 1$, and choose $\chi = 0.1$ in (a) and $\chi = 0.05$ in (b). The plots display the signal photon number as a function of time in units of the dissipation rates, while the insets show the $g^{(2)}$ function of the signal mode. The red stars in (a) show the result obtained from the numerical simulation of the full master equation (3.1), while the red line in (b) indicates its steady-state values only. The blue solid curves represent the results obtained from the numerical integration of the c-MoP eqs. (3.17), (3.18), (3.20), and (3.21). Finally, the green dashed and black dotted lines represent the time evolution obtained from a Gaussian state approximation on the c-MoP equations and the full master equation (mean-field), respectively.

can be understood as an eigenvector corresponding to the zero eigenvalue of the Liouvillian $\mathcal{L}$ such that $\mathcal{L}\rho_{ss} = 0$. The formal solution for the time evolving state which can be written as $\rho(t) = e^{\mathcal{L}t}\rho(0)$, on the other hand, involves all eigenvalues of the Liouvillian. Hence, it is a priori not clear whether a given approximate method used for the evaluation of the steady state of $\mathcal{L}$ will provide the same degree of accuracy when used for transient time evolution.

In order to investigate this open issue we simulate the time dynamics of the various approximate methods that we have introduced, and compare their results with an exact simulation of the full master equation (3.1) in regions of the parameter space where it is numerically tractable. We analyze a situation in which the input laser drives the system from the initial vacuum to its steady state. Fig. 3.6 shows the signal photon number as a function of time at the classical threshold point $\sigma = 1$, for $\gamma_p = \gamma_s = 1$, and for $\chi = 0.1$ in Fig. 3.6(a) and $\chi = 0.05$ in Fig. 3.6(b). The red stars in Fig. 3.6(a) illustrate the result obtained from the numerical simulation of the full master equation (3.1), while the red line in Fig. 3.6(b) illustrates the steady-state value of its observables only, since the small value of χ prevented us from being able to simulate the whole dynamics in this case. On the other hand, the blue solid curves represent the results obtained from the numerical integration of the c-MoP equations as explained in Sec. 3.4. Finally, the green dashed and black dotted lines represent the time evolution obtained from a GSA on the c-MoP equations and the full master equation, respectively.

Remarkably, Fig. 3.6(a) shows that the level of accuracy found dynamically for the various approximations is similar to the ones that we already encountered when evaluating steady-state quantities. In particular, it is apparent that, at any point in time, the GSA on the full master equation (mean-field) is less accurate than the GSA on the c-MoP equations, which in turn does not have the remarkable level of accuracy shown by the full c-MoP numerical simulation, almost coinciding with the numerics of the full master equation at all times. It is important to note that the evolution of the $g^{(2)}$ function shown in the inset of Fig. 3.6(a) suggests that, indeed, the c-MoP equations are able to map the full quantum state of the signal in the course of time. Thus, the c-MoP theory provides an efficient approach for the investigation of the transient time evolution in a driven-dissipative scenario, where quantum states in the intermediate time are expected to find practical applications for quantum engineering and computing [111].

A numerical simulation for the parameter set chosen in Fig. 3.6(b) demands minimal Hilbert space dimensions of $\dim \mathcal{H}_p = 6$ and $\dim \mathcal{H}_s = 120$ in order to reach convergence up to an accuracy of 10^{-2} for the relevant observables. Thus, while the c-MoP approach requires a simulation of a set of 28 814 coupled nonlinear differential equations, in the case of the full master equation one has to integrate 518 400 coupled linear differential equations, which has precluded us from being able to simulate the dynamics from it. Therefore we only show steady-state observables of the full master equation for this case.

Figs. 3.6(a) and 3.6(b) further illustrate the scaling of various quantities with the nonlinear coupling χ at the critical point. In particular, note how both the signal photon number and the time that the system needs to reach the steady state double when χ is reduced by half. The latter is known in the literature as critical slowing down [96], and just as the signal photon number, it was predicted to scale with χ^{-1} [12, 96, 99], in agreement with our c-MoP simulation. Hence, we can appreciate the practical use of a Gaussian theory by considering that to simulate an experimentally relevant scenario where $\chi \ll 1$, dynamical quantities would require extremely long simulation times. This can be efficiently handled with a GSA on the c-MoP theory, but not by a full numerical simulation. As an example, we have checked that for $\chi = 0.01$ a GSA on the c-MoP equations requires a normalized time of approximately 300 to reach the steady state, again in agreement with the χ^{-1} scaling. It can be appreciated in Fig. 3.6(a) that such time is about 10 times smaller for $\chi = 0.1$. We will exploit the ability of the Gaussian c-MoP theory to predict the scaling behaviour at threshold to a large extend in the following Chapter.

Chapter 4

Degenerate optomechanical parametric oscillators: cooling in the vicinity of a critical point

4.1 Introduction

Degenerate optical parametric oscillators (DOPOs) consist of a driven optical cavity containing a crystal with second-order optical nonlinearity [20, 42, 76, 113]. Down-conversion in the crystal can generate a field at half the frequency of the driving laser and classical electrodynamics predicts that such field will start oscillating inside the cavity only if the external laser power exceeds some threshold value, where the nonlinear gain can compensate for the cavity losses. A fully quantum-mechanical theory, on the other hand, reveals that even below threshold the down-converted field is not vacuum, but a squeezed field whose quantum correlations increase as the threshold is approached.

Recent developments in the fabrication of crystalline whispering gallery mode resonators [114–126] have opened the way to study the intracavity interplay between down-conversion and optomechanics [69], a setup that we will refer to as degenerate optomechanical parametric oscillator (DOMPO). So far, it has been shown that the presence of down-conversion in an optomechanical cavity can help enhancing mechanical cooling [127], normal mode splitting [128], sensitivity in position measurements [129], or even bringing optomechanics close to the strong coupling regime with additional bath engineering [90]. In all these works, however, the nonlinear crystal is operated as a parametric amplifier, providing a nonlinear gain to some external field that is injected in the cavity at the down-converted frequency (*stimulated* down-conversion). In contrast, the description of the interaction between the field generated via spontaneous down-conversion and the mechanical mode is much more challenging, since (below threshold) the former is purely quantum mechanical [70], so that the optomechanical coupling cannot be linearized and does not admit a simple Gaussian description.

In this thesis we provide a theory for the DOMPO which can be trusted all the way to threshold, and is obtained by combining traditional adiabatic elimination techniques with the c-MoP theory [32, 130]. We show that, for parameters compatible with current crystalline whispering gallery mode resonators, the mechanical state stays approximately thermal in all parameter space, and identify the region below threshold where the down-converted field is able to cool down the mechanical state significantly. Moreover, we provide a physical explanation for the latter, showing that it constitutes a realistic example of the "cooling by heating" mechanism [131]. Interestingly, our c-MoP approach allows us to show that cooling is not optimal at threshold, which features the largest photon number, even though the cooling rate is in fact maximal at that point. This is because the strong quantum fluctuations in the down-converted field enhance a heating mechanism associated to it, which in turn limits the mechanical cooling achievable.

The remainder of the Chapter is organized as follows. In Sec. 4.2 we introduce the DOMPO model and briefly discuss its classical properties. Next, we explain how to perform the adiabatic elimination of the optical modes in Sec. 4.3 and show that all the information about the optical modes enters the effective mechanical dynamics through the signal photon number and an optical correlation function. We then treat the optics, that is the DOPO, in different ways: via standard linearization (semi-classical approach) and also in a squeezed picture that highlights the "cooling by heating" effect in Sec. 4.4, and through the c-MoP theory in Sec. 4.5. The latter will allow us to find the scaling of the relevant quantities at threshold discussed in Sec. 4.5.1, and we will extensively use it in Sec. 4.5.2 to justify the absence of mechanical backaction on the optics by bounding the backaction terms proportioned by c-MoP theory applied to the full optomechanical problem. Finally, we will comment on the implications of alternative choices for the self-consistent Mori projector in Sec. 4.5.3.

4.2 Degenerate optomechanical parametric oscillators

Degenerate optomechanical parametric oscillators (DOMPOs) are optical resonators in which a mechanical degree of freedom is coupled to a cavity mode that is nonlinearly amplified via parametric down-conversion of an external pumping laser. We illustrate the scheme of the DOMPO system in Fig. 4.1. A crystal with second-order optical nonlinearity is shared by two cavities with relevant resonances at frequencies ω_p (pump mode) and $\omega_s \approx \omega_p/2$ (signal mode). The pump cavity is driven by a resonant laser, so that photons in the signal cavity can be generated via spontaneous down-conversion [42, 113]. In addition, one of the mirrors of the signal cavity can oscillate at frequency Ω_m, and is therefore optomechanically coupled to the down-converted field via radiation pressure [69]. In essence, the DOMPO model

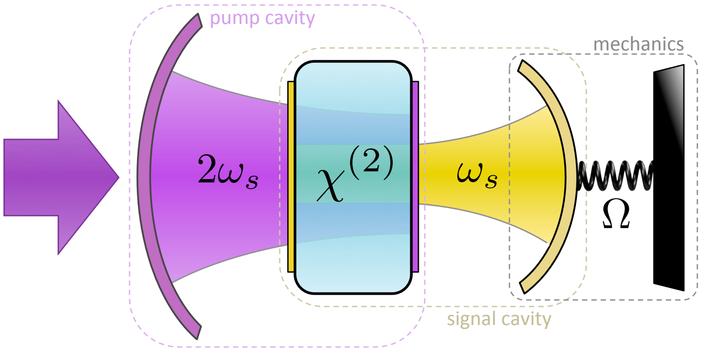

Figure 4.1: Sketch of the degenerate optomechanical parametric oscillator considered in this chapter.

is described by the DOPO model, investigated in Chapter 3 of this thesis, optomechanically coupled to a mechanical degree of freedom.

Let us define annihilation operators a_j with $j = \{p, s, m\}$ for the pump (p), signal (s), and mechanical (m) modes. Including losses of the optical modes at rate $\gamma_0 = \gamma_s = \gamma_p$ (we choose pump and signal loss rates to be equal in all that follows), as well as the irreversible energy exchange of the mechanical mode with its thermal environment at rate γ_m, the master equation governing the evolution of the full DOMPO state $\rho(t)$ can be written as ($\hbar = 1$)

$$\dot{\rho}(t) = \left(\mathcal{L}_{\mathrm{opt}} + \mathcal{L}_m + \mathcal{L}_{\mathrm{OM}}\right) \rho(t). \tag{4.1}$$

The optical Liouvillian is given by the DOPO model. In a frame rotating at the laser frequency it thus reads

$$\mathcal{L}_{\mathrm{opt}}(\cdot) = \left[-i\Delta_s a_s^\dagger a_s + \epsilon_p(a_p^\dagger - a_p) + \frac{\chi}{2}(a_p a_s^{\dagger\,2} - a_p^\dagger a_s^2), (\cdot)\right] + \gamma_0 \left(D_{a_p} + D_{a_s}\right)(\cdot), \tag{4.2}$$

where $\chi/2$ is the down-conversion rate, and ϵ_p is proportional to the square root of the injected laser power. We also remind the definition of our notation for the standard Lindblad dissipator $D_J(\cdot) = 2J(\cdot)J^\dagger - J^\dagger J(\cdot) - (\cdot)J^\dagger J$ with J being an arbitrary operator. In contrast to the DOPO model on resonance, see Eq. (3.1), we have here introduced the detuning $\Delta_s = \omega_s - \omega_L/2$ of the signal mode to half of the laser frequency, whereas we consider the pump mode to be on resonance with the laser, i.e. $\Delta_p = \omega_p - \omega_L = 0$. For the purpose of investigating optomechanical cooling effects we focus on the red detuned regime where $\Delta_s \geq 0$.

The mechanical degree of freedom is described by the local Liouvillian

$$\mathcal{L}_{\mathrm{m}}(\cdot) = -i[\Omega_m a_m^\dagger a_m, (\cdot)] + \gamma_m(\bar{n}_{\mathrm{th}} + 1)D_{a_m}(\cdot) + \gamma_m \bar{n}_{\mathrm{th}} D_{a_m^\dagger}(\cdot). \tag{4.3}$$

In the absence of light, the mechanical state is at thermal equilibrium with $\bar{n}_{\mathrm{th}}$ phonons. Finally, we write the optomechanical interaction Liouvillian as

$$\mathcal{L}_{\mathrm{OM}}(\cdot) = i[\Omega_m \eta_{\mathrm{OM}} a_s^\dagger a_s (a_m + a_m^\dagger), (\cdot)], \tag{4.4}$$

where we normalize the optomechanical coupling η_{OM} to the frequency of the mechanical oscillation Ω_m.

The Liouville-von Neumann equation of the DOMPO given by Eq. (4.1), which can be written in a short-hand notation $\dot{\rho}(t) = \mathcal{L}\rho(t)$ as in Eq. (1.1), provides the starting point for approximative theories as the nonlinear coupling terms $a_p a_s^{\dagger 2} - a_p^\dagger a_s^2$ and $a_s^\dagger a_s(a_m^\dagger + a_m)$ render an exact solution of Eq. (4.1) in general impossible. Exact numerical calculations are only feasible in the small excitation limit and therefore can not address a large range of physically interesting cases.

In the classical approximation, where any correlations between the modes are neglected and the state of all modes is assumed to be in a coherent state (as discussed in Sec. 3.2.1), one finds the classical steady-state phase diagram of the DOMPO to feature a variety of phases. All classical phases have been identified within the framework of the author's PhD thesis. We will not present a detailed discussion here and refer to Ref. [70] since we want to keep the main focus on the quantum nature of the light and the application of the c-MoP theory to the DOMPO problem. Therefore, we focus on the regime where the state of the signal field is fully quantum, i.e. where the trivial classical solution $\langle a_s \rangle = 0$ is the only stable one, henceforth referred to as the *monostable phase*, which requires two conditions. First, defining the *injection parameter* $\sigma = \epsilon_p \chi / \gamma_0^2$ and the normalized detuning $\Delta = \Delta_s/\gamma_0$, the trivial solution becomes unstable in favor of a nontrivial one $\langle a_s \rangle \neq 0$ for $\sigma > \sqrt{1+\Delta^2}$ [70]. Hence, we write $\sigma = \sqrt{1+\Delta^2}\, x$ and focus on the $x \in [0,1]$ region. The second condition, $4\Omega\Delta\eta_{\mathrm{OM}}^2/\eta_{\mathrm{DC}}^2 < 1$, guarantees that the nontrivial solution does not enter the $x \in [0,1]$ region [70]. In this expression we have introduced the dimensionless down-conversion coupling $\eta_{\mathrm{DC}} = \chi/\gamma_0$ as well as the sideband-resolution parameter $\Omega = \Omega_m/\gamma_0$.

We emphasize that the vanishing signal field amplitude excludes the possibility of using a linearization approach similar to those applied in [70, 127–129] in order to capture any optomechanical effects. The linearized equations, in fact, predict absolutely no effect from the optical modes onto the mechanical mode. By considering the vastly increasing number of signal photons in the DOPO as threshold is approached, see Sec. 3.4, one has to conclude that the linearization approach simply fails to capture any phenomena occuring below threshold. In fact, in the monostable below threshold regime, the signal photons scattered by the mechanical mode are purely quantum mechanical, with no coherent or classical background, and this is precisely what makes the optomechanical interaction $a_s^\dagger a_s(a_m^\dagger + a_m)$ purely nonlinear or nongaussian, and consequently any effect related to it is completely lost upon linearization. In the following, we provide a full quantum theory that works in all the $x \in [0,1]$ region, and use it to predict the action of the down-converted field on the mechanical state.

4.3 Adiabatic elimination of the optical modes

Despite the complexity of the DOMPO problem, we will show below that for typical system parameters the optical modes do not receive considerable backaction from the mechanics. This result is surprising since close to the critical point the DOPO experiences critical slowing down and thus one might expect the breakdown of time scale separation between the optical and mechanical modes. For now, we will simply presume the absence of backaction and leave its validation to Sec. 4.5.2 complemented by Sec. 4.5 where we exploit the c-MoP theory to gain insight in the critical behavior of the DOPO. The adiabatic elimination of the optical modes in the Born-Markov limit [4, 5, 19, 33, 132], which is a key step in our approach that can be verified using c-MoP theory, see Sec. 4.5.2, leads to an effective master equation for the reduced mechanical state $\rho_m(t)$ simplifying the problem significantly.

In order to eliminate the optical modes and find an effective master equation for the mechanical state $\rho_m(t)$ we proceed as follows. We first define the standard time-independent Mori projector $P(\cdot) = \bar{\rho}_{\text{opt}} \otimes \text{Tr}_{\text{opt}}\{\cdot\}$ whose action on the full state $\rho(t)$ of the DOMPO gives $P\rho(t) = \bar{\rho}_{\text{opt}} \otimes \rho_m(t)$. Here, $\bar{\rho}_{\text{opt}}$ is the steady state of the optical Liouvillian, that is, $\mathcal{L}_{\text{opt}}[\bar{\rho}_{\text{opt}}] = 0$. Applying this superoperator and its complement $Q = \mathbb{1} - P$ onto the master equation, and formally integrating the latter, we obtain an exact equation of motion for $\rho_m(t)$, the so-called *Nakajima-Zwanzig* equation [4, 5], see also Sec. 1.2. Such an equation is in general and especially in our case not solvable, and therefore we apply a *Born approximation* which takes all terms up to second order in the optomechanical interaction into account. The resulting equation reads

$$\begin{aligned}\dot{\rho}_m(t) = \mathcal{L}_m\rho_m(t) &+ i\Omega_m\eta_{\text{OM}}\bar{N}_s\left[x_m, \rho_m(t)\right] \\ &- \Omega_m^2\eta_{\text{OM}}^2\left[x_m, \int_0^t d\tau\, e^{\mathcal{L}_m\tau}[x_m\rho_m(t-\tau)s(\tau) - \text{H.c.}]\right],\end{aligned} \tag{4.5}$$

where we have defined the mechanical position quadrature $x_m = a_m + a_m^\dagger$, the photon number in the signal mode $\bar{N}_s = \text{Tr}\{a_s^\dagger a_s \bar{\rho}_{\text{opt}}\}$, and the optical correlation function

$$s(\tau) = \text{Tr}\{a_s^\dagger a_s e^{\mathcal{L}_{\text{opt}}\tau}[a_s^\dagger a_s \bar{\rho}_{\text{opt}}]\} - \bar{N}_s^2. \tag{4.6}$$

As we argued in Sec. 3.2.1 and in Sec. 2.2.2, the steady state $\bar{\rho}_{\text{opt}}$ of the DOPO is unique and the dynamical map $e^{\mathcal{L}_{\text{opt}}\tau}$ is a *relaxing map* [23, 63], mapping all optical operators O into the steady state while preserving the trace, that is, $\lim_{\tau\to\infty} e^{\mathcal{L}_{\text{opt}}\tau}O = \text{Tr}_{\text{opt}}\{O\}\bar{\rho}_{\text{opt}}$. Thus, the optical correlation function $s(\tau)$ will always decay to zero within some finite *memory time* which we denote by τ_{opt}. Hence, in the asymptotic limit we can write $\lim_{t\to\infty}\rho_m(t-\tau) = \lim_{t\to\infty}\rho_m(t) \equiv \bar{\rho}_m$ in the integral Kernel of Eq. (4.5), obtaining an equation for $\bar{\rho}_m$ which is quadratic in the operators a_m and therefore allows for a Gaussian-state solution. In other words, the equations for the first and second steady-state mechanical moments form a closed linear algebraic set

$$\begin{aligned}
0 &= (-i\Omega_m - \gamma_m)\langle a_m\rangle + i\Omega_m\eta_{\mathrm{OM}}\bar{N}_s - \Omega_m^2\eta_{\mathrm{OM}}^2\mathrm{Re}\{d_0\}\langle x_m\rangle \\
0 &= -\gamma_m\langle \delta a_m^\dagger \delta a_m\rangle + \gamma_m\bar{n}_{\mathrm{th}} \\
&\qquad - \Omega_m^2\eta_{\mathrm{OM}}\mathrm{Re}\{(d_+ - d_-)\langle\delta a_m^\dagger\delta a_m\rangle + (d_-^* - d_+)\langle\delta a_m^2\rangle - d_-\} \\
0 &= (-i\Omega_m - \gamma_m)\langle\delta a_m^2\rangle - \Omega_m^2\eta_{\mathrm{OM}}^2[(d_- - d_+^*)\langle\delta a_m^\dagger\delta a_m\rangle + (d_+ - d_-^*)\langle\delta a_m^2\rangle + d_-]
\end{aligned} \tag{4.7}$$

where we used the abbreviations $\langle A\rangle = \mathrm{Tr}\{A\bar{\rho}_m\}$, $\delta A = A - \langle A\rangle$, and

$$d_0 = \int_0^\infty d\tau s(\tau) \quad \text{and} \quad d_\pm = \int_0^\infty d\tau\, e^{(\pm i\Omega_m - \gamma_m)\tau}\, s(\tau). \tag{4.8}$$

These equations can be solved for the steady-state moments as functions of the optical photon number $\bar{N}_s$ and correlation function $s(\tau)$ without the need of further approximations. However, in order to obtain more physical insight into the mechanical steady state $\bar{\rho}_m$ we apply both Markov approximation and a *rotating-wave approximation* to Eq. (4.5). The Markov approximation is based on the assumption that within the optical memory time τ_{opt} all the mechanical dynamics can be neglected except for the evolution provided by the free Hamiltonian $\Omega_m a_m^\dagger a_m$. As a result we can write $e^{\mathcal{L}_m\tau}[x_m\rho_m(t-\tau)] \approx x_m(\tau)\rho_m(t)$ with $x_m(\tau) = e^{i\Omega_m\tau}a_m + e^{-i\Omega_m\tau}a_m^\dagger$. On the other hand, the rotating-wave approximation consists of neglecting all the terms proportional to a_m^2 and $a_m^{\dagger 2}$ in the effective mechanical master equation, under the assumption that their rotation at frequency $2\Omega_m$ is much larger than the rates they are weighted by. After applying these approximations in Eq. (4.5) we are left with an effective mechanical master equation given by

$$\dot{\rho}_m = \mathcal{L}_m\rho_m + i\Omega_m\eta_{\mathrm{OM}}\bar{N}_s[x_m, \rho_m] + \gamma_m\Gamma_- D_{a_m}[\rho_m] + \gamma_m\Gamma_+ D_{a_m^\dagger}[\rho_m], \tag{4.9}$$

where we have defined the heating and cooling rates $\gamma_m\Gamma_\pm = \Omega_m^2\eta_{\mathrm{OM}}^2\mathrm{Re}\{d_\mp|_{\gamma_m=0}\}$. This master equation has a very simple Gaussian steady state $\bar{\rho}_m$ corresponding to a displaced thermal state with mean

$$\langle a_m\rangle = \frac{\mathrm{i}\Omega_m\eta_{\mathrm{OM}}\bar{N}_s}{\mathrm{i}\Omega_m + \gamma_m} \approx \eta_{\mathrm{OM}}\bar{N}_s, \tag{4.10}$$

$\langle\delta a_m^2\rangle = 0$, and phonon number $\langle\delta a_m^\dagger\delta a_m\rangle = \bar{n}_m$, where $\bar{n}_m$ is given by

$$\bar{n}_m = \frac{\bar{n}_{\mathrm{th}} + \Gamma_+}{1 + (\Gamma_- - \Gamma_+)} \overset{\Gamma\gg 1}{\approx} \frac{\bar{n}_{\mathrm{th}}}{\Gamma} + \bar{n}_{\mathrm{FL}}\ . \tag{4.11}$$

Here, $\Gamma = \Gamma_- - \Gamma_+$ is the cooling efficiency and $\bar{n}_{\mathrm{FL}} = \Gamma_+/\Gamma$ the fundamental limit for the phonon number. All the information about the optical modes is contained in the heating and cooling rates $\Gamma_\pm = C\,\mathrm{Re}\,\{\gamma_0 d_\mp\}$ through the optical correlation function $s(\tau)$ and the bare cooperativity $C = \Omega Q\eta_{\mathrm{OM}}^2$ with the mechanical quality factor $Q = \Omega_m/\gamma_m$ which we here assume to fulfill $Q \gg 1$.

We note that, starting from a thermal state, the mechanical mode relaxes to its steady state with a rate $\gamma_{\text{eff}} = \gamma_m(1+\Gamma)$, since the equations of motion for the phonon number fluctuations and the mechanical field amplitude are given by

$$\partial_t \langle \delta a_m^\dagger \delta a_m \rangle = -2\gamma_m(1+\Gamma)\,\langle \delta a_m^\dagger \delta a_m \rangle + 2\gamma_m(\bar{n}_{\text{th}} + \Gamma_-), \tag{4.12a}$$

$$\partial_t \langle a_m \rangle = [-i\Omega_m - \gamma_m(1+\Gamma)]\,\langle a_m \rangle + \mathrm{i}\eta_{\text{OM}}\Omega_m \langle a_s^\dagger a_s \rangle\,. \tag{4.12b}$$

We have checked throughout all the following calculations that this rate γ_{eff} is smaller than the decay rate of the optical correlator $s(\tau)$ for the parameters of interest, hence validating the Markov approximation.

Let us remark that we have been using both Eq. (4.5) and Eq. (4.9) to obtain the steady-state moments of the mechanical oscillator. We have never observed any notable differences between them, except when working extremely close to threshold within the semi-classical approach, see the inset of Fig. 4.3. In these cases, however, the failure of Eq. (4.9) can be directly attributed to the failure of the semi-classical approach, and not to a failure of the rotating-wave approximation itself, which indeed is very well satisfied as shown by the c-MoP approach. Thus, we conclude that for the parameter regime studied in this chapter the state of the mechanical oscillator is indeed a displaced thermal state, with a phonon number that can only be evaluated once the optical photon number $\bar{N}_s$ and correlation function $s(\tau)$ are known.

In the following we study the behaviour of the steady-state phonon number as we approach the DOMPO's threshold. From Eq. (4.11) it is clear that significant cooling requires Γ to be as large as possible, but even in that case, cooling is lower bounded by $\bar{n}_{\text{FL}}$. Optimal cooling is then found by simultaneously maximizing Γ and minimizing $\bar{n}_{\text{FL}}$.

The nonlinear nature of the parametric down-conversion process in Eq. (4.2) and a potential backaction of the mechanical mode preclude an exact treatment of the optical correlation function in Eq. (4.6). To get simple analytic expressions that enable physical insight, we first apply standard linearization to the optical problem which we will denote by *semi-classical* approach. We then justify the applicability of the adiabatic elimination, resolve the unphysical predictions of the semi-classical approach close to the critical point, and find more accurate expressions at criticality by using c-MoP theory.

4.4 Semi-classical approach to the DOMPO problem

The simplest way of obtaining the optical correlator $s(\tau)$ is by using standard linearization on $\mathcal{L}_{\text{opt}}$. In this approach, we move to a displaced picture in which the large coherent background of the pump mode is removed, and then keep terms of the transformed optical Liouvillian only up to second order in the the bosonic operators, see also Sec. 3.2.1. The displacement operator $\mathcal{D} = \exp[\epsilon_p(a_p - a_p^\dagger)/\gamma_0]$ allows us to move to the new picture, in which the transformed optical state $\tilde{\rho}_{\text{opt}} = \mathcal{D}^\dagger \rho_{\text{opt}} \mathcal{D}$

evolves according to a transformed Liouvillian $\tilde{\mathcal{L}}_{\text{opt}} = \mathcal{D}^\dagger \mathcal{L}_{\text{opt}} \mathcal{D}$. Removing terms beyond quadratic order, this transformed Liouvillian can be written as a sum of independent Liouvillians for the pump and signal modes, $\tilde{\mathcal{L}}_{\text{opt}} = \mathcal{L}_p + \mathcal{L}_s$, with $\mathcal{L}_p = \gamma_0 D_{a_p}$ and

$$\gamma_0^{-1}\mathcal{L}_s(\cdot) = \left[-i\Delta a_s^\dagger a_s + \frac{\sigma}{2}(a_s^{\dagger 2} - a_s^2), (\cdot)\right] + D_{a_s}(\cdot), \tag{4.13}$$

with the injection parameter $\sigma = \epsilon_p \chi/\gamma_0^2$ and normalized detuning $\Delta = \Delta_s/\gamma_0$. Consequently, the optical steady state in the original picture becomes the separable state $\bar{\rho}_{\text{opt}} = |\epsilon_p/\gamma_0\rangle\langle\epsilon_p/\gamma_0| \otimes \bar{\rho}_s$ where $|\epsilon_p/\gamma_0\rangle$ is a coherent state of amplitude ϵ_p/γ_0 and $\bar{\rho}_s$ is the Gaussian state satisfying $\mathcal{L}_s\bar{\rho}_s = 0$. The latter is completely characterized by its first and second moments, which are trivially found to be $\langle a_s\rangle = 0$, $\langle a_s^\dagger a_s\rangle = \sigma^2/2(1+\Delta^2-\sigma^2) \equiv \bar{N}_s$, and $\langle a_s^2\rangle = \sigma(1-\mathrm{i}\Delta)/2(1+\Delta^2-\sigma^2)$, where we use the usual notation $\langle A\rangle = \mathrm{Tr}_s\{A\rho_s\}$ for any operator A acting on the signal subspace.

The optical correlation function simplifies to $s(\tau) = \mathrm{Tr}_s\{a_s^\dagger a_s e^{\mathcal{L}_s \tau}\mu_s\}$ where we have defined a traceless operator $\mu_s = (a_s^\dagger a_s - \bar{N}_s)\bar{\rho}_s$. Using again the fact that the Liouvillian $\mathcal{L}_s$ is Gaussian, it is simple to evaluate the correlation function $s(\tau)$. To this aim, we follow the steps presented in Sec. 3.3.2 and define the column vector

$$\vec{v}(\tau) = \text{col}\left(\widetilde{\langle a_s^\dagger a_s\rangle}, \widetilde{\langle a_s^2\rangle}, \widetilde{\langle a_s^{\dagger 2}\rangle}\right), \tag{4.14}$$

where the expectation value of an operator A with the tilde is defined as $\widetilde{\langle A\rangle} = \mathrm{Tr}\{Ae^{\mathcal{L}_s\tau}\mu_s\}$. Taking the derivative of this vector with respect to τ, we find the linear system $\partial_\tau \vec{v}(\tau) = L\vec{v}(\tau)$, where the matrix L reads

$$L = \gamma_0 \begin{pmatrix} -2 & \sigma & \sigma \\ 2\sigma & -2(1+i\Delta) & 0 \\ 2\sigma & 0 & -2(1-i\Delta) \end{pmatrix}. \tag{4.15}$$

It is straightforward to solve this linear system, for example by diagonalizing L. We write $L = U\Lambda U^{-1}$, with a similarity matrix U that can be found analytically (but its expression is too lengthy to be reported here), and a diagonal matrix Λ containing the eigenvalues of L, $\lambda_1 = -2\gamma_0$, and $\lambda_{2,3} = -2\gamma_0(1 \pm \mathrm{i}\sqrt{\Delta^2-\sigma^2})$. Notice that for $\sigma > \Delta$ the square root becomes imaginary, making $\lambda_2 < \gamma_0$, and in fact $\lambda_2 = 0$ at threshold, $\sigma = \sqrt{1+\Delta^2}$. Consequently, we call the region with $\sigma > \Delta$ the *critical slowing down regime*. The solution of the linear system is then found as

$$\vec{v}(\tau) = Ue^{\Lambda\tau}U^{-1}\vec{v}(0) \equiv \sum_{n=1}^{3} L_n e^{\lambda_n \tau}\,\vec{u}, \tag{4.16}$$

where we have defined the initial condition vector

$$\vec{u} = \vec{v}(0) = \text{col}\left(\langle a_s^\dagger a_s a_s^\dagger a_s\rangle - \bar{N}_s^2, \langle a_s^2 a_s^\dagger a_s\rangle - \langle a_s^2\rangle\bar{N}_s, \langle a_s^{\dagger 3} a_s\rangle - \langle a_s^2\rangle^*\bar{N}_s\right), \tag{4.17}$$

and the matrices $L_n = U\Pi_n U^{-1}$, where $(\Pi_n)_{jl} = \delta_{jn}\delta_{ln}$. Note that the vector $\vec{u}$ is formed by fourth order moments. In order to find them, we simply exploit the Gaussian structure of $\mathcal{L}_s$, which allows us to express moments of any order as products of moments of first and second order. Specifically, concerning third and fourth order moments we simply use

$$\begin{aligned} \langle a_s^\dagger a_s^2\rangle &= \langle a_s^3\rangle = 0 && (4.18a)\\ \langle a_s^{\dagger 2} a_s^2\rangle &= \langle a_s^{\dagger 2}\rangle\langle a_s^2\rangle + 2\langle a_s^\dagger a_s\rangle^2, && (4.18b)\\ \langle a_s^\dagger a_s^3\rangle &= 3\langle a_s^\dagger a_s\rangle\langle a_s^2\rangle. && (4.18c)\end{aligned}$$

Note that the optical correlation function we are looking for is given by the first component of the vector, $s(\tau) = [\vec{v}(\tau)]_1$, and the integrals appearing in d_0 and $d_\pm$ in Eq. (4.8) can be easily evaluated due to the exponential τ-dependence of $\vec{v}(\tau)$ in Eq. (4.16).

Overall, below threshold, the linearization of the DOPO is accomplished by treating the pump mode as a classical stationary source and as a result the optical problem is governed by a Gaussian single-mode Liouvillian from which any correlation function can be easily found, allowing us to obtain analytical expressions for the relevant quantities in Eq. (4.11). For the fundamental limit, we find

$$\bar{n}_{\mathrm{FL}} = \frac{4 + (\Omega - 2\Delta)^2}{8\Omega\Delta}, \tag{4.19}$$

while the cooling efficiency can be written as

$$\Gamma = Q\eta_{\mathrm{OM}}^2 \bar{N}_s(x)\Delta\, f(\Omega, \delta_{\mathrm{eff}}), \tag{4.20}$$

where we have defined the function

$$f(\Omega, \delta_{\mathrm{eff}}) = \frac{8\Omega^2[\Omega^2 + 4(5 + \delta_{\mathrm{eff}}^2)]}{(4 + \Omega^2)[\Omega^4 + 16(1 + \delta_{\mathrm{eff}}^2)^2 + 8\Omega^2(1 - \delta_{\mathrm{eff}}^2)]}, \tag{4.21}$$

and a parameter $\delta_{\mathrm{eff}} = \sqrt{\Delta^2 - \sigma^2}$ that will be shown to play the important role of an effective optical detuning. The photon number $\bar{N}_s(x) = x^2/(2 - 2x^2)$ is fully due to quantum fluctuations and increases hyperbolically until threshold $x = 1$ where it diverges in this semi-classical approach.

As explained above, optimal cooling requires the simultaneous maximization of Γ and minimization of $\bar{n}_{\mathrm{FL}}$. The fundamental limit takes its minimum value $\bar{n}_{\mathrm{FL}} = (\sqrt{4/\Omega^2 + 1} - 1)/2$ for $\Delta = \sqrt{4 + \Omega^2}/2$, and can thus be pushed towards zero by getting deeper and deeper into the resolved side-band regime $\Omega^2 \gg 4$ keeping $\Delta = \Omega/2$. On the other hand, it is easy to check by inspection that for $\Omega \gtrsim 3$, the function $f(\Omega, \delta_{\mathrm{eff}})$ requires $\delta_{\mathrm{eff}} \approx \Omega/2$ in order to take its maximum value $f \approx 1$. The optimal conditions for $\bar{n}_{\mathrm{FL}}$ and Γ are therefore incompatible and the minimum phonon number is achieved by finding a proper trade off between them.

In Fig. 4.2 we show the steady-state phonon number as a function of the two control parameters, detuning Δ and distance to threshold x, fixing the rest of parameters

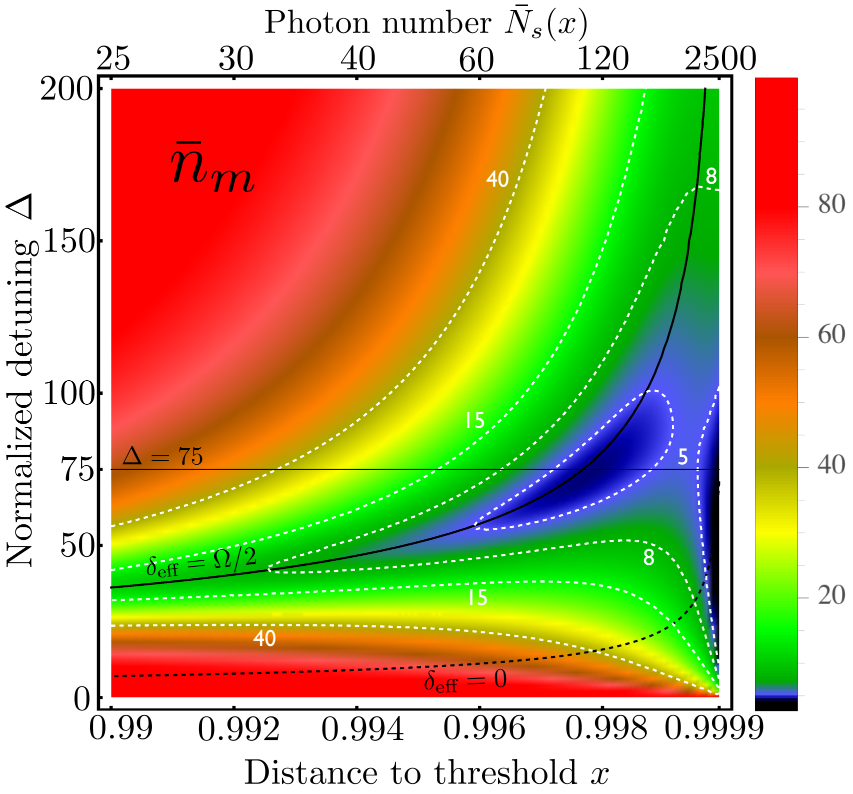

Figure 4.2: Steady state phonon number as a function of the normalized detuning Δ and the distance to threshold x, as obtained from a semi-classical description of the DOPO and a thermal phonon number $\bar{n}_{\text{th}} = 100$. We choose typical parameters for cWGM resonators [118, 119]: resolved sideband regime $\Omega = 10$, optomechanical coupling $\eta_{\text{OM}} = 10^{-4}$, mechanical quality factor $Q = 10^6$, and down-conversion coupling $\eta_{\text{DC}} = 10^{-2}$. The signal steady-state photon numbers $\bar{N}_s(x)$ corresponding to the ticked x-values are shown in the upper axis, showing that cooling is effective even with just ~ 100 photons.

to typical values of cWGM resonators [118, 119]. One can appreciate that there are two regions where significant cooling effects appear. One is in the vicinity of the threshold point and can be traced back to the vast increase of the photon number $\bar{N}_s$ which makes $\Gamma \gg 1$ for virtually any value of the rest of the parameters. However, as we will show below with the c-MoP approach, so close to threshold this semi-classical approach breaks down and hence its predictions are not reliable. Moreover, without the rotating-wave approximation, the semi-classical approach provides a divergence of the phonon number exactly at threshold (see the inset of Fig. 4.3), which can be taken as further evidence that the theory breaks down as the critical point is approached.

The other region, which turns out to be of major significance when aiming for optimal cooling, corresponds to $\delta_{\text{eff}} \approx \Omega/2$, see the black solid line in Fig. 4.2. In the next section we will use the c-MoP approach to confirm this prediction of the semi-classical theory. Moreover, this region can be understood in physical terms by moving to a new picture defined by the squeezing operator $S(r) = \exp[-\mathrm{i}r(a_s^{\dagger 2} + a_s^2)/2]$ with $\tanh 2r = \sigma/\Delta$. Note that such transformation, and hence the following physical picture, requires $\Delta > \sigma$, which corresponds in Fig. 4.2 to the region above the black dashed line. This transformation diagonalizes the Hamiltonian in the optical Liouvillian $\mathcal{L}_s$, turning it into

$$\begin{aligned}\gamma_0^{-1} S^\dagger(r)\mathcal{L}_s S(r)(\cdot) = -i[\delta_{\text{eff}} a_s^\dagger a_s, (\cdot)] + (1+\bar{N}_{\text{eff}})D_{a_s}(\cdot) + \bar{N}_{\text{eff}} D_{a_s^\dagger}(\cdot) \\ + iMK_{a_s}(\cdot) - iMK_{a_s^\dagger}(\cdot),\end{aligned} \tag{4.22}$$

where we have defined the superoperator $K_J(\cdot) = 2J(\cdot)J - J^2(\cdot) - (\cdot)J^2$, as well as the parameters $\bar{N}_{\text{eff}} = (\Delta/\delta_{\text{eff}} - 1)/2$ and $M = \sigma/2\delta_{\text{eff}}$.

Note that the $K_J(\cdot)$ terms rotate at frequency $2\delta_{\text{eff}}$, and hence are highly suppressed under a rotating wave approximation when we work within the cooling conditions $\delta_{\text{eff}} \approx \Omega/2$ away from $\delta_{\text{eff}} = 0$. Therefore, in this picture the signal field is turned into a bosonic mode oscillating at frequency δ_{eff}, coupled to a finite-temperature environment and characterized by a thermal occupation $\bar{N}_{\text{eff}}$. On the other hand, the photon number operator is transformed into

$$S^\dagger(r) a_s^\dagger a_s S(r) = \bar{N}_{\text{eff}} + (2\bar{N}_{\text{eff}} + 1) a_s^\dagger a_s + iM(a_s^2 - a_s^{\dagger}{}^2),$$

and hence the optomechanical interaction can be approximated by

$$S^\dagger(r) a_s^\dagger a_s S(r)(a_m + a_m^\dagger) \approx iM(a_s^2 a_m^\dagger - a_s^{\dagger 2} a_m). \tag{4.23}$$

within the rotating-wave approximation. Note that the optomechanical coupling is dressed by the squeezing parameter M, in a similar way to how the optomechanical interaction is dressed by the intracavity field amplitude in standard sideband cooling [33, 132]. However, at difference with that case the interaction exchanges phonons with pairs of photons (rather than single photons), thus explaining why $\gamma_0\delta_{\text{eff}} = \Omega_m/2$ is the resonance condition for cooling.

Altogether, in this semi-classical "squeezed" picture and within the rotating wave approximation we can approximate the master equation of the DOMPO by

$$\partial_t \tilde{\rho}(t) = \left(\tilde{\mathcal{L}}_{\text{s}} + \mathcal{L}_m + \tilde{\mathcal{L}}_{\text{OM}}\right) \tilde{\rho}(t) \tag{4.24}$$

with

$$\begin{aligned}
\tilde{\mathcal{L}}_{\text{s}}(\cdot) &= \left[-i\gamma_0\delta_{\text{eff}} a_s^\dagger a_s, (\cdot)\right] + \gamma_0(\bar{N}_{\text{eff}}+1)D_{a_s}(\cdot) + \gamma_0\bar{N}_{\text{eff}} D_{a_s^\dagger}(\cdot) && \text{(4.25a)}\\
\mathcal{L}_m(\cdot) &= [-i\Omega_m a_m^\dagger a_m, (\cdot)] + \gamma_m(\bar{n}_{\text{th}}+1)D_{a_m}(\cdot) + \gamma_m\bar{n}_{\text{th}} D_{a_m^\dagger}(\cdot) && \text{(4.25b)}\\
\tilde{\mathcal{L}}_{\text{OM}}(\cdot) &= [\Omega_m\eta_{\text{OM}} M(a_s^2 a_m^\dagger - a_s^{\dagger 2} a_m), (\cdot)], && \text{(4.25c)}
\end{aligned}$$

The structure of this master equation is similar to the full master equation of the DOMPO (4.1), with the differences that the optical Liouvillian is replaced by $\tilde{\mathcal{L}}_s$, corresponding to a single-mode at finite temperature, and the optomechanical interaction $a_s^\dagger a_s(a_m + a_m^\dagger)$ is replaced by $\mathrm{i}M(a_s^2 a_m^\dagger - a_s^{\dagger 2} a_m)$. The adiabatic elimination of the optical mode can be carried out exactly in the same way as we did in Sec. 4.3, and under the cooling condition $\delta_{\rm eff} = \Omega/2$ it would lead to the heating and cooling rates

$$\Gamma_- \approx \frac{1}{2} C M^2 \mathrm{Tr}\{a_s^2 a_s^{\dagger 2} \tilde{\rho}_s\}, \tag{4.26a}$$

$$\Gamma_+ \approx \frac{1}{2} C M^2 \mathrm{Tr}\{a_s^{\dagger 2} a_s^2 \tilde{\rho}_s\}, \tag{4.26b}$$

where $C = \Omega_m^2 \eta_{\rm OM}^2/\gamma_m \gamma_0$ is the bare optomechanical cooperativity, and $\tilde{\rho}_s$ is a thermal state with mean photon number $\bar{N}_{\rm eff}$. The cooling efficiency is then given by

$$\Gamma = \Gamma_- - \Gamma_+ = \frac{1}{2} C M^2 \mathrm{Tr}\{[a_s^2, a_s^{\dagger 2}]\tilde{\rho}_s\} = 2CM^2(\bar{N}_{\rm eff} + 1/2). \tag{4.27}$$

The cooling efficiency Γ thus receives an additional contribution $2\bar{N}_{\rm eff}$ from the effective thermal photon number, which is a direct consequence of the nonlinear nature of the effective optomechanical coupling (4.23) that cannot be found in standard sideband cooling.

This represents a natural example of the so-called *cooling by heating* effect [131], where heating up the optical field can contribute to making optomechanical cooling more efficient. It is important to note that this enhancement of the cooling efficiency is a direct consequence of the commutator appearing in the trace, contributing as $[a_s^2, a_s^{\dagger 2}] = 4a_s^\dagger a_s + 2$, which in turn comes from the fact that the effective optomechanical interaction $i(a_s^2 a_m^\dagger - a_s^{\dagger 2} a_m)$ corresponds to the exchange of phonons with pairs of photons. In the usual sideband laser cooling scenario, the effective optomechanical interaction is bilinear, e.g. $i(a_s a_m^\dagger - a_s^\dagger a_m)$, meaning that the commutator in the expression above is replaced by $[a_s, a_s^\dagger] = 1$, and hence the thermal photonic background does not enter the cooling efficiency.

Let us finally note that the fundamental limit can be written as

$$\bar{n}_{\rm FL} = \frac{\Gamma_+}{\Gamma} = \frac{\mathrm{Tr}\{a_s^{\dagger 2} a_s^2 \tilde{\rho}_s\}}{\mathrm{Tr}\{[a_s^2, a_s^{\dagger 2}]\tilde{\rho}_s\}} = \frac{\bar{N}_{\rm eff}^2}{2\bar{N}_{\rm eff} + 1} \xrightarrow{\bar{N}_{\rm eff} \gg 1} \frac{\bar{N}_{\rm eff}}{2}, \tag{4.28}$$

which increases linearly with the effective thermal photon number. When the term $\bar{n}_{\rm th}/\Gamma$ dominates over $\bar{n}_{\rm FL}$ in Eq. (4.11) the thermal optical background $\bar{N}_{\rm eff}$ can then be interpreted as "good noise", while as soon as the phonon limit is reached it becomes "bad noise" which just heats up the mechanical motion. This can be appreciated by following the $\delta_{\rm eff} = \Omega/2$ curve in Fig. 4.2. Hence, the "cooling by heating" mechanism is optimized by finding a proper trade off between the increase in the cooling efficiency ("good noise") and the increase in the fundamental limit ("bad noise"). It is to be noted that within the usual sideband laser cooling, any thermal background will still contribute to this fundamental limit, $\bar{n}_{\rm FL} = \mathrm{Tr}\{a_s^\dagger a_s \rho_s\}/\mathrm{Tr}\{[a_s, a_s^\dagger]\rho_s\} \xrightarrow{\bar{N}_{\rm eff} \gg 1} \bar{N}_{\rm eff}$, but, as explained above, it provides no enhancement of the cooling efficiency Γ. In other words, in standard sideband cooling the thermal background acts only as "bad" noise.

We emphasize that the expressions for Γ in Eq. (4.27) and $\bar{n}_{\mathrm{FL}}$ in Eq. (4.28) agree with the ones provided in Eqs. (4.20) and (4.19), respectively, which have been first calculated exactly within the semi-classical approach, and then approximated to leading order in $1/\Omega^2$ for $\delta_{\mathrm{eff}} = \Omega/2$.

4.5 Quantum approach to the DOMPO problem

The semi-classical approach has allowed us to get analytical and physical insight into the DOMPO problem. It is however well known that this approximation fails close to the critical point. To determine where it exactly breaks down and to find more accurate results for those parameters, we make use of the c-MoP technique which we developed for the DOPO in Chapter 3 and in particular of the Gaussian c-MoP theory presented in Sec. 3.6. For parameters of our interest within this thesis, which are compatible with cWGM resonators, the theory is already regularized by using c-MoP only in the optical problem of the DOPO which provides a more accurate description for the optical correlation function (4.6) and photon number that enter the effective mechanical dynamics and steady state through Eq. (4.9).

We will discuss the technical steps of the c-MoP theory and some important predictions about the critical behavior of the DOMPO in more detail below, but for now we show a very representative case for the phonon number $\bar{n}_m$ as a function of the distance to threshold x in Fig. 4.3. The c-MoP results find perfect agreement with the semi-classical predictions for almost all values of x, thus verifying the "cooling by heating" effect presented above. Most importantly, we find that the absolute minimum phonon number is indeed reached when the resonance condition $\delta_{\mathrm{eff}} = \Omega/2$ is met. On the other hand, close to threshold we find a significant correction to the semi-classical predictions for the fundamental limit $\bar{n}_{\mathrm{FL}}$. In particular, while this is independent of the distance to threshold x in the semi-classical picture, c-MoP shows that it actually increases very rapidly as the critical point is approached, and hence no cooling is found no matter how much the efficiency Γ is increased. This is consistent with the fact that when $\Delta < \sigma$ (as happens at threshold upon entering the critical slowing-down regime), δ_{eff} becomes imaginary and cannot be used to bring the optomechanical interaction to resonance.

Let us now turn to a few technical details which are different from the detailed description of the c-MoP approach to the DOPO problem presented in Chapter 3. Our main goal consists in finding the optical correlation function $s(\tau)$ defined in Eq (4.6). We start by noting that we can rewrite it as

$$s(\tau) = \bar{N}_s \left(\mathrm{Tr}\{a_s^\dagger a_s \nu(\tau)\} - \bar{N}_s \right) \tag{4.29}$$

where $\nu(\tau) = e^{\mathcal{L}_{\mathrm{opt}}\tau}\nu(0)$ can be interpreted as an operator with evolution equation $\dot{\nu} = \mathcal{L}_{\mathrm{opt}}\nu$ and initial condition $\nu(0) = a_s^\dagger a_s \bar{\rho}_{\mathrm{opt}}/\bar{N}_s$. We find $\mathrm{Tr}\{\nu(\tau)\} = 1$ for all

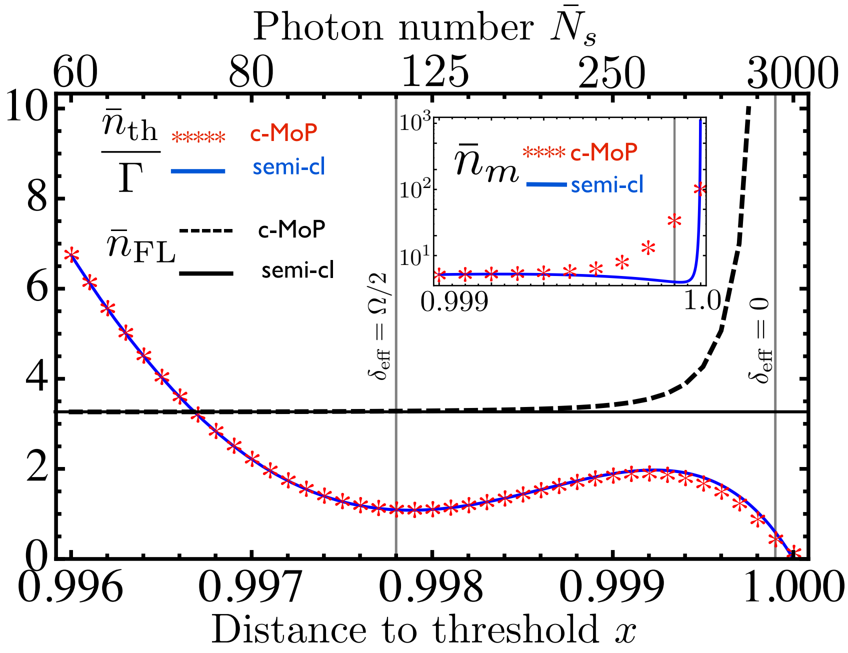

Figure 4.3: Terms $\bar{n}_{\text{th}}/\Gamma$ and $\bar{n}_{\text{FL}}$ contributing to the steady-state phonon number (4.11) as a function of the distance to threshold parameter x. We fix the detuning to $\Delta = 75$ choosing the rest of parameters as in Fig. 4.2. The inset displays a close up of the steady-state phonon number $\bar{n}_m$ for $x \in [0.999, 1]$, but without applying the rotating-wave and Markov approximations on the level of the mechanical master equation (4.5). Note that c-MoP gives finite results equivalent to those found within the rotating-wave approximation, while the semi-classical predictions diverge at threshold, which can be taken as further evidence that the theory breaks down there. The upper axis shows the signal photon numbers $\bar{N}_s$ corresponding to the ticked x-values as obtained from c-MoP up to threshold for $x = 1$.

times since the dynamical map $e^{\mathcal{L}_{\text{opt}}t}$ is trace preserving. This evolution equation is formally equivalent to the optical master equation (3.1) of the DOPO with an additional signal detuning term. Thus, we can apply c-MoP theory directly on $\nu(t)$, with the reduced matrices $\nu_p(t) = \text{Tr}_s\{\nu(t)\}$ and $\nu_s(t) = \text{Tr}_p\{\nu(t)\}$ evolving according to equations (3.17), (3.18), (3.20) and (3.21) with ρ_j replaced by ν_j and the additional signal detuning term in $\mathcal{L}_s$. Under a Gaussian approximation for $\nu_s(t)$ similar to (4.18) but with expectation values defined with respect to $\nu_s(t)$, the evolution equations for the first and second moments of $\nu_s(t)$, $\nu_p(t)$, $h_s(t)$, $\{h_{p,n}(t)\}_{n=1,2,3}$, and their Hermitian conjugates (note that ν is not Hermitian) form a closed nonlinear system which we can solve again efficiently. Note that the initial conditions for these moments, e.g., $\text{Tr}\{a_s^\dagger a_s \nu(0)\} = \text{Tr}\{a_s^\dagger a_s a_s^\dagger a_s \bar{\rho}_{\text{opt}}\}/\bar{N}_s$, are found from the Gaussian c-MoP steady-state solutions as explained above.

We emphasize that the results presented here are expected to be highly accurate based on our findings with respect to the quantitative accuracy of the Gaussian c-MoP approach. Given the assumption of the time-scale separation between optics and mechanics to hold (for which we present strong arguments in Sec. 4.5.1 and 4.5.2), the effective master equation of the mechanics can be expected to be very precise or even quasi exact for local mechanical quantities. Thus the only remaining quantity which does not allow for a direct analytic description is the optical correlation function $s(\tau)$ defined in Eq. (4.6) as the DOPO problem is a nonlinear two-mode problem with no analytic solution. Furthermore, a direct numerical simulation becomes unfeasible for moderate photon numbers ~ 100 already. In contrast the Gaussian c-MoP theory is highly efficient and still very accurate especially below and at threshold for all local first or second order moments of the optical fields for both dynamics and the steady state as shown in Figs. 3.5, 3.5 and 3.6. And indeed, the optical correlation function can be written as a second order moment of the signal field with respect to the regression matrix $\nu(\tau)$.

4.5.1 Critical scaling behavior

The knowledge of the scaling behavior of certain observables plays an important role for the determination of the conditions under which mechanical backaction on the optics can be neglected. In particular, we will be interested in the scaling of the signal photon number and the decay rate of the optical correlation function $s(\tau)$ at the critical point. In Sec. 3.7 we have indicated that the Gaussian c-MoP theory finds a scaling for the signal photon number for zero signal detuning which agrees with the well-known η_{DC}^{-1} scaling with the down-conversion coupling [12, 39, 96, 99]. Thus, we expect the scaling predictions presented here to be very reliable.

In Fig. 4.4(a) we show the steady-state signal photon number $\bar{N}_s$ at the critical point ($x = 1$) as a function of the normalized detuning Δ. It shows a clear linear dependence for $\Delta > 1$ which, together with the well-known η_{DC}^{-1} scaling with the down-conversion coupling, provides an overall $\bar{N}_s \propto (1 + \Delta)/\eta_{\mathrm{DC}}$ scaling of the signal photon number at threshold.

In Fig.4.4(b) we show the evolution of the absolute value of the correlation function $s(\tau)$ at the critical point and for different values of the normalized detuning Δ. Time is normalized to $[\gamma_0\eta_{\mathrm{DC}}(1+\Delta)]^{-1}$, and hence the fact that all the curves decay on the same-time scale proves that the optical relaxation time scales as $\gamma_{\mathrm{opt}} = \gamma_0\eta_{\mathrm{DC}}(1+\Delta)$ at threshold. This again plays a fundamental role when proving that mechanical backaction is negligible, as we pass to explain now in detail.

4.5.2 The Absence of mechanical backaction

The adiabatic elimination of the optical fields relies on the time-scale separation between the optical and mechanical degrees of freedom. In particular, such an approach neglects mechanical backaction onto the optics, which is a good approximation as long as the rate of any mechanical perturbation is much smaller than the intrinsic relaxation rate of the optics γ_{opt}, see also the general arguments presented

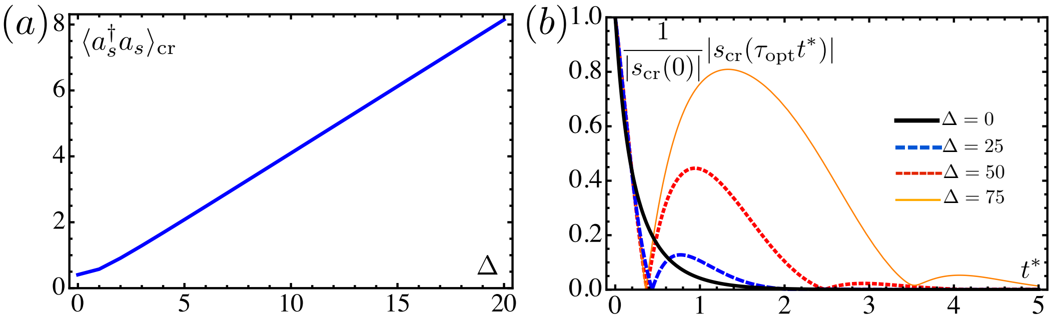

Figure 4.4: (a) Steady state photon number $\bar{N}_s = \text{Tr}\{a_s^\dagger a_s \bar{\rho}_{\rm opt}\}$ at the critical point as a function of the normalized detuning Δ. (b) Absolute value of the normalized optical correlation function $s(\tau)$ at the critical point for different values of detuning as of function of the normalized time $\gamma_{\rm opt}\tau$, with $\gamma_{\rm opt} = \gamma_0 \eta_{\rm DC}(1+\Delta)$. In both figures the parameters are $\gamma_0 = 1$ and $\eta_{\rm DC} = 0.01$, and we have obtained them by applying Gaussian c-MoP theory to the optical problem.

in Sec. 1.2. Far from the critical point the optical relaxation rate is γ_0, which usually dominates over any other rate in the system. However, as the critical point is approached the DOPO dynamics exhibits a critical slowing down, and its relaxation rate decreases with the distance to threshold. Hence, in our work that considers parameters close to threshold, it is important to verify that the desired time-scale separation is present.

As explained in the general case in Sec. 1.2 we can provide an intuitive argument which follows from relating the mechanical backaction rate with the optical frequency-shift induced by the optomechanical interaction, $\gamma_{\rm back} = \eta_{\rm OM}\Omega_m\langle x_m\rangle = 2\eta_{\rm OM}^2\Omega_m\bar{N}_s$, where we have used (4.10). Hence, using the scaling of $\bar{N}_s$ and $\gamma_{\rm opt}$ obtained in the previous section at threshold, the condition $\gamma_{\rm back} \ll \gamma_{\rm opt}$ becomes $2\Omega(\eta_{\rm OM}/\eta_{\rm DC})^2 \ll 1$, which is very well satisfied for the parameters of our study. Moreover, note that this condition is automatically satisfied when working within the monostability condition $4\Delta\Omega(\eta_{\rm OM}/\eta_{\rm DC})^2 < 1$ and $\Delta \gg 1/2$.

We can set more rigorous bounds to the region where mechanical backaction is negligible by using c-MoP theory. In contrast to adiabatic elimination methods, c-MoP does not rely on the concept of time-scale separation or absence of backaction effects. Hence, we apply it to the DOMPO system by using the time-dependent self-consistent Mori projectors $\mathcal{P}_t^{\rm opt} = \rho_{\rm opt}(t)\otimes\text{Tr}_{\rm opt}\{\cdot\}$ and $\mathcal{P}_t^m = \text{Tr}_m\{\cdot\}\otimes\rho_m(t)$, that is, using a bipartition "optics $\otimes$ mechanics" for the system. This approach will allow us to identify the terms contributing to the mechanical backaction and find upper bounds to their scaling. Using the general form given by Eq. (1.34) for the DOMPO setup in Eq. (4.1), the c-MoP equations for the reduced optical and mechanical states in the asymptotic $t\to\infty$ or steady-state limit are easily found to read for the mechanics

$$\begin{aligned}\frac{d\bar{\rho}_m}{dt} = 0 = \mathcal{L}_m\bar{\rho}_m + &i\Omega_m\eta_{\mathrm{OM}}\langle a_s^\dagger a_s\rangle[x_m,\bar{\rho}_m] \\ &- \Omega_m^2\eta_{\mathrm{OM}}^2\left[x_m, \int_0^\infty d\tau\, e^{\mathcal{L}_m\tau}(\delta x_m\bar{\rho}_m s(\tau) - \mathrm{H.c.})\right],\end{aligned} \tag{4.30}$$

and for the optics

$$\begin{aligned}\frac{d\bar{\rho}_{\mathrm{opt}}}{dt} = 0 = \mathcal{L}_{\mathrm{opt}}\bar{\rho}_{\mathrm{opt}} + &i\Omega_m\eta_{\mathrm{OM}}\langle x_m\rangle[a_s^\dagger a_s,\bar{\rho}_{\mathrm{opt}}] \\ &- \Omega_m^2\eta_{\mathrm{OM}}^2\left[a_s^\dagger a_s, \int_0^\infty d\tau\, e^{\mathcal{L}_{\mathrm{opt}}\tau}(\delta n_s\bar{\rho}_{\mathrm{opt}}\, s_m(\tau) - \mathrm{H.c.})\right],\end{aligned} \tag{4.31}$$

where, for any operator A, we have introduced the usual definition $\delta A = A - \langle A\rangle$, while $\delta n_s = a_s^\dagger a_s - \langle a_s^\dagger a_s\rangle$. $s(\tau)$ is the usual optical correlation function (4.6), and we have defined the mechanical correlation function

$$\begin{aligned}s_m(\tau) &= \mathrm{Tr}_m\{x_m e^{\mathcal{L}_m\tau}\delta x_m\bar{\rho}_m\} \\ &= e^{(-\mathrm{i}\Omega_m-\gamma_m)\tau} + \left[e^{(-\mathrm{i}\Omega_m-\gamma_m)\tau}(\langle\delta a_m^\dagger\delta a_m\rangle + \langle\delta a_m^2\rangle) + \mathrm{c.c.}\right],\end{aligned} \tag{4.32}$$

where the final expression is easily found since $\mathcal{L}_m$ is quadratic. Note that the only difference between the c-MoP Eq. (4.30) for the mechanical state and (4.5) in the stationary limit is the appearance of the fluctuation operator δx_m in the integral kernels, which is a direct consequence of the time-dependence in the self-consistent Mori projector. Nevertheless, this difference is not of major importance since the equations of motion for the fluctuations of the mechanical state $\langle\delta a_m^\dagger\delta a_m\rangle$ and $\langle\delta a_m^2\rangle$ obtained from these equations are equivalent.

The last two terms on the right-hand side of Eq. (4.31) account for the mechanical backaction on the optics, and we proceed now to bound their effect. The second to last term describes precisely the optical detuning $\Omega_m\eta_{\mathrm{OM}}\langle x_m\rangle$ induced by the optomechanical interaction that we already discussed at the beginning of the section, concluding that it is negligible within the parameter regime we work with. Then we focus on the last term in Eq. (4.31), the Born term. For this purpose we derive the steady-state equation for the moment $\langle a_s^{\dagger 2}\rangle$ which completely suffices within the Gaussian c-MoP theory as $\langle a_s^2\rangle = \langle a_s^{\dagger 2}\rangle^*$ and since the Born term does not effect the signal photon number. It reads

$$\begin{aligned}0 = \mathrm{Tr}_{\mathrm{opt}}\{a_s^{\dagger 2}\mathcal{L}_{\mathrm{opt}}\bar{\rho}_{\mathrm{opt}}\} &- 2\mathrm{i}\Omega_m\eta_{\mathrm{OM}}\langle x_m\rangle\langle a_s^{\dagger 2}\rangle \\ &+ 2\Omega_m^2\eta_{\mathrm{OM}}^2\int_0^\infty d\tau\,\mathrm{Re}\{s_m(\tau)\}\,\mathrm{Tr}_{\mathrm{opt}}\left\{a_s^{\dagger 2}e^{\mathcal{L}_{\mathrm{opt}}\tau}[a_s^\dagger a_s,\bar{\rho}_{\mathrm{opt}}]\right\} \\ &+ 2\mathrm{i}\Omega_m^2\eta_{\mathrm{OM}}^2\int_0^\infty d\tau\,\mathrm{Im}\{s_m(\tau)\}\,\mathrm{Tr}_{\mathrm{opt}}\left\{a_s^{\dagger 2}e^{\mathcal{L}_{\mathrm{opt}}\tau}\{\delta n_s,\bar{\rho}_{\mathrm{opt}}\}\right\},\end{aligned} \tag{4.33}$$

where $\{\cdot,\cdot\}$ denotes the anticommutator. Note first that the correlation functions $\mathrm{Tr}_{\mathrm{opt}}\left\{a_s^{\dagger 2}e^{\mathcal{L}_{\mathrm{opt}}\tau}[a_s^\dagger a_s,\bar{\rho}_{\mathrm{opt}}]\right\}$ and $\mathrm{Tr}_{\mathrm{opt}}\left\{a_s^{\dagger 2}e^{\mathcal{L}_{\mathrm{opt}}\tau}\{\delta n_s,\bar{\rho}_{\mathrm{opt}}\}\right\}$, which are of similar structure as the optical correlation function $s(\tau)$, decay to zero at a rate γ_{opt}. Next, we derive upper bounds for the last two terms in Eq. (4.33). For the second to last term we find

$$\begin{aligned}
&\left|2\Omega_m^2\eta_{\mathrm{OM}}^2\int_0^\infty d\tau\ \ \mathrm{Re}\{s_m(\tau)\}\,\mathrm{Tr}_{\mathrm{opt}}\left\{a_s^{\dagger 2}e^{\mathcal{L}_{\mathrm{opt}}\tau}[a_s^\dagger a_s,\bar{\rho}_{\mathrm{opt}}]\right\}\right|\\
&\qquad\le\left|2\Omega_m^2\eta_{\mathrm{OM}}^2\frac{\mathrm{Re}\{s_m(0)\}\,\mathrm{Tr}_{\mathrm{opt}}\left\{a_s^{\dagger 2}e^{\mathcal{L}_{\mathrm{opt}}0}[a_s^\dagger a_s,\bar{\rho}_{\mathrm{opt}}]\right\}}{\gamma_m+\gamma_{\mathrm{opt}}}\right|\\
&\qquad\le\underbrace{\frac{4\Omega_m^2\eta_{\mathrm{OM}}^2\bar{n}_m}{\gamma_m+\gamma_{\mathrm{opt}}}}_{\gamma'_{\mathrm{back}}}|\langle a_s^{\dagger 2}\rangle|,
\end{aligned}\tag{4.34}$$

where in the last step we have used $s_m(0)=1+\langle\delta a_m^\dagger\delta a_m\rangle+\langle\delta a_m^2\rangle\approx\langle\delta a_m^\dagger\delta a_m\rangle\equiv\bar{n}_m$ (note that we expect the mechanical state to stay approximately thermal, and hence $\langle\delta a_m^2\rangle\approx 0$) and $\mathrm{Tr}_{\mathrm{opt}}\left\{a_s^{\dagger 2}[a_s^\dagger a_s,\bar{\rho}_{\mathrm{opt}}]\right\}=\langle[a_s^{\dagger 2},a_s^\dagger a_s]\rangle=2\langle a_s^{\dagger 2}\rangle$. Similarly, for the last term in Eq. (4.33) we find

$$\begin{aligned}
&\left|2\mathrm{i}\Omega_m^2\eta_{\mathrm{OM}}^2\int_0^\infty d\tau\ \ \mathrm{Im}\{s_m(\tau)\}\,\mathrm{Tr}_{\mathrm{opt}}\left\{a_s^{\dagger 2}e^{\mathcal{L}_{\mathrm{opt}}\tau}\{\delta n_s,\bar{\rho}_{\mathrm{opt}}\}\right\}\right|\\
&\qquad\le\left|2\Omega_m^2\eta_{\mathrm{OM}}^2\frac{\mathrm{Tr}_{\mathrm{opt}}\left\{a_s^{\dagger 2}e^{\mathcal{L}_{\mathrm{opt}}0}\{\delta n_s,\bar{\rho}_{\mathrm{opt}}\}\right\}}{\gamma_m+\gamma_{\mathrm{opt}}}\right|\\
&\qquad\le\frac{2\Omega_m^2\eta_{\mathrm{OM}}^2}{\gamma_m+\gamma_{\mathrm{opt}}}\left|\mathrm{Tr}_{\mathrm{opt}}\left\{a_s^{\dagger 2}\{\delta n_s,\bar{\rho}_{\mathrm{opt}}\}\right\}\right|\\
&\qquad\approx\underbrace{\frac{4\Omega_m^2\eta_{\mathrm{OM}}^2(2\bar{N}_s+1)}{\gamma_m+\gamma_{\mathrm{opt}}}}_{\gamma''_{\mathrm{back}}}|\langle a_s^{\dagger 2}\rangle|.
\end{aligned}\tag{4.35}$$

where for the last expression we have used $\mathrm{Tr}_{\mathrm{opt}}\left\{a_s^{\dagger 2}\{\delta n_s,\bar{\rho}_{\mathrm{opt}}\}\right\}=2(\langle a_s^{\dagger 3}a_s\rangle-\langle a_s^{\dagger 2}\rangle\langle a_s^\dagger a_s\rangle+\langle a_s^{\dagger 2}\rangle)\approx 2(2\bar{N}_s+1)\langle a_s^{\dagger 2}\rangle$, within the Gaussian state approximation (4.18), that is, $\langle a_s^{\dagger 3}a_s\rangle\approx 3\langle a_s^{\dagger 2}\rangle\langle a_s^\dagger a_s\rangle$, noting that $\langle a_s\rangle=0$ below threshold.

A sufficient condition for mechanical backaction to be negligible is then $\gamma'_{\mathrm{back}},\gamma''_{\mathrm{back}}\ll\gamma_{\mathrm{opt}}$. We pass to check whether this is the case in our work. Note first that $\gamma_m\ll\gamma_{\mathrm{opt}}$ even at threshold, since $\gamma_{\mathrm{opt}}/\gamma_m\sim\gamma_s\eta_{\mathrm{DC}}(1+\Delta)/\gamma_m\gg 1$ for the parameters we are interested in. Using the scalings $\gamma_{\mathrm{opt}}\propto\gamma_0\eta_{\mathrm{DC}}(1+\Delta)$ and $\bar{N}_s\propto(1+\Delta)/\eta_{\mathrm{OM}}$ at threshold (where these bounds are the tightest), we can then write the conditions under which backaction is negligible as $\gamma'_{\mathrm{back}}/\gamma_{\mathrm{opt}}\sim\Omega^2\bar{n}_m\eta_{\mathrm{OM}}^2/\eta_{\mathrm{DC}}^2(1+\Delta)^2\ll 1$ and $\gamma''_{\mathrm{back}}/\gamma_{\mathrm{opt}}\sim\Omega^2\eta_{\mathrm{OM}}^2/\eta_{\mathrm{DC}}^3(1+\Delta)\ll 1$. For the parameter set of Fig. 2 these lead to the conditions $\bar{n}_m\ll 100(1+\Delta)^2$ and $1+\Delta\gg 1$, respectively. For the large values of Δ that we use during most of our study, these conditions are very well satisfied. For small Δ they seem to be too tight, but we need to stress here that we have been extremely conservative when estimating the Born terms (4.34) and (4.35), meaning that in practice backaction should be negligible even in a much broader region of the parameter space.

4.5.3 Signal-pump correlations and tripartite c-MoP theory

Finally, we would like to discuss the "tripartite" c-MoP theory which we have also employed to the DOMPO problem. In the tripartite c-MoP theory we use a projector which projects onto the factorized state $\rho_p(t) \otimes \rho_s(t) \otimes \rho_m(t)$ of pump, signal and mechanical mode. Due to the absence of a pump-mechanics interaction, the resulting c-MoP equations are given by the DOPO equations presented in Sec. 3.3 and Sec. 3.3.2 for the dynamics of $\rho_p(t)$ and $\rho_s(t)$ together with Eq. (4.31) accounting for the backaction of the mechanics onto the signal, while the equation for the dynamics of $\rho_m(t)$ is given by Eq. (4.30). The significant difference within the tripartite theory, however, is revealed in the optical Liouvillian $\mathcal{L}_{\text{opt}}$ which in Eq. (4.31) and most importantly in the optical correlation function $s(\tau)$, see Eq. (4.6), is replaced by $\mathcal{L}_s$ as given in Eq. (3.4).

The results obtained from a tripartite c-MoP theory coincide well with the c-MoP results presented in Sec. 4.5 up to a point, which is usually very close to threshold, where they lead to unphysical predictions such as negative phonon numbers. We conclude from this observation that the signal-pump correlations, included in the bipartite c-MoP theory of Sec. 4.5 but neglected in the tripartite theory, during the memory or rather correlation time of optics and mechanics indeed play an important role for the behavior of the mechanical mode.

Chapter 5

The nonequilibrium Dicke model

In the last chapter of the work we will present valuable insights for the c-MoP theory obtained from an investigation of the nonequilibrium Dicke model [38, 91, 133]. The Dicke model is of interest for us since on the one hand it offers an "impurity many-body" problem which allows for the investigation of different Ansatzes for c-MoP projectors. On the other hand, we find the physics of the Dicke model to be very much related to the one of the DOPO and thus it allows us to exploit the methods and concepts investigated in detail in Chapter 3. The results presented here are not fully elaborated and therefore should be understood as an outlook on what can be done in future work.

The nonequilibrium Dicke model (NEDM) describes the interaction of a photonic mode subject to Markovian dissipation with an ensemble of N two-level atoms. We shall denote the creation and annihilation operators of the photonic mode by a and $a^\dagger$, respectively. These operators fulfill the bosonic commutation relations $[a, a^\dagger] = \mathbb{1}$. The atoms shall be described by the Pauli operators σ_i^z, σ_i^x and the (de)excitation operators (σ_i) $\sigma_i^\dagger$ for $i \in \{1, 2, ..., N\}$. Finally, by introducing the collective spin operators $J_z = \frac{1}{2}\sum_{i=1}^N \sigma_i^z$, $J = \sum_{i=1}^N \sigma_i$ and $J_x = J + J^\dagger$ we state the NEDM ($\hbar = 1$)

$$\partial_t \rho(t) = -i\left[\omega_0 a^\dagger a + \omega_z J_z + \frac{g}{\sqrt{N}} x_a J_x, \rho(t)\right] + \kappa D_a \rho(t), \tag{5.1}$$

where we have introduced the quadrature $x_a = a + a^\dagger$, the standard Lindblad dissipator $D_J(\cdot) = 2a(\cdot)a^\dagger - a^\dagger a(\cdot) - (\cdot)a^\dagger a$, the local mode energies ω_0 and ω_z for the photons and atoms, respectively, and the coupling rate g. The total angular momentum $J_{\text{tot}}^2 = J_z^2 + (JJ^\dagger + J^\dagger J)/2$ is conserved by Eq. (5.1) [38] and thus we introduce a boundary condition complementing Eq. (5.1) by

$$\langle J_z^2 \rangle + \frac{1}{2}\left(\langle J^\dagger J \rangle + \langle J J^\dagger \rangle\right) = \langle (\vec{J}_{\text{tot}})^2 \rangle = \frac{N^2}{4}, \tag{5.2}$$

where the last equality is true for any initial state in which all atoms are in their ground state.

5.1 Mean-field approximation for the nonequilibrium Dicke model

In all what follows we will be interested in the stationary state $\partial_t \rho(t) = 0$ of Eq. (5.1). The nonlinear nature of the atom operators precludes an exact solution in general. We focus on the ultra-strong coupling regime $g \approx \omega_0(\omega_z)$ such that the counter-rotating terms aJ and $a^\dagger J^\dagger$ can not be neglected under a rotating-wave approximation. In fact, the counter-rotating terms will drive the system through a dissipative second order phase transition from a normal phase with $\langle a \rangle = 0$ to a superradiant phase with $\langle a \rangle \neq 0$ [20, 38]. The phases need to be understood as steady-state phases and they are characterized by exploiting a semi-classical or rather mean-field analysis.

As shown throughout the thesis the mean-field equations can be obtained by the c-MoP equations up to first order in $g/\sqrt{N}$. Thus, we refer to reference [38] for a detailed analysis of the mean-field approach for the treatment of the NEDM. We, however, state the mean-field equation here for completeness. By inserting the product state Ansatz $\rho(t) = \rho_{ph}(t) \otimes \rho_{at}(t)$, with $\rho_{ph}(t)$ $(\rho_{at}(t))$ describing the reduced state of the photons (atoms), into Eq. (5.1) one obtains the coupled nonlinear mean-field equations by tracing out the atoms in one case and the photons in the other case. The mean-field equations read

$$\begin{aligned} \partial_t \rho_{at}(t) &= -i \left[\omega_z J_z + \frac{g}{\sqrt{N}} \operatorname{Tr}_{ph}\{x_a \rho_{ph}(t)\}\, J_x, \rho_{at}(t) \right] \\ \partial_t \rho_{ph}(t) &= -i \left[\omega_0 a^\dagger a + \frac{g}{\sqrt{N}} \operatorname{Tr}_{at}\{J_x \rho_{at}(t)\}\, x_a, \rho_{ph}(t) \right] + \kappa D_a \rho_{ph}(t)\,. \end{aligned} \tag{5.3}$$

The superradient phase corresponds to the symmetry-broken solution branch of the mean-field equations since the NEDM is invariant under the Z_2 transformation which transforms $a \to -a$ and $J \to -J$. We illustrate the scaled stationary state photon number $\langle a^\dagger a \rangle_{ss}/N$ and the occupation number of a single atom $\langle \sigma^\dagger \sigma \rangle_{ss}$ (where we dropped the index i due to symmetry reasons) obtained by mean-field theory in Fig. 5.1 (a) and (b) by the dashed-gray line, respectively, as a function of g. The plots illustrate the non-analytic behavior of the stable mean-field branches at the critical point or rather threshold $g = g_c$ marked by the red stars in the figure.

The overall physical interpretation of the phase transition, especially with regard to the symmetry breaking, can surely be understood in analogy to the second order phase transition of the DOPO as explained in Sec. 3.2.1 and Sec. 3.4. The system-size parameter is here given by the number of atoms N which can equally be interpreted as the number of "nearest neighbors" of the photonic mode. The atoms do not interact with each other and thus the photonic mode can be considered as an impurity interacting with a structure free bath of atoms or rather qubits. From this point of view, the Dicke model is much simpler than the many-body lattice model of mutually interacting qubits introduced in Sec. (2.2). Consequently, the c-MoP equations will be drastically simplified which allows us to investigate different Ansatzes for the self-consistent Mori projectors in what follows.

5.2 C-MoP approach to the nonequilibrium Dicke model

We will now turn to the c-MoP equations and only focus on the symmetry preserving solutions within the theory. We start by identifying the bipartition of the full model by considering the photons as one part and the atoms as the other. Thus, we introduce the c-MoP projectors $\mathcal{P}_t^{at}(\cdot) = \rho_{at}(t) \otimes \mathrm{Tr}_{at}\{\cdot\}$ and $\mathcal{P}_t^{ph}(\cdot) = \mathrm{Tr}_{ph}\{\cdot\} \otimes \rho_{ph}(t)$. The reduced density matrix $\rho_{at}(t)$ includes all correlations between the atoms. For later use we will refer to $\mathcal{P}_t^{at}(\cdot)$ as the correlated projector for this reason. Moreover, we introduce the partition of the full Liouvillian $\mathcal{L}$ describing the NEDM in Eq. (5.1) such that $\dot{\rho}(t) = \mathcal{L}\rho(t)$ with $\mathcal{L} = \mathcal{L}_{ph} + \mathcal{L}_{at} + \mathcal{L}_I$ and

$$\begin{aligned}\mathcal{L}_{at}(\cdot) &= -i\left[\omega_z J_z, (\cdot)\right]\\ \mathcal{L}_{ph}(\cdot) &= -i\left[\omega_0 a^\dagger a, (\cdot)\right] + \kappa D_a(\cdot)\\ \mathcal{L}_I(\cdot) &= -i\frac{g}{\sqrt{N}}\left[J_x x_a, (\cdot)\right].\end{aligned} \tag{5.4}$$

By exploiting the techniques exemplified in detail in Chapter 3, especially in Sec. 3.3 and Sec. 3.3.2, and neglecting any symmetry breaking terms (including the mean-field terms), we can immediately state the c-MoP equations in the steady state for the NEDM by

$$\begin{aligned}\partial_t\rho_{at}^{ss} = 0 = \mathcal{L}_{at}\rho_{at}^{ss} - \frac{g^2}{N}\left[J_x\,, \int_0^\infty d\tau\, e^{\mathcal{L}_{at}\tau}\left(J_x\,\rho_{at}^{ss}\, d_{ph}(\tau) - \rho_{at}^{ss}\, J_x\, d_{ph}^*(\tau)\right)\right]\\ \partial_t\rho_{ph}^{ss} = 0 = \mathcal{L}_{ph}\rho_{ph}^{ss} - \frac{g^2}{N}\left[x_a\,, \int_0^\infty d\tau\, e^{\mathcal{L}_{ph}\tau}\left(x_a\,\rho_{ph}^{ss}\, d_{at}(\tau) - \rho_{ph}^{ss}\, x_a\, d_{at}^*(\tau)\right)\right],\end{aligned} \tag{5.5}$$

where $\rho_{ph(at)}^{ss}$ denotes the steady state reduced density matrix of the photons (atoms). In addition, the correlation functions read

$$\begin{aligned}d_{ph}(\tau) = \mathrm{Tr}_{ph}\{x_a e^{\mathcal{L}_{ph}\tau}\left(x_a\rho_{ph}^{ss}\right)\} = \langle a x_a\rangle_{ss}\, e^{(-i\omega_0-\kappa)\tau} + \langle a^\dagger x_a\rangle_{ss}\, e^{(i\omega_0-\kappa)\tau}\\ d_{at}(\tau) = \mathrm{Tr}_{at}\{J_x e^{\mathcal{L}_{at}\tau}\left(J_x\rho_{at}^{ss}\right)\} = \langle J J_x\rangle_{ss}\, e^{-i\omega_z\tau} + \langle J^\dagger J_x\rangle_{ss}\, e^{i\omega_z\tau}.\end{aligned} \tag{5.6}$$

Just as in the example of the DOPO for the pump mode, we find the photonic state ρ_{ph}^{ss} to be determined by a c-MoP equation which is quadratic in the operators a and $a^\dagger$. Thus, we find a closed set of equations for the photonic steady state variables $\langle a^\dagger a\rangle_{ss}$, $\langle a^2\rangle_{ss}$ and $\langle a^{\dagger 2}\rangle_{ss}$ which then depend on the state of the atoms.

The c-MoP equation for the atomic sector on the other hand is not quadratic and renders the main difficulty on our way to solve the c-MoP equations of the NEDM. We will present three possibilities to tackle such a difficulty.

A straightforward way to solve the c-MoP equations is to integrate Eq. (5.5) numerically. Here, the Hilbert space dimension scales as $2^N \times 2^N$. We show the result of the steady state photon number $\langle a^\dagger a\rangle_{ss}$ obtained from the full numerical solution of the c-MoP equation as a function of g in Fig. 5.1 (d) by the solid line for $N = 1, 2, ..., 6$. For comparison we also integrated the full master equation, eq. (5.1), for $N = 1, 2, ..., 5$ and illustrate the result by the dashed line in Fig. 5.1 (d). The dashed and solid lines match perfectly on the scale present in Fig. 5.1 (d) and therefore they are hardly distinguishable by eye in the plot. Thus, we find that the c-MoP equations give quasi-exact results, just as found in the previous example of the DOPO in Chapter 3. However, due to the exponential scaling of the Hilbert space dimension with increasing atom number, a full numerical integration of the c-MoP equation is not feasible for $N \geq 10$, despite its more favorable scaling as compared to the numerical integration of the full master equation which scales as $(2^N \times d_a) \times (2^N \times d_a)$, with d_a accounting for the Hilbert space dimension of the photon mode.

5.3 Correlated and uncorrelated projectors

The most efficient way to solve the c-MoP equation is to follow the ideas of Chapter 2 and introduce a self-consistent Mori projector which projects onto the factorized state of all constituents, that is each atom and the photons separately. We refer to this projector as the uncorrelated projector. In practice this amounts to writing $\rho_{at}(t) = \rho_1(t) \otimes \rho_2(t) \otimes ... \otimes \rho_N(t)$ for the projector introduced above in Sec 5.2. This step simplifies the c-MoP eqs. (5.5) considerably. They then read

$$\begin{aligned}
\partial_t \rho_1^{ss} &= 0 = \mathcal{L}_1 \rho_1^{ss} - \frac{g^2}{N}\left[\sigma^x\,, \int_0^\infty d\tau\, e^{\mathcal{L}_1\tau}\left(\sigma^x\, \rho_1^{ss}\, d_{ph}(\tau) - \rho_1^{ss}\, \sigma_x\, d_{ph}^*(\tau)\right)\right] \\
\partial_t \rho_{ph}^{ss} &= 0 = \mathcal{L}_{ph} \rho_{ph}^{ss} - g^2\left[x_a\,, \int_0^\infty d\tau\, e^{\mathcal{L}_{ph}\tau}\left(x_a\, \rho_{ph}^{ss}\, d_1(\tau) - \rho_{ph}^{ss}\, x_a\, d_1^*(\tau)\right)\right],
\end{aligned} \tag{5.7}$$

where $\mathcal{L}_1(\cdot) = -i\left[\omega_z \sigma_z, (\cdot)\right]$ denotes the free evolution of a single atom and ρ_1^{ss} denotes the steady state reduced density matrix of a single atom. Due to the symmetry of the Dicke model we have dropped the atom labeling for the spin operators. The first equation in eq. (5.7) can be directly obtained from the first equation in eq. (5.5) by taking $\rho_{at}(t) = \rho_1(t) \otimes \rho_2(t) \otimes ... \otimes \rho_N(t)$ and tracing over all but one atom. In addition, the single-atom correlation function reads

$$d_1(\tau) = \mathrm{Tr}_1\{\sigma^x e^{\mathcal{L}_1\tau}\left(\sigma^x \rho_1^{ss}\right)\} = \langle \sigma\sigma^x\rangle_{ss}\, e^{-i\omega_z\tau} + \langle \sigma^\dagger\sigma^x\rangle_{ss}\, e^{i\omega_z\tau}, \tag{5.8}$$

which can be directly deduced from $d_{at}(\tau)$ given in eq. (5.6). Note that the $1/N$ dependence of the Born term in the c-MoP equation for the photons is canceled in eq. (5.7).

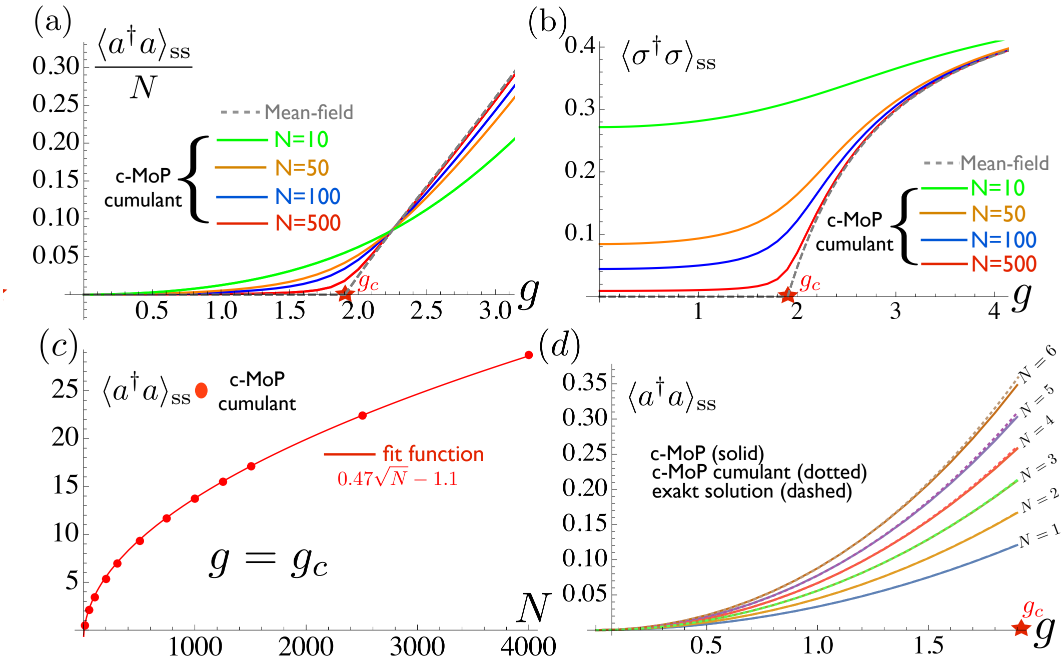

Figure 5.1: Steady state scaled photon number $\langle a^\dagger a\rangle_{ss}/N$ in part (a) and atomic occupation number in part (b) as a function of g obtained from mean-field theory (dashed gray line) and the cumulant c-MoP approach for $N = 10$ (green solid line), $N = 50$ (orange solid line), $N = 100$ (blue solid line) and $N = 500$ (red solid line). The second order dissipative phase transition occurs at $g = g_c$ marked by the red star. In part (c) we show the steady state photon number $\langle a^\dagger a\rangle_{ss}$ as a function of N at threshold $g = g_c$ obtained from the c-MoP cumulant approach (red dots) and a fit function (red solid thin line), indicating the critical scaling $\langle a^\dagger a\rangle_{ss} \sim \sqrt{N}$ of the photon number. In part (d) we show the steady state photon number $\langle a^\dagger a\rangle_{ss}$ as a function of g up to threshold obtained from a full simulation of the c-MoP equations (solid lines for $N = 1, 2, ..., 6$), from a full simulation of the exact Dicke model (dashed lines for $N = 1, 2, ..., 5$), and from the c-MoP cumulant approach (dotted lines for $N = 3, 4, 5, 6$). The difference between the dashed and solid lines is not visible indicating that the c-MoP equations lead to quasi exact results. The c-MoP cumulant approach deviates from the exact result at threshold for increasing atom numbers N. Parameters are $\omega_0 = 2$, $\omega_z = 1$ and $\kappa = 5$ which leads to $g_c \approx 1.904$.

Overall, the c-MoP equations obtained from an uncorrelated projector grant us with a closed set of equations for the variables $\langle a^\dagger a\rangle_{ss}$, $\langle a^2\rangle_{ss}$, $\langle a^{\dagger 2}\rangle_{ss}$ and $\langle \sigma^\dagger \sigma\rangle_{ss} = \mathrm{Tr}_1\{\sigma^\dagger \sigma \rho_1^{ss}\}$ which can be solved very efficiently. Surprisingly, one finds that the result for all these four variables will not depend on the number of atoms N. One can immediately understand this result by considering that $\mathrm{Tr}_1\{\sigma^\dagger \sigma \mathcal{L}_1 \rho_1^{ss}\} = 0$, and consequently the $1/N$ dependence in the Born term for the single atom in eq. (5.7) drops out. The photon number turns out to be given by an analytic function depending on the parameters $\omega_z, \omega_z, \kappa$ and g but not on N. Thus we find a scaling for the rescaled photon number $\langle a^\dagger a\rangle_{ss}/N \sim 1/N$ and conclude that the c-MoP equations obtained from the uncorrelated projector lead to a correction of the mean-field result which is suppressed as $1/N$. We emphasize however, that we are considering the solution branch which conserves the symmetry and therefore we should trust our findings only up to the critical point g_c. For the symmetry breaking solution, however, we expect a similar behavior.

At this point it is very insightful to consider the correlation function $d_{at}(\tau)$ from eq. (5.6) again. In particular we consider $\langle JJ_x\rangle_{ss}$ which we rewrite to

$$\langle JJ_x\rangle_{ss} = \sum_{i=1}^{N}\sum_{j=1}^{N}\langle \sigma_i\sigma_j^x\rangle_{ss} = N\langle\sigma_i\sigma_i^x\rangle_{ss} + N(N-1)\langle\sigma_i\sigma_j^x\rangle_{ss}, \tag{5.9}$$

since $\langle\sigma_i\sigma_i^x\rangle_{ss}$ and $\langle\sigma_i\sigma_j^x\rangle_{ss}$ are identical for all i, j. Clearly the on-site correlation function $\langle\sigma_i\sigma_i^x\rangle_{ss}$ contribute N-times to the total correlation function $\langle JJ_x\rangle_{ss}$ whereas the two-atom correlation function $\langle\sigma_i\sigma_j^x\rangle_{ss}$ dominates with a contribution scaling as $N(N-1) \sim N^2$. Within the uncorrelated projection operator approach the dominant contributions are completely neglected for the symmetry preserving solution branch since then $\langle\sigma_i\sigma_j^x\rangle_{ss} = \langle\sigma_i\rangle_{ss}\langle\sigma_j^x\rangle_{ss} = 0$. From this consideration it obviously seems highly desirable to account for two-atom correlations.

5.3.1 Cumulant expansion

Let us recall once more our findings so far. On the one hand we have the c-MoP equations (5.5) which are derived from a correlated projector and need to be solved fully numerically. This procedure gives quasi exact results below and at threshold but it is unfeasible for large atom numbers $N \geq 10$. On the other hand we have the uncorrelated c-MoP approach which is highly efficient but gives unreliable results for large atom numbers. Inspired by the success of the Gaussian c-MoP theory for the DOPO, see Sec. 3.6, we will now introduce a method that is both numerically feasible and accounts for the relevant two-atom correlations. We refer to this method as the cumulant c-MoP approach.

For the operators $A, B, C, D, ...$ we introduce the cumulants $\langle ...\rangle_C$ defined as

$$\begin{aligned}\langle A\rangle_C &= \langle A\rangle\\ \langle AB\rangle_C &= \langle AB\rangle - \langle A\rangle_C\langle B\rangle_C\\ \langle ABC\rangle_C &= \langle ABC\rangle - \langle AB\rangle_C\langle C\rangle_C - \langle AC\rangle_C\langle B\rangle_C - \langle BC\rangle_C\langle A\rangle_C - \langle A\rangle_C\langle B\rangle_C\langle C\rangle_C\\ \langle ABCD\rangle_C &= ...\end{aligned} \tag{5.10}$$

The cumulant expansion of n-th order neglects all cumulants of order higher than n. We will consider an expansion up to second order and thus we set $\langle ABC\rangle_C = 0$ and consequently $\langle ABC\rangle = \langle AB\rangle_C\langle C\rangle_C + \langle AC\rangle_C\langle B\rangle_C + \langle BC\rangle_C\langle A\rangle_C + \langle A\rangle_C\langle B\rangle_C\langle C\rangle_C$.

In our particular case we assign the Pauli operators with different atom label indices to the operators A, B and C. For example we write

$$\langle \sigma_i^z \sigma_j \sigma_m^\dagger \rangle_{ss} = \langle \sigma_i^z \rangle_{ss} \langle \sigma_j \sigma_m^\dagger \rangle_{ss} ,$$

where due to symmetry all but one term vanishes for $i \neq j \neq m$. Note that the Gaussian state approximation introduced in Sec. 3.6 is nothing but a cumulant expansion up to second order where the photonic field operators correspond to A, B and C.

Exploiting the cumulant expansion we are able to achieve both, we account for the very important two-atom correlation function $\langle \sigma_i \sigma_j^x \rangle_{ss}$ discussed in eq. (5.9), and find a closed set of equation from the c-MoP eq. (5.5) together with the conservation of total angular momentum in eq. (5.2). The resulting equations contain 8 variables and can be solved very efficiently for arbitrary values of N. The variables include the three photonic moments $\langle a^\dagger a \rangle_{ss}$, $\langle a^2 \rangle_{ss}$, $\langle a^{\dagger\, 2} \rangle_{ss}$ and five atomic moments $\langle \sigma_i^\dagger \sigma_i \rangle_{ss}$, $\langle \sigma_i^\dagger \sigma_i \sigma_j^\dagger \sigma_j \rangle_{ss}$, $\langle \sigma_i^\dagger \sigma_j \rangle_{ss}$, $\langle \sigma_i^\dagger \sigma_j^\dagger \rangle_{ss}$ and $\langle \sigma_i \sigma_j \rangle_{ss}$ for $i \neq j$.

We show the steady state scaled photon number $\langle a^\dagger a \rangle_{ss}/N$ in Fig. 5.1(a) and atomic occupation number in Fig. 5.1(b) as a function of g obtained from the cumulant c-MoP approach for $N = 10$ (green solid line), $N = 50$ (orange solid line), $N = 100$ (blue solid line) and $N = 500$ (red solid line). The second order dissipative phase transition occurs at $g = g_c$ marked by the red star. Here we see that the quantum fluctuations which are taken into account by the c-MoP cumulant approach deviate significantly from the mean-field result. Further, the mean-field result seems to become exact as N tends to infinity but strictly speaking only on the scale of $1/N$. In fact, the bare photon number diverges as $N \to \infty$ which is shown at threshold in Fig. 5.1(c) where we display the steady state photon number $\langle a^\dagger a \rangle_{ss}$ as a function of N obtained from the c-MoP cumulant approach (red dots) and a fit function (red solid thin line), indicating the critical scaling $\langle a^\dagger a \rangle_{ss} \sim \sqrt{N}$ of the photon number. The $\sqrt{N}$ scaling of the photon number was also found by the Keldysh formalism in Ref. [91] in the Holstein-Primakoff picture. Finally, in Fig. 5.1(d) we show the steady state photon number $\langle a^\dagger a \rangle_{ss}$ obtained from the c-MoP cumulant approach as a function of g up to threshold. Here, we see that the c-MoP cumulant approach offers a high quantitative accuracy which, however, decreases as the atom number increases, what can be understood considering the approximations performed within the cumulant expansion up to second order.

Summary of Part II

In Chapter 3 we exemplified the applicability of the self-consistent projection operator theory to nonlinear quantum optical systems on the case study of the degenerate optical parametric oscillator. We illustrated how our theory generalizes mean-field approaches and in particular adiabatic elimination methods to settings without time-scale separation. The effective master equations can be solved efficiently despite their non-Markovian structure. We demonstrated the high degree of accuracy of our method and revealed its capability to determine the exact quantum states below, at, and above the classical threshold for both the stationary limit and dynamical evolution. In addition, we developed a linearized theory consistent with the self-consistent Mori projector equations and showed its accuracy far beyond other known linearized approaches.

In Chapter 4 we combined adiabatic elimination techniques, semi-classical methods, and the Gaussian c-MoP theory to provide a theoretical analysis of the degenerate optomechanical parametric oscillator which works even at the critical point. We focused on the region where the optical field coupled to the mechanics is fully quantum, showing that such a quantum-correlated field with no coherent background can be used to induce significant optomechanical cooling through a "cooling by heating" mechanism. Our c-MoP techniques have allowed us to check the validity of the optical adiabatic elimination as well as the semi-classical approximation, whose predictions have indeed been shown to break down at threshold, showing the potential of c-MoP to treat dissipative quantum-optical problems in the vicinity of critical points.

Finally, in Chapter 5 we studied the second order dissipative phase transition of the nonequilibrium Dicke model for different c-MoP projector Ansatzes. The c-MoP theory accounting for interatomic correlations has been shown to lead to very accurate results for steady state observables. Further, a very efficient technique feasible for arbitrary atom numbers based on a cumulant expansion was introduced and shown to describe the finite-size corrections of the phase transition and its critical scaling behavior while still preserving the symmetry of the nonequilibrium Dicke model.

Conclusion and Outlook

Conclusion: In the present thesis we have introduced a novel theoretical approach to the treatment of quantum few- and many-body systems which we call *self-consistent projection operator theory* or in short **c-MoP**. Our theory exploits the key idea of projection operator methods as they are prominently used in open systems theory [4] or adiabatic elimination techniques [20, 33]. The first formal step in a projection operator approach consists in partitioning the whole quantum system into subparts, with a prominent example given by the bipartition of system and environment, followed by an elimination of all degrees of freedom not belonging to the subpart of interest. Formally, such elimination can be achieved by introducing the Mori projection operator which ultimately enables the derivation of exact equations of motion for the reduced quantum states. These exact Nakajima-Zwanzig equations, however, are not solvable in their full generality and thus approximations need to be performed. So far, in the applications of projection operator approaches the environmental reference states, that is all degrees of freedom but the ones of interest, are taken to be time-independent. This constitutes a strong approximation being well justified for quantum systems consisting of subparts with different size or rather subparts evolving on different time-scales.

The main achievement of the c-MoP theory is to generalize the concept of projection operator methods by introducing a time-dependent Mori projector to account for a dynamically evolving environment. As shown in this thesis, the framework of the c-MoP theory allows for the derivation of an exact equation of motion for reduced states of all the subparts. In strong contrast to standard projection operator approaches, the applied approximation on the exact c-MoP equations, namely the Born approximation, does not rely on a clear time-scale separation between the dynamics of the subparts. Thus, the c-MoP theory suggest to be applicable to physical systems in which all the subparts have similar sizes and characteristic dynamical times. In this way c-MoP complements standard projection operator methods holding the long-term promise to become a well-established tool enlarging the scope of the theory of open systems.

In addition, we have shown that in the lowest order approximation c-MoP becomes equivalent to mean-field approaches and therefore forms a systematic generalization of mean-field theories taking non-Markovian back-action between the subparts of the system into account. This fact motivates the application of c-MoP to quantum many-body problems.

In order to substantiate the presumptions made from the general framework of the c-MoP theory we applied it to few-body bosonic quantum-optical problems as well as to unitary and driven-dissipative many-body lattice scenarios. In particular, within the scope of this thesis, we studied open and closed spin lattices in one and two dimensions, the degenerate opto(-mechanical) parametric oscillator (DO(M)PO) and the nonequilibrium Dicke model. Throughout the applications we tested the accuracy of c-MoP by comparing it to (quasi) exact results, if these were available, and also to other approximative methods such as linearized descriptions, mean-field theory or in the case of the DOPO even to the Keldysh formalism within the self-consistent Hartree-Fock approximation. In the considered cases we found c-MoP to outperform all of these approximative methods and for 1D spin lattices to compare with the performance of t-DMRG calculations for local observables. Essentially, in all the scenarios investigated here, we showed that c-MoP theory accurately describes the physics of the driven and dissipative phase transitions, even at the critical points, and includes mean-field theory and adiabatic elimination methods as its limiting cases.

With all these applications, we clearly demonstrated the usefulness of c-MoP theory in this thesis. However, we also highlighted how different choices for the self-consistent Mori projector as well as partitions of the full system into the subparts can lead to significantly different efficiencies and accuracies. The possible choices for the partitions and the according Mori projectors are limited by the ability to solve the nonlinear and non-Markovian c-MoP equations.

For the many-body lattice problems we suggested here to implement a partition of the lattice into small subgroups or rather clusters of lattice sites. The corresponding self-consistent Mori projectors then projected the full lattice state onto a factorized state of all the clusters. This choice allowed us to derive efficient c-MoP equations for the local observables reaching a reduction of complexity similar to mean-field approaches. As a consequence we could straightforwardly increase the considered cluster sizes and in this way provide a control handle for the convergence of our results.

We found that the accuracy of the clustered c-MoP approach improves fast as the size of the clusters is increased. In fact, for the one dimensional quench problem in the Heisenberg XX spin chain, where exact results are available for comparison, the time ranges accurately described by the cluster c-MoP approach increase linearly with the cluster size. We could numerically solve the c-MoP equations up to a cluster size of 10 sites and show that the result compares to time ranges reached with t-DMRG methods [58]. In the case of the driven and dissipative Heisenberg XX spin model, we showed that the c-MoP equations can be reduced to simple algebraic equations in order to directly solve for the stationary state. We found that increasing the cluster size reaches a convergence in the steady state observables which allowed us to conclude that c-MoP gives an efficient method to accurately determine local observables in the thermodynamic limit. We have verified the c-MoP predictions with a finite-size scaling using t-DMRG methods for the dissipative scenario as well.

As a direct application, we investigated a nonequilibrium mean-field phase transition of first order, to which we referred as the quantum to classical transition, appearing in the locally driven and dissipative Heisenberg XX spin model. We argued for the system-size parameter driving the phase transition to be given by the coordination number of the lattice. Thus, the phase transition appearing somewhere in the bistable region predicted by the mean-field analysis becomes sharp in the limit of infinite dimensions only, while for a fixed spatial dimension the transition is expected to be smooth even in the case where the number of lattice sites tends to infinity. Indeed, by exploiting the clustered c-MoP approach we found a strong signature for the absence of the phase transition both in one and two spatial dimensions even in the thermodynamic limit of infinite lattice sites. Our results provide an understanding of the dissipative nature of the phase transition and provide a physical explanation of the bistability from the mean-field analysis which at first sight seems to be somewhat obscure. The absence of the phase transition for one dimensional lattices has been observed for different dissipative models [134, 135] as well.

The results for the two dimensional lattice were obtained by simply applying the same techniques that were introduced in this thesis. In fact, the general framework for the application of c-MoP to many-body systems as presented here, allows to apply the theory to any lattice geometry and any spatial dimension by simply adding additional terms which depend on the exact shape of the lattice. However, we have also argued that some relevant processes are not taken into account by the c-MoP method based on the partition of the lattice into clusters. These 'corner' processes become less important as the cluster size increases. Nonetheless, increasing the cluster size in two or more spatial dimensions is numerically much more expensive than in one spatial dimension. We showed in this thesis that these 'corner' processes could be taken into account by considering a more general choice employing a bipartition of the entire lattice into one small cluster of lattice sites and the remainder of the lattice. The resulting c-MoP equation would than lead to local quantities that will depend on non-local ones and thus be very inefficient or in general unsolvable without any further approximations.

This issue arrises in any projection operator based theory where the prerequisites needed for a solvable model consist in the ability to solve both the isolated system and environment. In our case the isolated environment would still be given by a large many-body lattice model. Therefore, solving an impurity model is much simpler than solving the full lattice model. In the light of this insight, we suggest to explore in future work whether c-MoP theory can be combined with ideas from dynamical mean-field theory (DMFT) where the mapping from the full lattice model onto a quantum impurity model is performed at the initial stages of the approach [112].

In order to put emphasis onto this topic, we have further performed c-MoP calculations for the nonequilibrium Dicke model [38] and explicitly tested different projection operator Ansatzes. The Dicke model consists of a dissipative photonic mode coupled to N non-interacting two-level atoms. In this sense it can be understood as an impurity model. We have verified that the bipartition into the photonic mode as one subsystem and all the remaining atoms leads to a c-MoP theory which describes the phase transition very efficiently and accurately, even capturing the correct critical scaling behavior [91] of the model. In contrast, the partition of the Dicke model into the photonic mode and all the atoms one by one separately leads to a c-MoP equation which only leads to small corrections to the mean-field predictions that tend to zero with $1/N$.

In the case of the DOPO, which is a nonlinear photonic two-mode problem, the bipartition was naturally taken by the two modes of the system. More importantly, we were able to state c-MoP equations and solve them such that all linear parts of the interaction were accounted for exactly, that is up to all orders in the interaction, while only the nonlinear part of the interaction was expanded up to second order. In this case, we obtained quasi exact results for the full reduced density matrices below, at and above the critical point of the second order dissipative phase transition. The favorable scaling of the c-MoP equations, in contrast to the full master equation, allowed us to enter a larger regime of the parameter space and even extract the full Wigner function of the reduced state. Away from the adiabatic limit, such a result has not been obtained before. Most importantly, however, in the context of this thesis, the case study on the DOPO illustrated the solution procedure for the non-Markovian c-MoP equations and the need to restrict the Born approximation only to the nonlinear part of the inter-mode interaction. If these prerequisites are maintained for a c-MoP calculation, we expect similar results for any other nonlinear problem of quantum optics such as the (one-atom) laser [4, 20], optomechanics [69], and the dissipative Dicke model [38] in the Holstein-Primakof limit [91, 136, 137].

As a direct application of the c-MoP method developed for the DOPO we introduced a theoretical approach that is capable of describing the below threshold regime of degenerate optomechanical parametric oscillators, even at the critical point itself. We found that the down-converted field, which is of purely quantum mechanical nature, can induce significant mechanical cooling and identified the process responsible of this as a "cooling by heating" mechanism. Moreover, we showed that, contrary to naive expectations and semi-classical predictions, cooling is not optimal at the critical point, where the photon number is largest. All the works so far on the OMPO [90, 127–129] have focused on regions of the parameter space far from the critical point solving the problem through a semi-classical approach or rather a standard linearization. In these works, however, the parameter range was either far below threshold or an additional coherent injection at the down-converted mode was considered.

Thus, we believe that we have solved a hard problem for the quantum optics community using c-MoP theory which gave three significant contributions. For one, it justified the semi-classical theory in the "cooling by heating" parameter regime, second, it allowed to extend the theory beyond that regime up to the critical point and showed the breakdown of the semi-classical predictions together with the cooling, and third, it allowed to justify the time-scale separation between the optical and the mechanical modes for the experimentally relevant situation. Especially, the latter did not seem obvious as the optical modes experience a significant change of their relaxation rates in the critical slowing-down regime. At this point it is foreseeable that experiments will be able to study parameter regions where back-action effects of the mechanics on the optics will become significant, in which case we suppose the c-MoP approach to be very useful.

Outlook: In summary, we have illustrated the relevance of the c-MoP theory and that the methods developed in this thesis can be directly applied to nonlinear quantum optical as well as to closed or open many-body lattice models. Thus, one objective for future research simply consists in further applications of the c-MoP theory. In addition, future advancements of the methodology could include more efficient numerical strategies to solve the c-MoP equations together with a possible combination of c-MoP theory and field theoretical methods such as dynamical mean-field theory. Also, the investigation of higher order terms in the expansion of the generalized Nakajima-Zwanzig equation provides an intriguing task for future research.

As one natural example in the context of quantum optical problems we suggest to apply c-MoP to the dissipative Dicke model in the Holstein-Primakof picture [38, 91]. This model constitutes an example where the methods developed here can be directly applied. We expect c-MoP to deliver the (reduced) quantum states below, at and above the critical point and thus give access to higher order correlation functions reaching beyond the studies presented for example in Ref. [91, 136]. Moreover, it will be possible to study dissipative quenches where interesting phenomena are expected to appear [137].

In the context of many-body applications it seems natural to apply the c-MoP method to study higher dimensional lattices or lattices with frustration, especially in the context of open systems. Moreover, one can reach beyond the spin models presented in this thesis. In particular, one can use c-MoP to study Bose-Hubbard models in the driven and dissipative scenario [24]. There, the mean-field phase diagram is known [68] but especially in lattice dimensions larger than one the physics is still elusive, and it is not yet clear whether there is a finite critical dimension for the phase transition appearing in the mean-field result. In order to shed light onto this topic we suggest to apply the c-MoP methods developed here to the driven and dissipative Bose-Hubbard model in momentum space [56] rather than in position space. From a technical point of view, one can either partition the full state into all the momentum modes, or more promisingly into the driven mode (in the case of homogeneous driving in position space there is only one driven mode in momentum space) and the rest of the modes. The on-site nonlinear Hubbard interaction in position space translates into nonlinear modal interactions which are known as 4-wave mixing terms. All the modes which fulfill momentum conservation can in principle scatter with each other. We suggest to neglect all scattering processes which do not include the driven mode and thus obtain an impurity model which can be solved within the c-MoP framework presented here. In this model it will be evident that the system-size parameter is given by the number of lattice sites and thus it will allow us to study the dissipative phase transition in the Bose-Hubbard model at fixed spatial dimensions but with varying number of lattices sites.

Bibliography

[1] K. Gottfried and T.-M. Yan, *Quantum Mechanics: Fundamentals*, Springer (2003).

[2] L. D. Landau and E. M. Lifshitz, *Statistical Physics, Volume 5*, Elsevier (1980).

[3] R. Zwanzig, *Nonequilibrium Statistical Mechanics*, Oxford University Press, Oxford (2001).

[4] H.-P. Breuer and F. Petruccione, *The Theory of Open Quantum Systems*, Oxford University Press (2007).

[5] *Quantum Noise*, C. W. Gardiner and P. Zoller (Springer-Verlag, Berlin Heidelberg, 2004).

[6] D.F. Walls and G. Milburn, *Quantum Optics*, Springer (2007)

[7] M. O. Scully and M. S. Zubairy, *Quantum Optics*, Cambridge University Press (1997)

[8] A. Altland and B. Simons, *Condensed matter field theory*, Cambridge University Press (2010)

[9] S. Sachdev, *Quantum Phase Transitions*, Cambridge University Press (2011).

[10] H. Bethe, *Zur Theorie der Metalle. I. Eigenwerte und Eigenfunktionen der linearen Atomkette*, Zeitschrift für Physik **71**, 205226 (1931)

[11] P. D. Drummond and D. F. Walls, *Quantum theory of optical bistability. I. Nonlinear polarisability model*, J. Phys. A: Math. Gen. **13**, 725 (1980).

[12] M. Wolinsky and H. J. Carmichael, *Quantum noise in the parametric oscillator: From squeezed states to coherent-state superpositions*, Phys. Rev. Lett., **60**, 1836 (1988).

[13] V. Weisskopf and E. Wigner, *Berechnung der natürlichen Linienbreite auf Grund der Diracschen Lichttheorie*, Z. Phys., **63**, 54-73, (1930).

[14] A. J. Leggett, S. Chakravarty, A. T. Dorsey, M. P. A. Fisher, A. Garg and W. Zwerger, *Dynamics of the dissipative two-state system* Rev. Mod. Phys., **59**, 1-85, (1987).

[15] D. V. Hutton, *Fundamentals of finite element analysis*, Mc-Graw-Hill, (2004).

[16] P. Giannozzi, *Numerical methods in quantum mechanics*, University of Udine, (2013).

[17] L. P. Kadanoff, *More is the Same; Mean Field Theory and Phase Transitions*, J. Stat. Phys. **137**, 777 (2009).

[18] M. P. A. Fisher, P. B. Weichman, G. Grinstein, and D. S. Fisher, *Boson localization and the superfluid-insulator transition*, Phys. Rev. B **40**, 546 (1989).

[19] H. J. Carmichael, *Statistical Methods in Quantum Optics 1*, Springer Verlag, Berlin (2002).

[20] H. J. Carmichael, *Statistical Methods in Quantum Optics 2*, Springer Verlag, Berlin (2008).

[21] H. Mori, *Transport, Collective Motion, and Brownian Motion*, Prog. Theor. Phys. **33**, 423 (1965).

[22] G. Lindblad, *On the generators of quantum dynamical semigroups*, Comm. Math. Phys. 48, **119** (1976).

[23] A. Rivas and S. F. Huelga, *Open Quantum Systems. An Introduction*, Springer, (2011).

[24] M. J. Hartmann, F. G. S. L. Brandão, and M. B. Plenio, *Strongly Interacting Polaritons in Coupled Arrays of Cavities*, Nature Phys. **2**, 849 (2006).

[25] S. Diehl, A. Micheli, A. Kantian, B. Kraus, H.P. Büchler, and P. Zoller, *Quantum States and Phases in Driven Open Quantum Systems with Cold Atoms*, Nature Phys. **4**, 878 (2008).

[26] S. Diehl, A. Tomadin, A. Micheli, R. Fazio, and P. Zoller, *Dynamical Phase Transitions and Instabilities in Open Atomic Many-Body Systems*, Phys. Rev. Lett. **105**, 015702 (2010).

[27] I. de Vega and D. Alonso, *Dynamics of non-Markovian open quantum systems*, arXiv:1511.06994 (2015).

[28] J. Prior, A. W. Chin, S. F. Huelga, and M. B. Plenio, *Efficient simulation of strong system-environment interactions*, Phys. Rev. Lett. **105** (5), 050404 (2010).

[29] H.-P. Breuer, *Non-Markovian generalization of the Lindblad theory of open quantum systems* Phys. Rev. A **75**, 022103 (2007).

[30] B. R. Mollow, *Power Spectrum of Light Scattered by Two-Level Systems*, Phys. Rev., **188**, 1969 (1969).

[31] P. Degenfeld-Schonburg, E. del Valle and M. J. Hartmann, *Signatures of single-site addressability in resonance fluorescence spectra*, Phys. Rev. A **85**, 013842 (2012).

[32] P. Degenfeld-Schonburg and M. J. Hartmann, *Self-consistent projection operator theory for quantum many-body systems*, Phys. Rev. B **89**, 245108 (2014).

[33] I. Wilson-Rae, N. Nooshi, W. Zwerger, and T. J. Kippenberg, *Theory of ground state cooling of a mechanical oscillator using dynamical backaction*, Phys. Rev. Lett. **99**, 093901 (2007).

[34] J. I. Cirac, R. Blatt, P. Zoller, and W. D. Phillips, Phys. Rev. A **46**, 2668 (1992)

[35] D. S. Rokhsar and B. G. Kotliar, *Gutzwiller projection for bosons*, Phys. Rev. B **44**, 10328 (1991).

[36] F. Nissen, S. Schmidt, M. Biondi, G. Blatter, H.E. Türeci, and J. Keeling, *Nonequilibrium Dynamics of Coupled Qubit-Cavity Arrays*, Phys. Rev. Lett. **108**, 233603 (2012).

[37] J. Jin, D. Rossini, R. Fazio, M. Leib, and M. J. Hartmann, *Photon solid phases in driven arrays of non-linearly coupled cavities*, Phys. Rev. Lett. **110**, 163605 (2013).

[38] F. Dimer, B. Estienne, A. S. Parkins, and H. J. Carmichael, *Proposed realization of the Dicke-model quantum phase transition in an optical cavity QED system*, Phys. Rev. A, **75**, 013804 (2007).

[39] O. Veits and M. Fleischhauer, *Quantum fluctuations in the Optical Parametric Oscillator in the limit of a fast decaying subharmonic mode*, Phys. Rev. A **52**, 4344 (1995).

[40] T. Mori, *Exactness of the mean-field dynamics in optical cavity systems*, J. Stat. Mech., **06**, P06005 (2013)

[41] L. E. Reichl, *A Modern Course in Statistical Physics*, John Wiley, New York (1998).

[42] R. W. Boyd, *Nonlinear optics*, Academic Press (2003).

[43] A. G. Redfield, *On the theory of relaxation processes*, IBM J. Res. Dev., **1**, 19 (1957).

[44] K. Blum, *Density Matrix Theory and Applications*, Plenum Press, New York (1981).

[45] M. Z. Hasan and C. L. Kane, *Colloquium: Topological insulators*, Rev. Mod. Phys. **82**, 3045 (2010).

[46] C. Nayak, S. H. Simon, A. Stern, M. Freedman, and S. Das Sarma, *Non-Abelian anyons and topological quantum computation*, Rev. Mod. Phys. **80**, 1083 (2008).

[47] A. J. Leggett, *What DO we know about high T_c?*, Nature Phys. **2**, 134 (2006).

[48] U. Schollwöck, *The density-matrix renormalization group*, Rev. Mod. Phys. **77**, 259 (2005).

[49] R. Fazio and H.S.J. van der Zant, *Quantum Phase Transitions and Vortex Dynamics in Superconducting Networks*, Phys. Rep. **355**, 235 (2001).

[50] I. Bloch, J. Dalibard and W. Zwerger, *Many-body physics with ultracold gases*, Rev. Mod. Phys. **80**, 885 (2008).

[51] R. Islam, C. Senko, W. C. Campbell, S. Korenblit, J. Smith, A. Lee, E. E. Edwards, C.-C. J. Wang, J. K. Freericks, and C. Monroe, *Emergence and Frustration of Magnetic Order with Variable-Range Interactions in a Trapped Ion Quantum Simulator*, Sience **340**, 583 (2013).

[52] J. T. Barreiro, M. Müller, P. Schindler, D. Nigg, T. Monz, M. Chwalla, M. Hennrich, C. F. Roos, P. Zoller, and R. Blatt, *An open-system quantum simulator with trapped ions*, Nature **470**, 486 (2011).

[53] C. Kollath, A. M. Läuchli, and E. Altman, *Quench Dynamics and Nonequilibrium Phase Diagram of the Bose-Hubbard Model* Phys. Rev. Lett. **98**, 180601 (2007).

[54] S. Trotzky, Y-A. Chen, A. Flesch, I. P. McCulloch, U. Schollwöck, J. Eisert, and I. Bloch, *Probing the relaxation towards equilibrium in an isolated strongly correlated one-dimensional Bose gas*, Nature Phys. **8**, 325 (2012).

[55] T. Prosen and I. Pižorn, *Quantum Phase Transition in a Far-from-Equilibrium Steady State of an XY Spin Chain*, Phys. Rev. Lett. **101**, 105701 (2008).

[56] M. J. Hartmann, *Polariton Crystallization in Driven Arrays of Lossy Nonlinear Resonators*, Phys. Rev. Lett., **104**, 113601 (2010).

[57] S. Diehl, E. Rico, M. A. Baranov, and P. Zoller, *Topology by dissipation in atomic quantum wires*, Nature Phys. **7**, 971 (2011).

[58] A. Flesch, M. Cramer, I. P. McCulloch, U. Schollwöck, and J. Eisert, *Probing local relaxation of cold atoms in optical superlattices*, Phys. Rev. A **78**, 033608 (2008).

[59] V. Lakshmikantham, M. Rama Mohana Rao, *Theory of Integro-Differential Equations*, CRC Press (1995).

[60] We greatly acknowledge Johannes Lang for support with the implementation of a Heun method that allowed us to choose larger time steps Δt without spoiling the accuracy. This step made the numerical integration of the c-MoP equations more efficient and allowed for the calculation of the c-MoP equations for a 10-site cluster.

[61] P. Barmettler, M. Punk, V. Gritsev, E. Demler, and E. Altman, *Quench Dynamics and Nonequilibrium Phase Diagram of the Bose-Hubbard Model* Phys. Rev. Lett. **102**, 130603 (2009).

[62] C. Navarrete-Benlloch, *Open systems dynamics: Simulating master equations in the computer*, arxiv:1504.05266.

[63] S. G. Schirmer and Xiaoting Wang, *Stabilizing open quantum systems by Markovian reservoir engineering*, Phys. Rev. A **81**, 062306 (2010).

[64] M. J. Hartmann, J. Prior, S. R. Clark and M.B. Plenio, *Density Matrix Renormalization Group in the Heisenberg Picture*, Phys. Rev. Lett., **102**, 057202 (2009).

[65] E. del Valle and M.J. Hartmann, *Correlator expansion approach to stationary states of weakly coupled cavity arrays*, J. Phys. B: At. Mol. Opt. Phys. **46**, 224023 (2013).

[66] Andy C.Y. Li, F. Petruccione, and Jens Koch, *Perturbative approach to Markovian open quantum systems*, Sci. Rep. **4**, 4887 (2014).

[67] M.A. Nielsen and I.L. Chuang, *Quantum Computation and Quantum Information*, Cambridge University Press 2000.

[68] A. Le Boité, G. Orso, and C. Ciuti, *Steady-State Phases and Tunneling-Induced Instabilities in the Driven Dissipative Bose-Hubbard Model*, Phys. Rev. Lett. **110**, 233601 (2013).

[69] M. Aspelmeyer, T. J. Kippenberg, and F. Marquardt, *Cavity optomechanics*, Rev. Mod. Phys. **86**, 1391 (2014).

[70] S. Pina-Otey, F. Jimenez, P. Degenfeld-Schonburg, and C. Navarrete-Benlloch, *Classical and quantum linearized descriptions of degenerate optomechanical parametric oscillators* arxiv:1412.2521.

[71] P. D. Drummond, K. J. McNeil, and D. F. Walls, *Non-equilibrium transitions in sub/second harmonic generation, I. Semiclassical theory*, Optica Acta., **27**, 321 (1980).

[72] S. Aldana, C. Bruder, and A. Nunnenkamp, *Equivalence between an optomechanical system and a Kerr medium* Phys. Rev. A, **88**, 043826 (2013).

[73] H. Spohn, *An algebraic condition for the approach to equilibrium of an open N-Level system*, Lett. Math. Phys. 2, **33** (1977).

[74] H. Weimer, *Variational principle for steady states of dissipative quantum many-body systems* Phys. Rev. Lett., **114**, 040402 (2015).

[75] K. Staliunas and V. J. Sanchez-Morcillo, *Transverse Patterns in Nonlinear Optical Resonators*, Springer (2002).

[76] P. Meystre and D. F. Walls (eds.), *Nonclassical Effects in Quantum Optics*, American Institute of Physics, New York (1991).

[77] M. J. Hartmann and M. B. Plenio, *Strong Photon Nonlinearities and Photonic Mott Insulators*, Phys. Rev. Lett. **99**, 103601 (2007).

[78] F. G. S. L. Brandão, M. J. Hartmann, and M. B. Plenio, *Light-shift-induced photonic nonlinearities*, New J. Phys. **10**, 043010 (2008).

[79] K. Goda, O. Miyakawa, E. E. Mikhailov, S. Saraf, R. Adhikari, K. McKenzie, R. Ward, S. Vass, A. J. Weinstein, and N. Mavalvala, *A quantum-enhanced prototype gravitational-wave detector*, Nat. Phys., **4**, 472 (2008).

[80] H. Vahlbruch, S. Chelkowski, B. Hage, A. Franzen, K. Danzmann, R. and Schnabel, *Demonstration of a Squeezed-Light-Enhanced Power- and Signal-Recycled Michelson Interferometer*, Phys. Rev. Lett., **95**, 211102 (2005).

[81] N. Treps, N. Grosse, W. P. Bowen, C. Fabre, H.-A. Bachor, and P. K. Lam, *A quantum laser pointer*, Science, **301**, 940 (2003).

[82] N. Treps, U. Andersen, B. Buchler, P. K. Lam, A. Maitre, H.-A. Bachor, and C. Fabre, *Surpassing the standard quantum limit for optical imaging using nonclassical multimode light*, Phys. Rev. Lett., **88**, 203601 (2002).

[83] S. L. Braunstein and P. van Loock, *Quantum information with continuous variables*, Rev. Mod. Phys., **77**, 513 (2005).

[84] C. Weedbrook, S. Pirandola, R. Garcia-Patron, N. J. Cerf, T.C. Ralph, J.H. Shapiro, and S. Lloyd, *Gaussian quantum information*, Rev. Mod. Phys., **84**, 621 (2012).

[85] M. D. Reid and P. D. Drummond, *Quantum Correlations of Phase in Nondegenerate Parametric Oscillation*, Phys. Rev. Lett. **60**, 2731-2733 (1988).

[86] P. D. Drummond and M. D. Reid, *Correlations in nondegenerate parametric oscillation. II. Below threshold results*, Phys. Rev. A **41**, 3930-3949 (1990).

[87] C. Navarrete-Benlloch, E. Roldán, and G. J. de Valcárcel, *Noncritically Squeezed Light via Spontaneous Rotational Symmetry Breaking*, Phys. Rev. Lett. **100**, 203601 (2008).

[88] C. Navarrete-Benlloch, G. J. de Valcárcel, and E. Roldán, *Generating highly squeezed hybrid Laguerre-Gauss modes in large-Fresnel-number degenerate optical parametric oscillators*, Phys. Rev. A **79**, 043820 (2009).

[89] L. Mandel and E. Wolf, *Optical coherence and quantum optics*, Cambridge University Press (1995).

[90] X.-Y. Lü, Y. Wu, J.R. Johansson, H. Jing, J. Zhang, and F. Nori, *Squeezed Optomechanics with Phase-matched Amplification and Dissipation*, Phys. Rev. Lett. **114**, 093602 (2015).

[91] E. G. Dalla Torre, S. Diehl, M. D. Lukin, S. Sachdev, and P. Strack, *Keldysh approach for nonequilibrium phase transitions in quantum optics: Beyond the Dicke model in optical cavities*, Phys. Rev. A, **87**, 023831 (2013).

[92] H. Ritsch, P. Domokos, F. Brennecke, and T. Esslinger, *Cold atoms in cavity-generated dynamical optical potentials*, Rev. Mod. Phys. **85**, 553 (2013).

[93] P. D. Drummond, K. J. McNeil, and D. F. Walls, *Non-equilibrium transitions in sub/second harmonic generation*, J. Mod. Opt., **28**, 211 (1980).

[94] P. D. Drummond and C. W. Gardiner, *Generalised P-representations in quantum optics*, J. Phys. A: Math. Gen., **13**, 2353 (1980).

[95] P. Kinsler, M. Fernee, and P. D. Drummond, *Limits to squeezing and phase information in the parametric amplifier*, Phys. Rev. A, **48**, 3310 (1993).

[96] P. Kinsler and P. D. Drummond, *Critical fluctuations in the quantum parametric oscillator*, Phys. Rev. A, **52**, 783 (1995).

[97] P. D. Drummond, K. Dechoum, and S. Chaturvedi, *Critical quantum fluctuations in the degenerate parametric oscillator*, Phys. Rev. A, **65**, 033806 (2002).

[98] S. Chaturvedi and P. D. Drummond, *Stochastic diagrams for critical point spectra*, Eur. Phys. J. B, **8**, 251 (1999).

[99] O. Veits and M. Fleischhauer, *Effects of finite-system size in nonlinear optical systems: A quantum many-body approach to parametric oscillation*, Phys. Rev. A **55**, 3059 (1997).

[100] C. J. Mertens, T. A. B. Kennedy, and S. Swain, *Many-body theory of quantum noise*, Phys. Rev. Lett., **71**, 2014 (1993).

[101] C. J. Mertens, T. A. B. Kennedy, and S. Swain, *Many-body quantum theory of the optical parametric oscillator*, Phys. Rev. A, **48**, 2374 (1993).

[102] L. A. Lugiato and G. Strini, Opt. Commun., **41**, 67 (1981).

[103] M. J. Collett and C. W. Gardiner, *Squeezing of intracavity and traveling-wave light fields produced in parametric amplification*, Phys. Rev. A, **30**, 1386 (1984).

[104] C. Navarrete-Benlloch, E. Roldán, Y. Chang, and T. Shi, *Regularized linearization for quantum nonlinear optical cavities: application to degenerate optical parametric oscillators*, Optics Express **22**, 024010 (2014)

[105] S. Gigan, L. Lopez, V. Delaubert, N. Treps, C. Fabre, and A. Maitre, *Continuous-wave phase-sensitive parametric image amplification*, J. Mod. Opt. 53, 809 (2006).

[106] C. Navarrete-Benlloch, *An introduction to the formalism of quantum information*, arxiv:1504.05270.

[107] P. Kinsler and P.D. Drummond, *Quantum dynamics of the parametric oscillator*, Phys. Rev. A, **43**, 6194 (1991).

[108] C. Navarrete-Benlloch, J. J. García-Ripoll, and Diego Porras, *Inducing Nonclassical Lasing via Periodic Drivings in Circuit Quantum Electrodynamics*, Phys. Rev. Lett. **113**, 193601 (2014).

[109] T. Eberle, S. Steinlechner, J. Bauchrowitz, V. Handchen, H. Vahlbruch, M. Mehmet, H. Muller-Ebhardt, and R. Schnabel, *Quantum Enhancement of the Zero-Area Sagnac Interferometer Topology for Gravitational Wave Detection*, Phys. Rev. Lett., **104**, 251102 (2010).

[110] H. Vahlbruch, M. Mehmet, S. Chelkowski, B. Hage, A. Franzen, N. Lastzka, S. Gossler, K. Danzmann, and R. Schnabel, *Observation of*

Squeezed Light with 10-dB Quantum-Noise Reduction, Phys. Rev. Lett., **100**, 033602 (2008).

[111] Z. Leghtas, S. Touzard, I. M. Pop, A. Kou, B. Vlastakis, A. Petrenko, K. M. Sliwa, A. Narla, S. Shankar, M. J. Hatridge, M. Reagor, L. Frunzio, R. J. Schoelkopf, M. Mirrahimi, and M. H. Devoret, *Confining the state of light to a quantum manifold by engineered two-photon loss*, Science, **347**, 853, (2015)

[112] H. Aoki, N. Tsuji, M. Eckstein, M. Kollar, T. Oka, and P. Werner, *Nonequilibrium dynamical mean-field theory and its applications*, Rev. Mod. Phys. **86**, 779 (2014).

[113] C. Navarrete-Benlloch, *Contributions to the Quantum Optics of Multi-mode Optical Parametric Oscillators*, arXiv:1504.05917.

[114] V. S. Ilchenko, A. A. Savchenkov, A. B. Matsko, and L. Maleki, *Whispering-gallery-mode electro-optic modulator and photonic microwave receiver*, J. Opt. Soc. Am. B **20**, 333 (2003).

[115] V. S. Ilchenko, A. A. Savchenkov, A. B. Matsko, and L. Maleki, *Nonlinear Optics and Crystalline Whispering Gallery Mode Cavities*, Phys. Rev. Lett. **92**, 043903 (2004).

[116] A. A. Savchenkov, A. B. Matsko, M. Mohageg, D. V. Strekalov, and L. Maleki, *Parametric oscillations in a whispering gallery resonator*, Opt. Lett. **32**, 157 (2007).

[117] J. U. Fürst, D. V. Strekalov, D. Elser, M. Lassen, U. L. Andersen, Ch. Marquardt, and G. Leuchs, *Naturally Phase-Matched Second-Harmonic Generation in a Whispering-Gallery-Mode Resonator*, Phys. Rev. Lett. **104**, 153901 (2010).

[118] J. U. Fürst, D. V. Strekalov, D. Elser, A. Aiello, U. L. Andersen, Ch. Marquardt, and G. Leuchs, *Low-Threshold Optical Parametric Oscillations in a Whispering Gallery Mode Resonator*, Phys. Rev. Lett. **105**, 263904 (2010).

[119] J. Hofer, A. Schliesser, and T. J. Kippenberg, *Cavity optomechanics with ultrahigh-Q crystalline microresonators*, Phys. Rev, A **82**, 031804(R) (2010).

[120] J. U. Fürst, D. V. Strekalov, D. Elser, A. Aiello, U. L. Andersen, Ch. Marquardt, and G. Leuchs, *Quantum Light from a Whispering-Gallery-Mode Disk Resonator*, Phys. Rev. Lett. **106**, 113901 (2011).

[121] T. Beckmann, H. Linnenbank, H. Steigerwald, B. Sturman, D. Haertle, K. Buse, and I. Breunig, *Highly Tunable Low-Threshold Optical Parametric Oscillation in Radially Poled Whispering Gallery Resonators*, Phys. Rev. Lett. **106**, 143903 (2011).

[122] C. S. Werner, T. Beckmann, K. Buse, and I. Breunig, *Blue-pumped whispering gallery optical parametric oscillator*, Opt. Lett. **37**, 4224 (2012).

[123] M. Förtsch, J. U. Fürst, C. Wittmann, D. Strekalov, A. Aiello, M. V. Chekhova, C. Silberhorn, G. Leuchs, and Ch. Marquardt, *A versatile source of single photons for quantum information processing*, Nature Commun. **4**, 1818 (2013).

[124] Ch. Marquardt, D. Strekalov, J. Fürst, M. Förtsch, and G. Leuchs, *Nonlinear Optics in Crystalline Whispering Gallery Resonators*, Opt. Phot. News **24**, 38 (2013).

[125] M. Förtsch, G. Schunk, J. U. Fürst, D. Strekalov, T. Gerrits, M. J. Stevens, F. Sedlmeir, H. G. L. Schwefel, S. W. Nam, G. Leuchs, and Ch. Marquardt, *Highly efficient generation of single-mode photon pairs from a crystalline whispering-gallery-mode resonator source*, Phys. Rev. A **91**, 023812 (2015).

[126] M. Förtsch, T. Gerrits, M. J. Stevens, D. Strekalov, G. Schunk, J. U. Fürst, U. Vogl, F. Sedlmeir, H. G. L. Schwefel, G. Leuchs, S. W. Nam, and Ch. Marquardt, *Near-infrared single-photon spectroscopy of a whispering gallery mode resonator using energy-resolving transition edge sensors*, J. Opt. **17**, 065501 (2015).

[127] S. Huang and G. S. Agarwal, *Enhancement of cavity cooling of a micromechanical mirror using parametric interactions*, Phys. Rev. A **79**, 013821 (2009).

[128] S. Huang and G. S. Agarwal, *Normal-mode splitting in a coupled system of a nanomechanical oscillator and a parametric amplifier cavity*, Phys. Rev. A **80**, 033807 (2009).

[129] V. Peano, H. G. L. Schwefel, Ch. Marquardt, and F. Marquardt, *Optomechanical position detection enhanced by de-amplification using intracavity squeezing*, Phys. Rev. Lett. **115**, 243603 (2015).

[130] P. Degenfeld-Schonburg, C. Navarrete-Benlloch, and M. J. Hartmann, *Self-Consistent Projection Operator Theory in Nonlinear Quantum Optical Systems: A case study on Degenerate Optical Parametric Oscillators*, Phys. Rev. A **91**, 053850 (2015).

[131] A. Mari and J. Eisert, *Cooling by Heating: Very Hot Thermal Light Can Significantly Cool Quantum Systems*, Phys. Rev. Lett. **108**, 120602 (2012).

[132] F. Marquardt, J. P. Chen, A. A. Clerk, and S. M. Girvin, *Quantum Theory of Cavity-Assisted Sideband Cooling of Mechanical Motion*, Phys. Rev. Lett. **99**, 093902 (2007).

[133] M. J. Bhaseen, J. Mayoh, B. D. Simons, and J. Keeling, *Dynamics of nonequilibrium Dicke models*, Phys. Rev. A, **85**, 013817, (2012).

[134] J. Jin, A. Biella, O. Viyuela, L. Mazza, J. Keeling, R. Fazio and D. Rossini, *Cluster mean-field approach to the steady-state phase diagram of dissipative spin systems*, arXiv:1602.06553.

[135] J. J. Mendoza-Arenas, S. R. Clark, S. Felicetti, G. Romero, E. Solano, D. G. Angelakis and D. Jaksch, *Beyond mean-field bistability in driven-dissipative lattices: bunching-antibunching transition and quantum simulation*, arXiv:1510.06651.

[136] L. M. Sieberer, M. Buchhold and S. Diehl, *Keldysh Field Theory for Driven Open Quantum Systems*, arXiv: 1512.00637.

[137] J. Lang and F. Piazza, *Critical Relaxation with Overdamped Quasi-Particles in Driven-Dissipative Systems*, arXiv: 1602.05102.

Acknowledgements

First, I would like to thank my supervisor Prof. Michael J. Hartmann for his continuos support and all the helpful advice, ranging from important decisions to detailed scientific questions. Moreover, I would like to express my sincere gratitude for the trust and believe he put into the present work, which in this case can not be taken for granted, but rather requires courage to reach for something new. Michael has been a great supervisor and is a great person and I would always decide to join his group for a PhD again. Certainly, it has been a great time. Thank you.

Second, I would like to express my deepest thanks to Dr. Carlos Navarrete-Benlloch who has been an inspiring collaborator and became a good friend. His open-minded personality and will to share thoughts, knowledge and ideas is remarkable and I have certainly learned a lot from him. I truly wish him the best for his career, he for sure deserves it. Thanks a lot for everything Carlos.

Furthermore, my thanks goes to Prof.Wilhelm Zwerger and his group for the hospitality during my time at the TUM, the great stories during lunch time and the helpful scientific advices originating from an immense knowledge present in the group. In particular, I would like to thank Prof. Zwerger once more for his support in the thesis defense.
Moreover, I especially appreciate the discussions with Johannes Lang which taught me a lot about theoretical physics in general as well as about my own work. I highly respect Johannes for his talent and intelligence and I wish him all the best for his future career in science.

Special thanks also goes to my collaborator Mehdi Abdi, our discussions about physics were always enlightening and so much fun that we even took the discussions with us to lunch. Thanks for the great time and good luck with your future career.
Likewise, I would like to thank my former colleagues Simon Rips, Martin Leib and Elena del Valle for all the great times we spent together.

Last but not least, I would like to express my deepest gratitude towards my parents, Barbara and Stefan Degenfeld-Schonburg, my wonderful children Leopold, Constantin and Elara, and of course to my beloved wife Sina. Without you I would not be where I am now.